FEMTOSECOND LASER STUDIES OF CO AND NO ON Pd(111)

A thesis submitted for the degree of

Doctor of Philosophy

Jadranka Butorac

October 2011

University College London

I, Jadranka Butorac, confirm that the work presented in this thesis is my own. Where information has been derived from other sources, I confirm that this has been indicated in the thesis.

You leave home to seek your fortune and, when you get it, you go home and share it with your family.

To Zoran, Dorotea, Vjeko and Jelisaveta

ABSTRACT

The ultimate goal of any branch of chemistry, including surface chemistry, is to understand the dynamics of reactions. The typical time scale for bond making and breaking is the femtosecond time scale. Femtochemistry has led to enormous progress in the understanding, and even control, of chemical reactions in the gas and solution phases over the past decades. However, a comparable level of sophistication in the analysis of surface chemical reactions has not been achieved due to the complexity of the energy dissipation channels. For this thesis, a new experimental set-up was built with the goal to monitor the femtosecond laser-induced desorption (fs-LID) and femtosecond laser-induced reaction (fs-LIR) of CO and NO co-adsorbed on a Pd(111) surface. In addition, a femtosecond extreme ultraviolet (XUV) source was designed and commissioned. All the femtosecond laser-induced studies were accompanied by temperature programmed desorption (TPD) and reflection absorption infrared spectroscopy (RAIRS). First, fs-LID experiments were performed for pure CO and NO adsorbed on Pd(111) in order to test the apparatus. The CO and NO photodesorption dynamics were compared and the different photoreactivity was explained qualitatively using two theoretical models: electron friction and desorption induced by multiple electronic transitions (DIMET). The power law behaviour was also tested and a new method of fitting proposed. The photodesorption behaviour of CO co-adsorbed with NO on Pd(111) was then studied and compared qualitatively with the photodesorption behaviour of pure CO and NO within the empirical friction model.

The work described in this thesis is being prepared for submission for publication.

Chapter 4

The photochemistry of NO and CO on Pd(111)
J. Butorac, R.S. Minns, E. L. Wilson, H. H. Fielding and W. A. Brown
To be submitted to *J. Phys. Chem. C.*

The photochemistry of the NO/Pd(111) and CO/Pd(111) systems has been investigated as a function of surface coverage using femtosecond laser-induced desorption (fs-LID) and compared with temperature programmed desorption. The adsorbate-surface systems are characterised using RAIRS. The fs-LID yield is monitored as a function of surface coverage and laser fluence. A new fitting procedure is proposed to take into account the threshold for laser-induced desorption.

Chapter 5

Femtosecond laser-induced desorption of NO + CO on Pd(111)
J. Butorac, E. L. Wilson, R.S. Minns, W. A. Brown and H. H. Fielding
To be submitted to *J. Phys. Chem. C.*

The photochemistry of NO+CO on Pd(111) has been investigated as a function of surface coverage using femtosecond laser-induced desorption (fs-LID) and compared with temperature programmed desorption. The fs-LID yield is monitored as a function of surface coverage and laser fluence.

ACKNOWLEDGEMENTS

The work presented in this thesis was supervised by Helen Fielding and Wendy Brown to whom I express my gratitude for their advice, encouragement and active assistance. Helen Fielding was very supportive at the start of my PhD. She had great ideas how to solve either theoretical or practical problems and how to raise my spirit in the case of any accidents. Wendy was very helpful in the lab, and with time management. Thanks to both of them for their fast and thorough reading of my thesis chapters. I would also like to take this opportunity and express my gratitude to the EPSRC, ORS, Global Excellence Scholarship and Horswill Bequest for the provision of a studentship, without which none of this would have been possible.

I thank Professor Peter Saalfrank who provided me with some very useful ideas for Chapter 4 and Dr. Steve Firth who helped me deal with the femtosecond laser system. I am indebted to Dr. Russell Minns for his patience and his readiness to answer all my questions, and to his wife, Katherine, who read the first versions of my result chapters and helped me with the English. I am also indebted to Dr. Emma Wilson who taught me everything I know about the UHV system.

Many thanks to the staff and research students at UCL especially Ciarán, Roman, Douglas, Abi, Dorian, Maria, Adam K, Adam M, Jon, Nick and Rakhee, and to the staff in the MAPS faculty workshops, especially Roy and Jim. I would also like to thank Dave Knapp for help with the rotary pumps, and Len Parrish for all his assistance in synchronizing the femtosecond laser system and quadrupole mass spectrometer.

I would like to express my gratitude to my family, especially my mother, mother-in-law, sister Marija and sisters-in-law Anja and Mira for their help with looking after my son, Zoran, whilst I wrote this thesis. Finally I would like to thank my husband Vjeko and my children Zoran and Dorotea, without whose love and support I would have never gone this far.

CONTENTS

LIST OF FIGURES

CHAPTER 1

CHAPTER 2

CHAPTER 3

CHAPTER 4

CHAPTER 5

LIST OF TABLES

CHAPTER 1

CHAPTER 2

CHAPTER 4

CHAPTER 5

FREQUENTLY USED ABBREVIATIONS

2PC	two pulse correlation
CCD	charge coupled device
CPA	chirped pulse amplification
cw	continuous wave
DFT	density functional theory
DIET	desorption induced by electronic transitions
DIMET	desorption induced by multiple electronic transitions
DOS	density of states
fs-LID	femtosecond laser-induced desorption
fs-LIR	femtosecond laser-induced reaction
FTIR	Fourier transform infrared
FWHM	full-width at half maximum
GDD	group delay dispersion
GVD	group velocity dispersion
HOMO	highest occupied molecular orbital
HREELS	high resolution electron energy loss spectroscopy
IR	infrared
L	Langmuir
LEED	low energy electron diffraction
LUMO	lowest occupied molecular orbital
MCT	mercury cadmium telluride
ML	monolayer
PES	potential energy surface
PM	polarisation modulation
QMS	quadrupole mass spectrometer
RAIRS	reflection absorption infrared spectroscopy
REMPI	resonance enhanced multiphoton ionization
SFG	sum frequency generation
SHG	second harmonic generation
STM	scanning tunnelling microscopy
TPD	temperature programmed desorption

TRPES	time-resolved photoelectron spectroscopy
TTL	transform transform limited
UHV	ultra high vacuum system
UPS	ultraviolet photoemission spectroscopy
UV	ultraviolet
XUV	extreme ultraviolet
yield-FD	fluence dependence of the reaction yield

CHAPTER 1

INTRODUCTION

Surfaces are known to be very difficult systems to study, due to complex surface preparation procedures, and the requirement to maintain a clean and well-defined surface. However, detailed understanding of chemical reactions on metal surfaces is particularly important since many metal surfaces are known to be good catalysts for a large number of chemical reactions. The ultimate goal is to understand the *dynamics* of surface reactions and this is not possible by simply utilizing standard surface science techniques such as scanning tunnelling microscopy (STM), low energy electron diffraction (LEED), high resolution electron energy loss spectroscopy (HREELS), ultraviolet photoelectron spectroscopy (UPS), temperature programmed desorption (TPD), reflection absorption infrared spectroscopy (RAIRS), and many others.

In order to be able to elucidate the dynamics of chemical reactions on surfaces, femtosecond time resolution is necessary, since this is the timescale of bond making and bond breaking. Experimental studies with femtosecond time resolution became possible with the development of lasers with ultrashort pulse duration. [1] The field was pioneered by Zewail and co-workers and recognized by the award of the Chemistry Nobel prize in 1999.[2] Time-resolved femtochemistry experiments led to huge progress in the understanding and control of chemical reactions in the gas and solution phase, however surface femtochemistry, both static and time-resolved, is still in relative infancy, with the fundamental processes not well-understood.

In this thesis, a novel experimental set-up is designed in order to monitor, for the first time, the femtosecond laser-induced desorption (fs-LID) and reaction of CO and NO co-adsorbed on a Pd(111) surface.

1.1 Motivation for studying adsorption of CO and NO on surfaces

The study of the adsorption of molecules on solid surfaces has increased greatly since the early 1960s. About 90% of all industrial chemical processes involve heterogeneous catalysis, which is not only the basis of the chemical and petroleum industries, but is also of crucial importance for protecting the environment. [3]

In this PhD thesis, the reaction of interest is that between CO and NO on Pd(111). The CO + NO reaction has been studied over a variety of transition and noble metal catalysts. [4 –13] In the late 1970s, the three-way catalytic converter was introduced into the emission control systems of car exhausts in the United States. The three-way catalytic converter simultaneously catalyses three reactions: the reduction of NO_x species, the oxidation of CO and the oxidation of excess hydrocarbons, as shown in Scheme 1.1.

$$2NO_x \rightarrow xO_2 + N_2 \quad (1)$$

$$2CO + O_2 \rightarrow 2CO_2 \quad (2)$$

$$C_xH_{2x+2} + [(3x+1)/2]O_2 \rightarrow xCO_2 + (x+1)H_2O \quad (3)$$

Scheme 1.1. Reactions in the three-way catalytic converter.

In order to choose the cheapest and the best catalyst it is important to understand the fundamental reaction pathways and catalytic characteristics. The first catalysts were made of platinum and rhodium (90% platinum and 10% rhodium). The problem with these catalysts is that rhodium is expensive and a rare element, so with the increasing number of cars in operation there is a desire to replace rhodium with a less expensive, more plentiful, substitute. Palladium is one possible alternative, not only because it is more plentiful, but it has also been found to be more durable at higher reaction temperatures, so it can be positioned nearer to the engine. Palladium has also demonstrated excellent hydrocarbon oxidation characteristics. [3]

1.2 Surface science approach in studying real catalysts

A typical catalyst consists of nanometer sized particles with a lot of different crystal planes with various structural defects and chemisorbed foreign atoms. Hence, the surface chemistry of a real catalyst is rather complex. [14] Langmuir [15] in 1922 suggested a scientific approach that enables studying real catalysts in a systematic way:

In order to simplify our theoretical considerations of reactions at surfaces, let us confine our attention to plane surfaces. If the principles in this case are well understood, it should then be possible to extend the theory to the case of porous bodies.

Thus, the first step towards understanding reactions on real surfaces that are used in catalysis is to understand the reaction on a well-defined, single-crystal surface that is prepared and investigated using ultrahigh vacuum (UHV) techniques and a whole range of classic surface science techniques. Since most classic surface science techniques cannot be performed at the high pressure conditions of real catalysis, there is a so-called 'pressure gap'. In addition, since the properties of well-defined single crystal surfaces will generally be quite different to the surface properties of real catalysts, there is a so-called 'materials gap'. [14] The materials gap can be overcome by comparing reactions on various well-defined surfaces with conventional high surface area powder catalysts. [3] Some of the surface science techniques, such as RAIRS, can be used under atmospheric conditions. Hence, the pressure gap can be overcome by studying the reaction at different pressures.

In this thesis, the reaction of interest is studied on a well-defined, single crystal surface under UHV conditions as a first step towards understanding the same reaction on real catalysts under atmospheric conditions.

1.3 Importance of femtosecond lasers in surface photochemistry

There are several factors motivating the use of femtosecond lasers in surface science experiments. Perhaps the most obvious motivation, as in gas-phase studies, [16, 17] is the possibility of direct access to the fundamental time-scale of the relevant chemical processes. In addition to this, the absorption of femtosecond laser pulses at a metal surface can result in the creation of unique, non-equilibrium, excitation of the substrate. The exploration of surface processes resulting from these conditions is interesting in its

own right. Figure 1.1 shows a flow chart of how energy can be transferred between the substrate and adsorbate electronic and vibrational excitations.

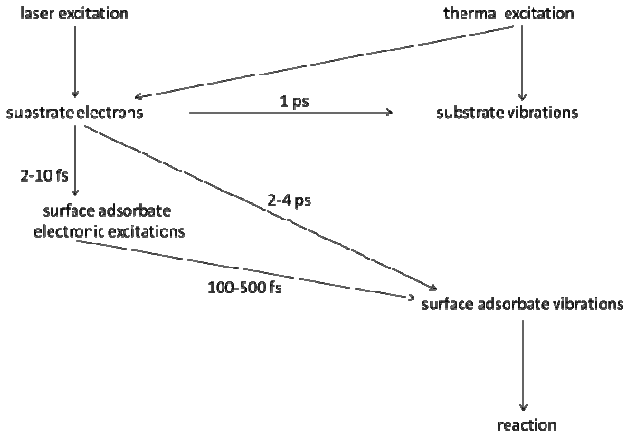

Figure 1.1 Chart of energy flow at electronic conductor surfaces excited by lasers *versus* conventional thermal sources.

All of the processes shown in Figure 1.1 can be identified in a time-resolved experiment. If the reaction finishes ~60 fs after the photoabsorption event, then there is probably a direct coupling between electronic excitations of the adsorbate-substrate complex and the surface adsorbate vibrations (the reaction will take ~10 fs within the electronic lifetime plus half a vibrational period, typically ~50 fs). However, if the substrate electrons excite the adsorbate surface vibration non-resonantly, then the reaction may not begin for ~1 ps, because the coupling time between the substrate electrons and the vibrations is ~1 ps. In the case of substrate phonons exciting adsorbate surface vibrations, the reaction will be finished in more than 10 ps. From these examples, it is clear that the reaction-time provides a direct way of distinguishing between different pathways.

The mechanism of energy flow between an adsorbate and a substrate is of fundamental importance in surface science. The role of coupling of the adsorbate motion to the substrate phonons is well understood, but the influence of energy exchange with substrate electronic excitations under thermal conditions has been the subject of discussion for many years. [18 – 21] These effects are especially important in chemisorbed systems, where there is a charge transfer between the substrate and the adsorbate.

Irradiation of a metal surface with femtosecond laser pulses results in the confinement of all energy in the electronic system during short-lived, electron-hole pair transients. These non-thermalized, hot carriers are capable of inducing surface reactions. This effect is the well-known process of substrate mediated surface photochemistry. However, in classic substrate mediated surface photochemistry (using a continuous wave laser or a nanosecond pulse laser) the density of these hot carriers is usually low, so the possibility for new reaction channels is not as high as with femtosecond laser pulses.

Femtosecond laser pulses also enable the study of non-adiabatic effects. When the substrate is a metal surface, there is a whole manifold of electron-hole pair excitations, so the Born-Oppenheimer (adiabatic) approximation is often not a good approximation. The Born-Oppenheimer approximation assumes that the electron motion is much faster than the nuclear motion, hence the electrons adjust instantaneously to the current nuclear configuration. When the electrons do not respond instantaneously to the motion of the adsorbate, electron-hole pairs can be created or destroyed, and this is the origin of strong non-adiabatic couplings.

1.4 Laser excitation of a metal adsorbate system

In Figure 1.1 it was shown schematically how energy flows between the electronic and vibrational excitations in the adsorbate-substrate complex and several pathways by which laser excitation can lead to chemical reaction. Each of these subsystems can be studied in detail. Hence, first the response of the metal substrate (parameters will be given for Pd(111)) to femtosecond laser pulses will be considered and then the electronic structures of the adsorbates, CO and NO, on Pd(111) will be presented. Finally, two models for describing the coupling mechanism for the energy transfer between the substrate and adsorbate will be described.

1.5 Laser excitation of the substrate

Upon photoabsorption, the following processes occur within a metal substrate: [22]

1) Photons of energy *hv* are absorbed by the electrons.

2) The non-equilibrium electron distribution relaxes by electron-electron interactions toward the Fermi-Dirac distribution, which can be characterized by a local electron temperature $T_e(r, t)$.

3) Simultaneously with **2)**, electrons scatter to lower energies by electron-phonon interactions. The resulting excited phonons are not necessarily in thermal equilibrium with the electrons.

4) The non-equilibrium phonon distribution relaxes by phonon-phonon and electron-phonon interactions toward the equilibrium Bose-Einstein distribution at the local lattice temperature $T_p(r, t)$.

5) Simultaneously with **1)** to **4)**, thermal diffusion, carried by the electrons, distributes the energy deposited within the optical penetration depth into the bulk.

As an approximate description of the substrate excitation, the two temperature model [23] is usually used. In this model, the electronic excitation is taken to be characterized by an equilibrium Fermi-Dirac distribution at a temperature T_e (electron heat bath) and the phonons are characterized by a thermal Bose-Einstein distribution at a temperature T_p (phonon heat bath). The electron heat bath transfers energy, either to the substrate by thermal diffusion, or to the phonon heat bath *via* electron-phonon coupling. In this model, only one-dimensional heat flow along the surface normal direction z will be considered, since the size of the laser spot is large compared to the optical penetration length and the lateral thermal diffusion lengths. The temporal evolution of the electron and phonon heat baths can be represented by a set of coupled differential equations:

$$C_e \frac{\partial T_e}{\partial t} = \frac{\partial}{\partial z} \kappa_e \frac{\partial T_e}{\partial z} - g(T_e - T_p) + A(z,t) \qquad (1.1a)$$

$$C_p \frac{\partial T_p}{\partial t} = g(T_e - T_p), \qquad (1.1b)$$

where C_e and C_p denote, respectively, the electronic and phonon heat capacities, κ_e is the thermal conductivity, g is the electron-phonon coupling constant, and $A(z, t)$ represents a term which is due to the absorption of the laser pulse. All the constants necessary to solve these equations for Pd are given in Table 1.1.

Table 1.1 Physical properties of palladium.

electronic specific heat coefficient	γ_1	249.14 J m^{-3} K^{-2} [24]
electronic specific heat offset	γ_0	249.14 J K^{-2} m^{-3}
thermal conductivity at 300 K	κ_0	72 W m^{-1} K^{-1} [25]
Debye temperature	ϑ_D	274 K [25]
refractive index (800 nm)	n_r+ik	2.08+4.55*i*
optical penetration depth*	δ	14 nm

The temperature dependence of the electron thermal conductivity can be approximated *via*: [26]

$$\kappa_e = \kappa_0 \frac{T_e}{T_p}, \tag{1.2}$$

where κ_0 is the thermal conductivity at 300 K (given in Table 1.1).

The phonon heat capacity, as a function of phonon temperature T_p, can be calculated according to the Debye approximation: [25]

$$C_p = 9N_A k_B \left(\frac{T_p}{\vartheta_D}\right)^3 \int_0^{\frac{\vartheta}{T_p}} dx \frac{x^4 e^x}{\left(e^x - 1\right)^2}, \tag{1.3}$$

where N_A is the Avogadro constant, k_B is the Boltzmann constant and ϑ_D is the Debye temperature that is given in Table 1.1. For $T_p > \vartheta_D$, Equation 1.3 passes into the Dulong-Petit law, where a constant heat capacity, C_p ~25 J K^{-1} mol^{-1} is derived.

The heat capacity of the electrons, C_e, depends on T_e and is given by [25]

$$C_e = \gamma_0 + \gamma_1 T_e, \tag{1.4}$$

where γ_1 is the electronic specific heat coefficient and γ_0 is the electronic specific heat offset, both given in Table 1.1.

The value of the electron-phonon coupling constant, $g = 5\times10^{11}$ W cm^{-3} K^{-1}, was determined from the relationship given by Allen. [27]

The overall optical excitation *A*, as a function of *z* and *t* is:

---

* $\delta = \frac{\lambda}{4\pi k}$, where λ is the wavelength and *k* is the imaginary part of refractive index.

$$A(z,t) = \frac{(1-R)I(t)}{\delta}\exp\left(-\frac{z}{\delta}\right), \tag{1.5}$$

where R is the reflectivity of the metal surface for the particular angle of incidence, I is the intensity of laser radiation, z is the direction of propagation perpendicular to the surface, and δ is the optical penetration depth. The reflectivity for light polarized perpendicular (R_s) or parallel (R_p) to the plane of incidence can be calculated from the Fresnel equations as a function of the angle of incidence i: [28]

$$R_s = \frac{a^2 + b^2 - 2a\cos i + \cos^2 i}{a^2 + b^2 + 2a\cos i + \cos^2 i} \tag{1.6a}$$

and

$$R_p = R_s \frac{a^2 + b^2 - 2a\sin i\tan i + \sin^2 i\tan^2 i}{a^2 + b^2 + 2a\sin i\tan i + \sin^2 i\tan^2 i}, \tag{1.6b}$$

where a, b can be obtained from

$$2a^2 = [(n_r{}^2 - k^2 - \sin^2 i)^2 + 4n_r{}^2k^2]^{1/2} + (n_r{}^2 - k^2 - \sin^2 i) \tag{1.6c}$$

$$2b^2 = [(n_r{}^2 - k^2 - \sin^2 i)^2 - 4n_r{}^2k^2]^{1/2} + (n_r{}^2 - k^2 - \sin^2 i). \tag{1.6d}$$

In these relations, n_r is the real part of the refractive index and k is the imaginary part of the refractive index, $n = n_r + \mathrm{i}k$.

In Chapter 5, qualitative analysis of photodesorption results for co-adsorbed systems is performed using results for T_e and T_p from Szymanski *et al.*[29], so all the physical constants and parameters needed to solve equations 1.1a and 1.1b are described in detail. Equations 1.6a and 1.6b are not only relevant for the calculation of the optical excitation in the two temperature model, but also for the calculation of absorbed laser fluence (described in detail in Chapter 2). For all experiments performed in this thesis, laser light was polarized perpendicular to the plane of the sample (parallel to the plane of incidence).

1.6 Electronic structure of the CO and NO on transition metals

In the free CO molecule, the 5σ and 2π* molecular orbitals are the highest occupied (HOMO) and lowest unoccupied (LUMO) molecular orbitals, respectively. Upon adsorption, it is generally assumed that the major CO-metal interaction can be explained in terms of interactions of the HOMO and LUMO of the adsorbate with the metal d-orbitals. The Blyholder model [30] is based on donation from the occupied CO 5σ orbital into empty surface orbitals, and back-donation from occupied surface orbitals to the unoccupied CO 2π* orbital. In the literature, there is divided opinion about this model. [31, 32, 33, 34] The chemisorption of CO on a metal surface can also be determined using density functional theory (DFT) calculations, [35] and the contribution to chemisorption is considered to be not only from the 5σ and 2π* orbitals, but also from the 1π and 4σ orbitals of CO.

Figure 1.2 shows the density of states (DOS) for the free CO molecule (for the 1π, 4σ, 5σ and 2π* orbitals) and the interaction of these orbitals with the metal substrate (Pt) d-orbitals. Based on the position of Pt and Pd in the periodic table, a similar interaction of CO with the Pd d-orbitals is expected. The position of the molecular orbitals of the CO adsorbate on Pd will be slightly shifted with respect to the Fermi level, since the Fermi energy of Pd is ~1 eV lower than the Fermi energy of Pt [36].

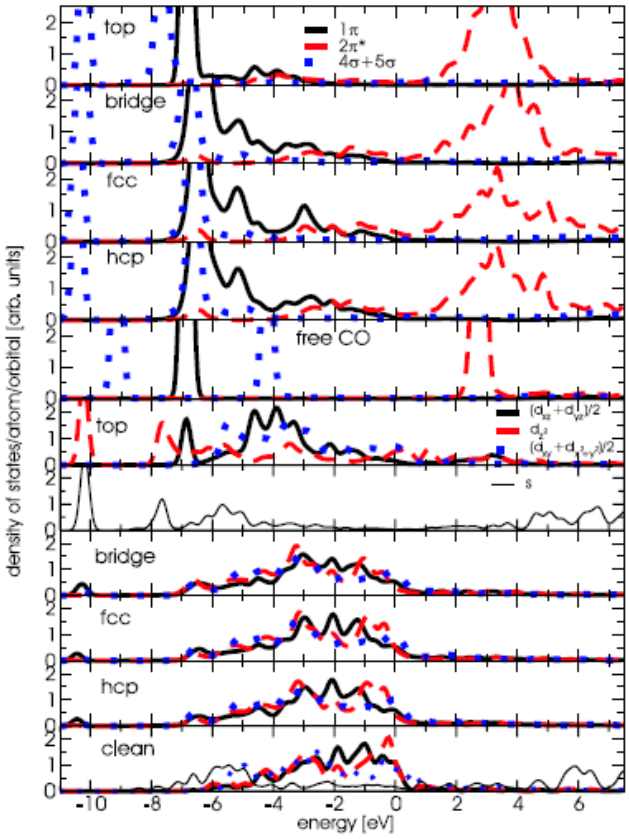

Figure 1.2 The electronic densities of states for the CO molecule adsorbed in top, bridge, fcc and hcp hollow sites of Pt surfaces. The upper five panels describe the density of states (DOS) for various molecular orbitals of the CO molecule. The lower six panels show the DOS for the substrate atom(s) interacting most with the molecule. The panels labelled "free CO" and "clean" describe the non-interacting case for comparison. Figure taken from reference 35.

The main role in bonding CO to the metal surface is due to the interaction of the 5σ, 1π and 2π* orbitals with the metal. Upon adsorption, these orbitals shift in energy and broaden. This broadening and shift increases with the coordination number of the substrate atoms. The 5σ orbital of CO interacts with the d_z^2 orbital of the metal, and the bonding contribution is centred ~7.5 eV below the Fermi level. [37] The antibonding contribution is located at higher energies and extends up to the Fermi level. The 1π and 2π* orbitals of CO interact with the d_{xz} (d_{yz}) and in plane ($d_{x^2-y^2}$, d_{xy}) orbitals of metal atoms. The main part of the 1π orbital is centred ~ 6 eV below the Fermi level. Upon adsorption, this peak broadens, ending up at the Fermi level. The partially filled 2π* orbital has a bonding contribution in the same energy range as the 1π orbital, but the

density of states is very low, as can be seen in Figure 1.2. The main antibonding contribution is positioned at ~3 eV above the Fermi level. [37]

The same mechanisms dominate the adsorption of NO, but now the partially filled $2\pi^*$ orbital, after interaction with the metal d-orbitals, has both bonding and antibonding contributions near the Fermi edge, and the 5σ and 1π orbitals are located at higher binding energies. The repulsive interactions arising from the interaction of the 1π orbital with the d-band are greatly reduced, while donation from the 5σ state is still efficient. [37] This electronic structure of the adsorbate substrate complex explains the larger adsorption energy of NO compared to CO, which is illustrated in TPD and RAIRS experiments in Chapters 4 and 5. Experimental investigations using direct and inverse photoelectron spectroscopy for CO and NO adsorption on Pd(111), show that the $2\pi^*$ orbitals of CO lies at around 4.6 eV with respect to the Fermi level, and the $2\pi^*$ orbitals of NO have contributions below the Fermi level (~-2.7 eV) and above the Fermi level (~1.7 eV), [38] in agreement with DFT calculations shown in Figure 1.2. The position of the $2\pi^*$ orbital with respect to the Fermi level gives one of the possible explanations for the lower fluence threshold for NO on Pd(111) than for CO on Pd(111) in terms of desorption induced by multiple electronic transitions (DIMET). This mechanism is explained in more detail in Section 1.8 b. The fluence threshold observed in fs-LID studies of CO and NO on Pd(111) is discussed in Chapter 4.

1.7 Mechanisms of coupling of electronic excitation to adsorbate degrees of freedom

The coupling of electronic degrees of freedom to adsorbate motion has received a great deal of attention in the literature. [32, 39] In this section, two models are discussed that treat the strong coupling between the substrate electronic excitation and adsorbate modes: the friction model and DIMET.

1.7.1 Friction model

In this model, [40, 41] adsorbate motion is assumed to occur on a single potential energy surface. The interaction of the adsorbate with substrate electronic excitations, causes the motion on the potential energy surface to be perturbed. Figure 1.3 is a cartoon illustrating the electronic friction mechanism.

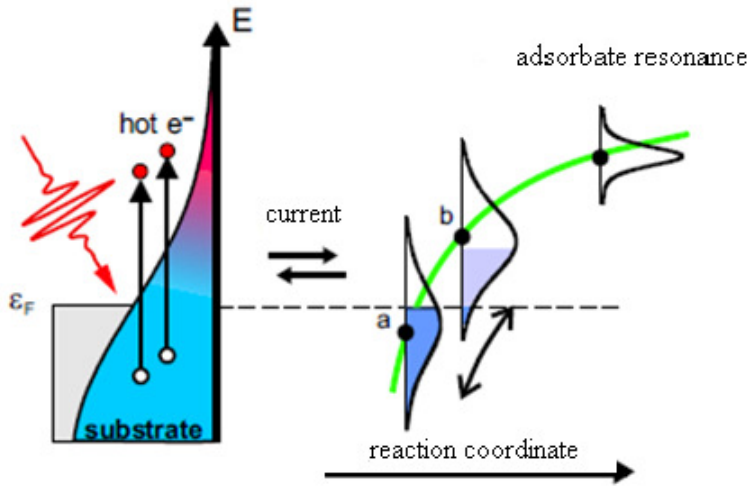

Figure 1.3 Frictional coupling between the adsorbate and the substrate. The adsorbate vibration leads to a motion along the reaction coordinate and an energetic shift of the adsorbate resonance with respect to the Fermi level. Motion of the adsorbate creates electron-hole pairs in the substrate. Figure taken from reference 42.

Two well-established models are used to describe the interactions of the adsorbate with substrate electronic excitations, one of which uses a quantum mechanical approach to describe the excitation of the intramolecular coordinate and the other uses classical equations to describe the motion of the centre of mass of the adsorbate.

1.7.1.1 Quantum mechanical approach to the friction model

In this model, the energy transfer between the substrate and the adsorbate is mediated by frictional coupling between the electron and phonon heat bath to a harmonic oscillator of the adsorbate motion. The time evolution of the energy content of the adsorbate is based on the master equation formalism, [40, 43] and can be represented by Equation 1.7: [44]

$$\frac{d}{dt}U_{ads} = \eta_e\left(U_e - U_{ads}\right) + \eta_p\left(U_p - U_{ads}\right) \qquad (1.7)$$

where η_e and η_p are coupling coefficients between the substrate electrons and the adsorbate and substrate phonons and the adsorbate, U_{ads} is the energy of the adsorbate and U_p and U_e denote the energy that would be in vibrations if it was equilibrated at a temperature T_p or T_e, respectively.

$$U_{p(e)} = \hbar\omega \left[\exp\left(\frac{\hbar\omega}{k_B T_{p(e)}} \right) - 1 \right]^{-1}, \tag{1.8}$$

where $\hbar$ is the Planck constant divided by 2π, ω is the angular frequency and k_B is the Boltzmann constant. If T_{ads}, T_p and $T_e >> \frac{\hbar\omega}{k_B}$, then the oscillator energies (U_{ads}, U_p and U_e) can be replaced by their classical limits - the corresponding temperatures themselves. Thus, Equation 1.7 becomes:

$$\frac{d}{dt} T_{ads} = \eta_e (T_e - T_{ads}) + \eta_p (T_p - T_{ads}). \tag{1.9}$$

T_{ads} can be calculated from Equation 1.9 after T_e and T_p are calculated using the two temperature model. [23] This T_{ads} is then used to obtain the reaction rate, R, and finally, the reaction yield, Y, as the time integral of R. The reaction rate is calculated from the Arrhenius expression for the desorption rate at a given oscillator temperature:

$$R(t) = -\frac{d}{dt}\theta = \theta^n \nu \exp\left(-\frac{E_a}{k_B T_{ads}(t)} \right), \tag{1.10}$$

where θ, n, ν and E_a denote the coverage, the order of the reaction kinetics, pre-exponential factor and activation energy for desorption. This model was used in Chapter 5 when desorption yields in fs-LID experiments of CO or NO in co-adsorbed systems are compared with desorption yields of pure CO or NO, respectively. In Chapter 4, the higher photoreactivity of NO is explained using the modified friction model developed by Brandbyge and co-workers. [41] In this model, only coupling between the substrate electrons and the adsorbate is considered, so Equation 1.9 becomes,

$$\frac{d}{dt} T_{ads} = \eta_e (T_e - T_{ads}). \tag{1.11}$$

The probability of desorption, P_{des}, in this model is given by Equation 1.12:

$$P_{des}(t) = E_a \int_0^\infty dt \frac{\eta_e}{T_{ads}} \exp\left(-\frac{E_a}{k_B T_{ads}} \right). \tag{1.12}$$

The activation energy, E_a, electron friction coefficient η_e, and adsorbate temperature T_{ads}, now enter the pre-exponential factor. It is very easy to relate a value of η_e to the

desorption probability, since the desorption probability is proportional to the value of the electron friction coefficient.

1.7.1.2 Classical treatment of motion in the friction model

The quantum mechanical model of electronic friction is only suitable for the case where the interaction potential is harmonic, for example, the excitation of the intramolecular vibration of the adsorbate. A semi-classical treatment of the motion enables the study of more complex and realistic potential energy surfaces, and gives direct information about the motion of the adsorbate-substrate complex. This approach has not been used in this thesis, but it will be described briefly as an approach from which information about the adsorbate-substrate system is obtained directly. The weakness of this model is in the error introduced by neglect of quantum mechanical effects. This error is not so significant for high electron temperatures where there is significant population of quantum states.

The nuclei are described by a classical equation of motion, with a frictional coupling to the heat bath. In its one-dimensional form, the Langevin equation [45] for motion is:

$$\frac{d^2z}{dt^2} + \eta_e \frac{dz}{dt} = \frac{F(z)}{m} + \Gamma(t). \qquad (1.13)$$

Here, m is the particle mass, z is the distance between the adsorbate and substrate, η_e is the friction coefficient for coupling between the electronic degrees of freedom of the substrate and the nuclear degrees of freedom of the adsorbate, F is the force acting on the particle in the adsorption well modelled by a Morse potential and $\Gamma(t)$ is the stochastic force. Direct integration of Equation 1.13 gives a set of stochastic trajectories of the adsorbate centre of mass coordinate.

1.7.2 DIMET

The DIMET model [46] is based on the model for desorption induced by electronic transitions [47] (DIET). In this model, the substrate electronic excitations act to induce electronic transitions in adsorbate localized states. It is employed in the literature for treating conventional photoinduced effects on surfaces [32, 39] induced by pulses of at least

picosecond duration. However, the novel aspect of this model associated with femtosecond pulses is related to the density of substrate electronic excitation (density of electron-hole pairs) seen at high electronic temperatures, T_e. This high density of electron-hole pairs can lead to a lot of successive electronic transitions that transfer energy into adsorbate motion before it vibrationally relaxes into the ground electronic state. Before introducing the DIMET model, the DIET model will be described briefly.

1.7.2.1 DIET model

The first successful explanation of the DIET mechanism was given by Menzel, Gomer and Redhead. [48, 49] The excitation mechanism is shown in Figure 1.4.

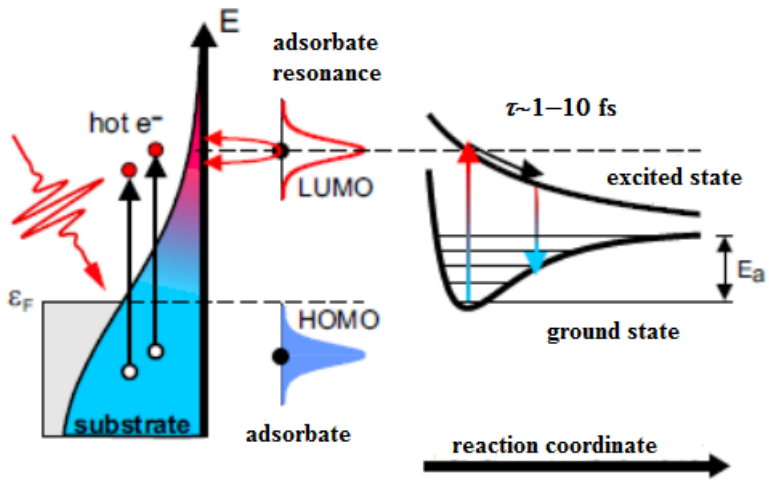

Figure 1.4 Schematic 1D illustration of DIET. Excitation of the adsorbate is through an electronic transition to a repulsive electronic state. After returning to the ground electronic state, the molecule gains vibrational energy. Figure taken from reference 42.

In Figure 1.4, the excited electronic state is repulsive, as proposed in the Menzel-Gomer-Redhead model. The same mechanism is also valid for bound excited states, first considered by Antoniewicz [50]. The ground potential energy surface (PES) can be described using a Morse potential. The system undergoes an electronic transition from the ground electronic state (HOMO) to the higher lying adsorbate resonance (LUMO). The equilibrium distance of the excited PES is displaced from that of the ground PES, so this results in a large force that accelerates the adsorbate towards the surface. The lifetime of the adsorbate on the excited PES is short, hence the adsorbate returns to the

ground PES after having moved only slightly, and usually the vibrational energy gain is not enough for the adsorbate to desorb. This fact explains the low desorption yields usually seen in DIET on metal surfaces.

1.7.2.2 DIMET model

At the high electronic temperatures reached during femtosecond laser irradiation of the substrate, a novel mechanism for the energy transfer between the substrate and adsorbate may appear. The initial step is a Franck-Condon transition to the excited PES. If the adsorbate remains on the excited PES for a time $t < \tau_c$ (τ_c is the minimum duration of motion on the excited PES necessary for desorption to occur), then the adsorbate cannot desorb, but it can make another Franck-Condon transition, from a vibrationally excited level of the ground PES. The adsorbate-surface vibration will therefore gain an additional amount of vibrational energy. A lot of these excitation-deexcitation cycles may occur within the lifetime of the molecule–surface vibration, so the desorption probability will be significantly enhanced compared to DIET. Stochastic trajectory simulations can be performed to obtain more quantitative understanding of the DIMET mechanism. For these simulations a knowledge of the ground and excited PES is required, as well as the rates of excitation and deexcitation. If the excited PES is regarded as a negative ion excited state, then the excitation and deexcitation can be regarded as the hopping of the electron from the substrate onto the adsorbed molecule and *vice versa*. The deexcitation rate can be modelled as:

$$k_d = \left[\tau^{-1} e^{-z/z_d}\right]\left[1 - f(\varepsilon_A(z), T_e(t))\right], \tag{1.14}$$

where τ is the excited state lifetime, z is the substrate-adsorbate distance, z_d is the parameter for the fall-off in the hopping rate, $f(\varepsilon, T_e)$ denotes the Fermi factor for energy ε and electronic temperature T_e. The activation rate can be modelled as:

$$k_a(z) = k_d(z) \exp\left[-\frac{\varepsilon_A(z)}{kT_e(t)}\right], \tag{1.15}$$

where k_d is the deexcitation rate, ε_A is the difference in the energy between the excited and ground PES for one value of z. The desorption trajectories can then be calculated

from stochastic simulations. In Chapter 4, the higher photoreactivity of NO compared to CO is explained using equations 1.14 and 1.15.

1.8 Link between laser-induced reactions and thermal reactions

The processes initiated by a femtosecond laser can be driven by non-equilibrium substrate electrons, before their thermal equilibration with phonons. A range of adsorbate/metal systems have been studied experimentally and theoretically using femtosecond laser excitation, see for example reference. [51]

If there is a possibility for competing reaction pathways, as was the case for O_2/Pt(111), [52] the channel favoured by thermally driven reactions can be different from the one favoured by femtosecond laser-induced reactions. In the case of O_2/Pt(111), heating of the Pt(111) surface with a saturation coverage of molecular oxygen gives rise to a substantial coverage of atomic oxygen, so the dissociation channel is preferred to the desorption channel. When the system is irradiated by femtosecond laser pulses, then there is a strong preference for desorption over dissociation. One of the exciting possibilities offered by femtosecond laser-induced reactions is the possibility for a new reaction path. This was demonstrated for a ruthenium surface on which carbon monoxide and atomic oxygen were co-adsorbed. [53] For this system, CO_2 cannot be formed thermally, but upon irradiation with femtosecond laser pulses there are two processes happening: formation of CO_2 (new reaction channel) and desorption of CO (a process also observed in thermally-induced reactions).

Nonetheless the reaction channels for thermally-induced desorption are sometimes the same as those for fs-LID. For example, based on the examples shown in the previous paragraph, it is expected that the dissociation channel will be active in the femtosecond laser irradiation of NO/Pd(111) [54] even though this is not the case in TPD experiments. There were no significant reaction products due to the molecular dissociation of NO, and this finding is consistent with the one from TPD.

There are many authors who have modelled fs-LID data successfully using activation energy from TPD data, either for the case where the channel favoured by a thermally driven reaction is different from the one favoured by fs-LID experiments (see for example Bonn *et al.* [53]) or is the same (see for example Prybyla *et al.* [54]).

In Chapter 5, the importance of finding a link between thermally-induced reactions and femtosecond laser-induced reactions is discussed. In the modelling of femtosecond laser-induced desorption by the friction approach, the desorption step can be modelled as the crossing of an effective activation energy barrier. If a simple one dimensional potential energy surface is assumed, then the activation energy for photoinduced desorption is presumed to be the same as that used to describe thermal desorption. There are several cases where the activation energy from TPD data has been used successfully to simulate photodesorption. [44,53,55,56] The photodesorption in these cases was modelled only for the case of one adsorbate on a particular metal surface. In this thesis a change in the position of the desorption peak maximum in TPD spectra in co-adsorbed (CO + NO/Pd(111)) with respect to the pure systems (CO/Pd(111) or NO/Pd(111)) is linked to the measured difference in the photodesorption yield for the first time.

1.9 Summary

This chapter introduced key topics that are important for the work described in Chapters 4 and 5. Chapter 4 describes the fs-LID of pure CO and NO on Pd(111) which have been performed before, [54, 56] providing a good test of the new apparatus. It also sets the scene for the next chapter. Chapter 5 describes the fs-LID of co-adsorbed CO and NO, together with a brief description of the reaction products generated during irradiation at one particular laser fluence.

The CO and NO reaction on Pd(111) was chosen because there is a lack of knowledge about the molecular mechanism. Palladium would be a good alternative to expensive rhodium that is currently used in car exhaust catalysis.

Irradiation of the CO(NO)/NO(CO)/Pd(111) surface with femtosecond laser pulses can provide the possibility for a new reaction path, or a reaction channel favoured by TPD (desorption of CO and NO) which can be different from a reaction channel favoured by fs-LID (preferably CO and NO reaction).

1.10 Thesis outline

In this chapter, the theoretical concepts for Chapter 4 and 5 have been introduced.

Chapter 2 describes a novel apparatus designed for fs-LID studies, and describes in detail photodesorption experiments. Basic theoretical concepts for TPD and RAIRS are also described.

Chapter 3 describes the design and commissioning of a femtosecond extreme ultraviolet (XUV) source, and theoretical simulations of the 9th (89 nm) and the 11th (72 nm) harmonic of the fundamental 800 nm femtosecond radiation. This apparatus can currently be used for gas phase photochemistry experiments.

Chapter 4 describes fs-LID studies of CO and NO adsorbed individually on the Pd(111) surface. Fs-LID studies are performed for three CO (NO) exposures, respectively. These studies are accompanied by RAIRS and TPD, and provide a good test of the new apparatus.

In Chapter 5, fs-LID studies are presented for systems where CO and NO are co-adsorbed. Studies were performed either by first dosing NO and then exposing the surface to CO, or by first dosing CO and then exposing the surface to NO. The photodesorption behaviour of CO or NO in the co-adsorbed systems is compared with the photodesorption of pure CO or NO, respectively.

1.11 References

1. C. V. Shank, R. L. Fork, R. Yen, R. H. Stolen and W. J. Tomlinson, *Applied Physics Letters*, **40** (9), 761 (1982).
2. A. H. Zewail, *Angewandte Chemie-International Edition*, **39** (15), 2587 (2000).
3. D. R. Rainer, S. M. Vesecky, M. Koranne, W. S. Oh and D. W. Goodman, *Journal of Catalysis*, **167** (1), 234 (1997).
4. J. D. Butler and D. R. Davis, *Journal of the Chemical Society-Dalton Transactions*, (21), 2249 (1976).
5. S. H. Oh, G. B. Fisher, J. E. Carpenter and D. W. Goodman, *Journal of Catalysis*, **100** (2), 360 (1986).
6. L. M. Carballo, T. Hahn and H. G. Lintz, *Applied Surface Science*, **40** (1-2), 53 (1989).
7. T. Hahn and H. G. Lintz, *Applied Surface Science*, **40** (1-2), 59 (1989).

8. S. H. Oh and C. C. Eickel, *Journal of Catalysis*, **128** (2), 526 (1991).
9. B. K. Cho, *Journal of Catalysis*, **148** (2), 697 (1994).
10. K. Y. S. Ng, D. N. Belton, S. J. Schmieg and G. B. Fischer, *Journal of Catalysis*, **146** (2), 394 (1994).
11. M. Valden, J. Aaltonen, E. Kuusisto, M. Pessa and C. J. Barnes, *Surface Science*, **307**, 193 (1994).
12. C. Howitt, V. Pitchon and G. Maire, *Journal of Catalysis*, **154** (1), 47 (1995).
13. F. Gao, Y. L. Wang and D. W. Goodman, *Journal of Catalysis*, **268** (1), 115 (2009).
14. G. Ertl, *Reactions at Solid Surfaces* (Wiley, 2009).
15. I. Langmuir, *Transactions of the Faraday Society*, **17**, 607 (1922).
16. J. Misewich, J. H. Glownia, J. E. Rothenberg and P. P. Sorokin, *Chemical Physics Letters*, **150** (5), 374 (1988).
17. M. J. Rosker, M. Dantus and A. H. Zewail, *Science*, **241** (4870), 1200 (1988).
18. G. D. Billing, *Chemical Physics*, **116** (2), 269 (1987).
19. J. C. Tully, *Journal of Chemical Physics*, **93** (2), 1061 (1990).
20. M. Head-Gordon and J. C. Tully, *Journal of Chemical Physics*, **96** (5), 3939 (1992).
21. M. Head-Gordon and J. C. Tully, *Physical Review B*, **46** (3), 1853 (1992).
22. E. Hasselbrink, *Surface Science*, **270**, 235 (1992).
23. S. I. Anisimov, B. Kapeliovich and T. L. Perelman, *Zhurnal Eksperimentalnoi I Teoreticheskoi Fiziki*, **66** (2), 776 (1974).
24. A. P. Miller and B. N. Brockhouse, *Canadian Journal of Physics*, **49**, 720 (1971).
25. C. Kittel, *Introduction to Solid State Physics*. (Wiley, 1996).
26. A. P. Kanavin, I. V. Smetanin, V. A. Isakov, Y. V. Afanasiev, B. N. Chichkov, B. Wellegehausen, S. Nolte, C. Momma and A. Tunnermann, *Physical Review B*, **57** (23), 14698 (1998).
27. P. B. Allen, *Physical Review Letters*, **59** (13), 1460 (1987).
28. D. E. Gray, *American Institute of Physics Handbook* - 3rd ed. (McGraw-Hill, New York, 1972).
29. P. Szymanski, A. L. Harris, N. Camillone III, *Surface Science*, **601** (16), 3335 (2007).
30. G. Blyholder, *Journal of Physical Chemistry*, **68** (10), 2772 (1964).
31. B. Gumhalter, K. Wandelt and P. Avouris, *Physical Review B*, **37** (14), 8048 (1988).

32. P. Avouris and R. E. Walkup, *Annual Review of Physical Chemistry*, **40**, 173 (1989).
33. S. Ohnishi and N. Watari, *Physical Review B*, **49** (20), 14619 (1994).
34. F. Illas, S. Zurita and A. M. Marquez, *Surface Science*, **376** (1-3), 279 (1997).
35. M. Gajdos, A. Eichler and J. Hafner, *Journal of Physics-Condensed Matter*, **16** (8), 1141 (2004).
36. O. Krogh Andersen, *Physical Review B*, **2** (4), 883 (1970).
37. M. Gajdos, A. Eichler and J. Hafner, *Journal of Physics-Condensed Matter*, **18** (1), 13 (2006).
38. F. Delbecq, B. Moraweck and L. Verite, *Surface Science*, **396** (1-3), 156 (1998).
39. D. S. King and R. R. Cavanagh, *Advances in Chemical Physics*, **76**, 45 (1989).
40. D. M. Newns, T. F. Heinz and J. A. Misewich, *Progress of Theoretical Physics Supplement*, (106), 411 (1991).
41. M. Brandbyge, P. Hedegard and T. F. Heinz, *Physical Review B*, **52** (8), 6042 (1995).
42. S. Wagner, *State- and Time-Resolved Investigations of Energy Transfer Mechanisms in Femtosecond Laser Induced Associative Desorption*. (PhD Thesis, Berlin, 2006).
43. F. Budde, T. F. Heinz, A. Kalamarides, M. M. T. Loy and J. A. Misewich, *Surface Science*, **283** (1-3), 143 (1993).
44. L. M. Struck, L. J. Richter, S. A. Buntin, R. R. Cavanagh and J. C. Stephenson, *Physical Review Letters*, **77** (22), 4576 (1996).
45. H. Risken, *The Fokker-Planck Equation*. (Springer, 1989).
46. J. A. Misewich, T. F. Heinz and D. M. Newns, *Physical Review Letters*, **68** (25), 3737 (1992).
47. J. C. Tully and M. Head-Gordon, *Desorption Induced by Electronic Transitions DIET V*, eds. A. R. Burns, E. B. Stechel (Springer-Verlag, Berlin, 1993).
48. D. Menzel and R. Gomer, *Journal of Chemical Physics*, **41** (11), 3311 (1964).
49. P. A. Redhead, *Canadian Journal of Physics*, **42** (5), 886 (1964).
50. P. R. Antoniewicz, *Physical Review B*, 21, 3811 (1980)
51. C. Frischkorn and M. Wolf, *Chemical Reviews*, **106** (10), 4207 (2006).
52. F. J. Kao, D. G. Busch, D. Cohen, D. G. Dacosta and W. Ho, *Physical Review Letters*, **71** (13), 2094 (1993).

53. M. Bonn, S. Funk and C. Hess, *Science*, **285** (5430), 1042 (1999).

54. J. A. Prybyla, T. F. Heinz and J. A. Misewich, *Physical Review Letters*, **64** (13), 1537 (1990).

55. S. Funk, M. Bonn, D. N. Denzler, C. Hess, M. Wolf and G. Ertl, *Journal of Chemical Physics*, **112** (22), 9888 (2000).

56. P. Szymanski, A. L. Harris and N. Camillone III, *Journal of Physical Chemistry A*, **111** (49), 12524 (2007).

CHAPTER 2

EXPERIMENTAL APPARATUS AND DIAGNOSTICS FOR FS-LID

2.1 Introduction

In this chapter, a detailed description of the experimental setup for femtosecond laser-induced desorption (fs-LID) is provided. The setup consists of an ultra-high vacuum (UHV) chamber and an amplified femtosecond laser system delivering 800 nm laser pulses that is also used for extreme ultraviolet (XUV) generation (described in detail in Chapter 3). After a description of the vacuum chamber and the laser systems, the diagnostic experimental methods (methods for beam waist and pulse duration measurements, reflection absorption infrared spectroscopy (RAIRS) and temperature programmed desorption (TPD)) are explained. The chapter ends with a brief description of how the photodesorption experiments described in this thesis (Chapter 4 and Chapter 5) were performed.

2.2 UHV chamber

The UHV chamber in which all of the experiments described in this thesis were performed, was designed before the start of this PhD. However, the components were assembled and tested during the course of these studies. The chamber has two levels: an upper level designed for TPD and fs-LID experiments, and a lower level for cleaning the sample and for RAIRS experiments. In Figure 2.1 a photograph of the UHV chamber is shown. Figure 2.2 is a schematic diagram showing the positions and orientations of the ports in the UHV chamber.

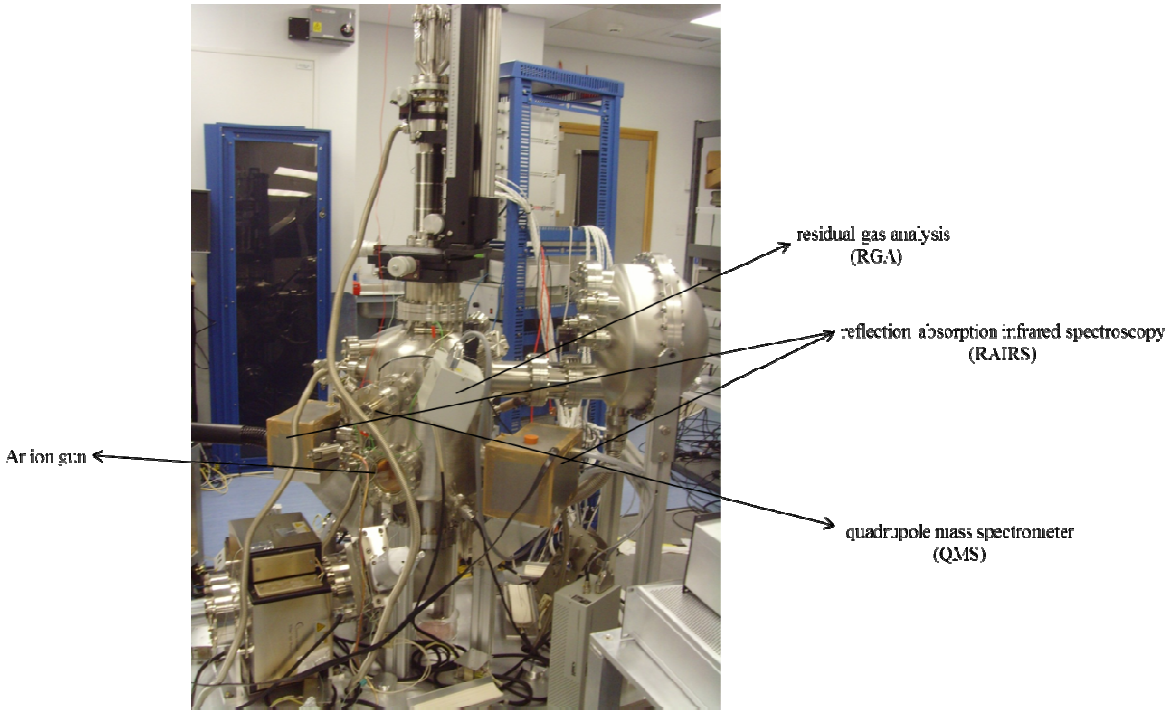

Figure 2.1 UHV chamber

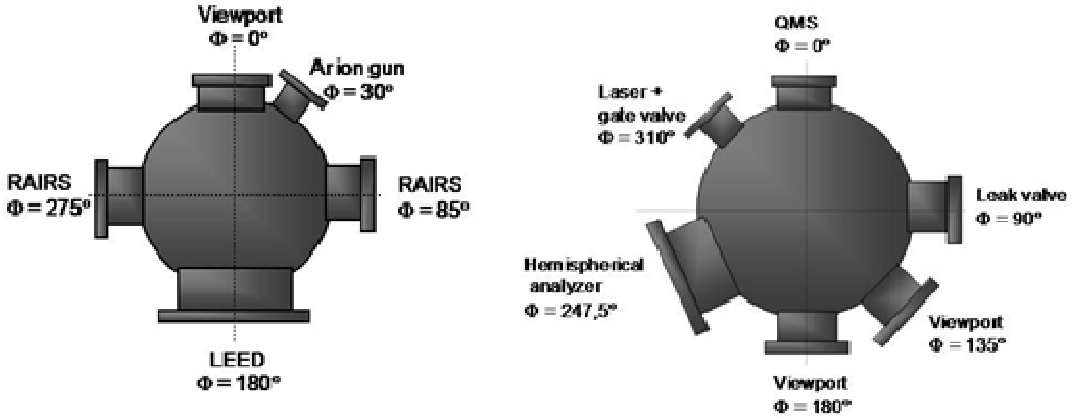

Figure 2.2 The arrangement of the ports (viewed from above) on the UHV chamber: lower level (left) and upper level (right).

The upper level of the home built UHV chamber is equipped with a port which will eventually connect the UHV chamber with the XUV radiation source (described in Chapter 3) for future time-resolved photoelectron spectroscopy (TRPES) experiments, a quadrupole mass spectrometer (HAL 3F/PC, Hiden Analytical) for TPD and

femtosecond LID experiments and a hemispherical analyzer (Scienta R3000, VG) for measuring the kinetic energies of the photoemitted electrons in TRPES experiments. The lower level consists of infrared optics for RAIRS experiments (Nicolet 6700), optics for LEED and Auger electron spectroscopy (AES) (Specs), an argon ion gun (IQE 11/35, SPECS) for sample cleaning, equipped with a valve for leaking gas into the chamber, a residual gas analyser (RGA) (Hiden), an ion gauge and a vacuum pumping system. The vacuum pumping system consists of a turbo-molecular pump (Turbovac 361, Leybold) backed by a rotary pump (Trivac D8B, Leybold), with further pumping provided by ion and titanium sublimation pumps (Gamma vacuum). The chamber is also fitted with multiple view ports to allow observation of the sample during positioning in the chamber. The entire sample assembly (Section 2.3) is mounted on a precision manipulator (Omniax Translator, MX series, Vacuum Generators, UK) which permits translation along the *x*, *y* and *z* axes and 360˚ rotation. The sample can therefore be positioned accurately within the chamber. For both sample cleaning and adsorption experiments, gases must be leaked into the chamber in a controlled manner. A gas manifold allows this process to take place. It is made from stainless steel to maintain the purity of the gases and to prevent corrosion. The gas manifold is evacuated using a turbo-molecular pump (Turbovac 50, Leybold), which is backed by a rotary pump (D4B, Leybold). The chamber also has two differentially pumped windows (for RAIRS) which are pumped by a rotary pump. The chamber is baked at 120 ˚C for 24 hours allowing a base pressure of around 10^{-10} mbar to be obtained. In the next two sections, the sample cleaning procedure and sample heating design will be explained.

2.3 Sample cleaning procedure

A single crystal Pd(111) surface has been used in all of the experiments described in this thesis. In order to perform an experiment on a well-defined single crystal surface, it is necessary that the surface is clean before the experiment starts. An everyday cleaning procedure performed prior to each of the experiments consisted of Ar^+ sputtering at 1 keV, then annealing to 1100 – 1200 K, cooling in oxygen, and again, brief annealing. Sputtering, annealing and chemical cleaning are standard cleaning techniques in surface science. Sputtering is a technique that involves a high energy beam of inert gas ions colliding with the surface and removing the atoms from the top surface layers. The

disadvantage of this technique is that the surface is left in a heavily damaged state, usually with embedded inert gas atoms, so it must be annealed to restore the order. Annealing involves heating to a high temperature, at which the surface atoms become mobile and reorder themselves, and any impurity atoms such as sulfur or carbon are brought to the subsurface region from the bulk. These impurities are the reason why the initial cleaning procedure involves many cycles of sputtering and annealing to deplete the impurities in the subsurface region. By chemically cleaning the surface, impurities are removed in the form of compounds that are easily desorbed from the surface such as CO, CO_2 or H_2O.

2.4 Sample heating design

The design of the heating system was important in order to ensure that cooling of the sample to liquid nitrogen temperature (77 K), and heating to the annealing temperature required for the cleaning procedure (1100 - 1200 K) were both possible. The sample temperature was measured using a K-type thermocouple in the 300-1200 K range.

In order to reach the very high temperatures required for annealing, a resistive heating system was used. This set-up enabled us to reach very high annealing temperatures in the cleaning cycle as well as to achieve the well-controlled and constant heating rate necessary for TPD experiments, as shown in Figure 2.3.

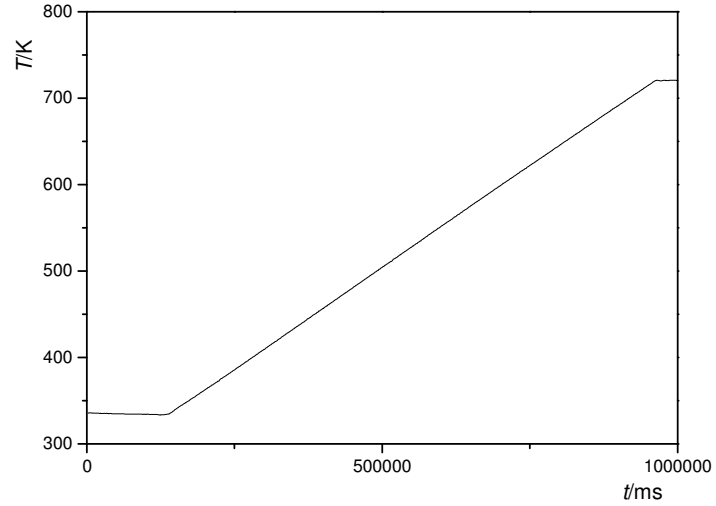

Figure 2.3 A plot showing temperature *vs* time during one of the TPD experiments.

To reach liquid nitrogen temperatures, a cold-finger is located in the middle of manipulator. A copper sample mount is on the end of the cold-finger. The copper sample mount consists of four layers, as shown in Figure 2.4c: in the first layer, there are two copper blocks, in the second layer there is a sapphire plate, in the third layer there is a heat exchanger made of copper, and in the last layer there is a sapphire plate. The first and last layers can be seen in figures 2.4a and 2.4b, respectively. The whole assembly is tightened with bolts covered in ceramic pieces.

Into the two copper blocks, Kapton-coated copper wires that provide current for the resisitive heating are introduced. The copper blocks need to be electrically insulated from each other, hence there is a ceramic disc placed between them. The copper blocks also need to be electrically, but not thermally, insulated from the heat exchanger. For that purpose, a sapphire disc is used. The sapphire disc is an electrical insulator and it has maximum thermal conductivity at very low temperatures which allows the efficient cooling of the sample. It has a poor high temperature conductivity, preventing the transfer of heat from the sample to the coldfinger. A tantalum rod with two arms is attached to each of the copper blocks, and heating wires made from 75% tungsten and 25% rhenium are spot welded to the tantalum arms and to the back of the sample. The spot welding at the back of the sample is performed in the following way: first, thin tantalum foil is spot welded to the back of the sample, then the heating wires with a piece of tantalum foil above each of them are spot welded to the thin tantalum foil; finally, the thermocouple is spot welded to the edge of the tantalum foil and the heating wires are spot welded to the four horizontal arms of the tantalum rods.

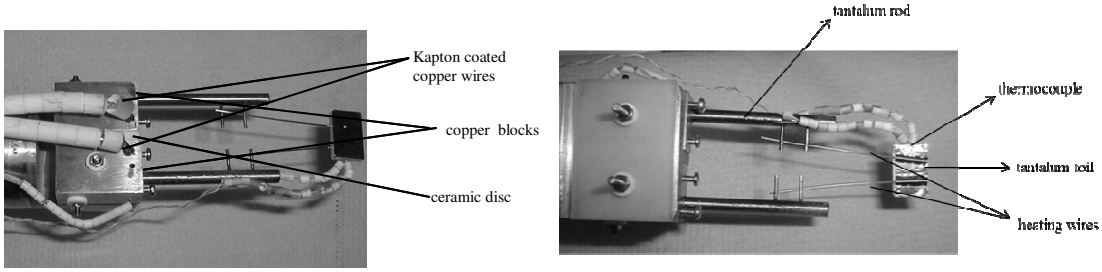

a) b)

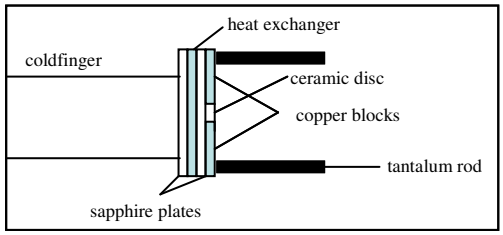

c)

Figure 2.4 The sample mount photos and a schematic: a) front view; b) at the back of the sample; c) lateral cross section.

The resistive heating system appeared to be efficient for 1 – 2 months. After this time, the heating wires, or thin tantalum foil or thermocouple (or all of them) start to detach from the sample. The main cause of this inefficiency is the repeated cycling of heating and cooling of the sample during the cleaning procedure. When this happens, the sample mount needs to be changed. Replacing a sample mount is a complicated procedure because taking the sample manipulator out of the chamber requires a change in the position of the optical table and lenses in front of the UHV chamber. An additional problem is that the mount is not rigid, so the position of the surface normal relative to the axis of the QMS will not be exactly the same when it is replaced. Every time the sample mount is replaced, additional testing needs to be carried out to make sure that the fs- LID experiments (described in detail in Section 2.9), with the different mounts, could be compared within reasonable error limits. The additional testing consisted of using the internal standard, mass 28 (CO) adsorbed on Pd(111) at saturation coverage. The photodesorption yield after the first laser pulse was measured for a few laser fluences for each of the sample mounts. When the results agreed within 10% of earlier results, the aligning procedure is finished.

2.5 Femtosecond laser system

The theory of the generation of femtosecond laser pulses is presented in Appendix A. The femtosecond laser system used for femtosecond LID experiments and for the generation of femtosecond XUV radiation consists of an oscillator (Coherent Micra) and a chirped pulse regenerative amplifier (Coherent Legend). Figure 2.5 shows a schematic diagram of the laser system. The oscillator produces pulses of 15 fs duration with 100 nm bandwidth and a pulse energy of 4 nJ at a repetition rate of 80 MHz. The chirped pulse regenerative amplifier has three parts: a stretcher, a regenerative amplifier and a compressor. It typically provides pulses of 40 fs duration with a pulse energy of 2.5 mJ at a central wavelength of 790 nm. The repetition rate can be adjusted manually between 1 kHz and 10 Hz.

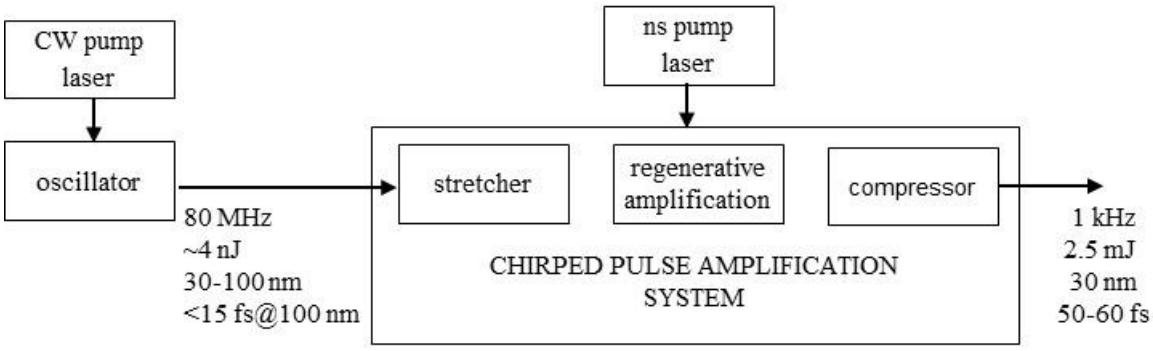

a)

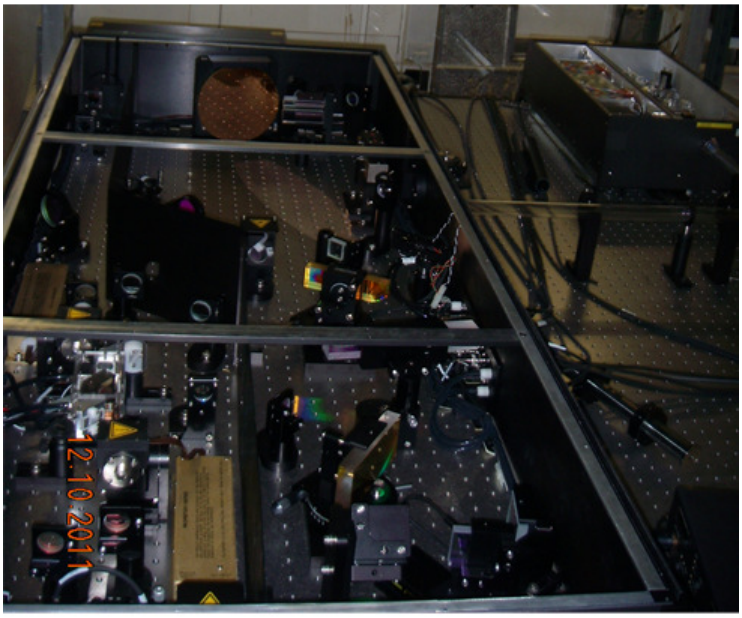

b)

Figure 2.5 a) Schematic of the drive laser system. b) Photo of the drive laser system.

2.5.1 Femtosecond oscillator

Weak femtosecond laser pulses are generated by a modelocked oscillator (Coherent Micra), shown in detail in Figure 2.6. The Micra relies on Kerr lens modelocking (KLM) to generate broadband modelocked output pulses (see Appendix A for a description of KLM). The Micra system is pumped by the output of a frequency doubled Nd:YVO_4 laser (Coherent Verdi). The broadband pulses are generated between two end mirrors: a highly reflective end mirror (HR1) and a partially reflective output coupler (OC). There are two paths of the fluorescence through the Ti:sapphire crystal, backwards and forwards, and they are shown in Figure 2.6 by red and black solid lines, respectively. The bandwidth can be adjusted, by changing the amount of the negative dispersion compensation, from 30 to 100 nm, together with tuning the slit. The central wavelength can also be adjusted by tuning the slit and the HR1 mirror. Neither of these adjustments were used in the experiments performed here. All of the experiments were performed with the slit fully opened. The HR4 mirror has a crucial part in starting the modelocking by introducing noise into the system. After the output coupler, a beam splitter sends the laser beam to the photodiode assembly that measures the power of the laser operating in a CW or modelocked mode. P is the power track mirror – it is a piezo driven mirror to maintain the optimum pump beam alignment into the oscillator, as measured by one of the photodiodes.

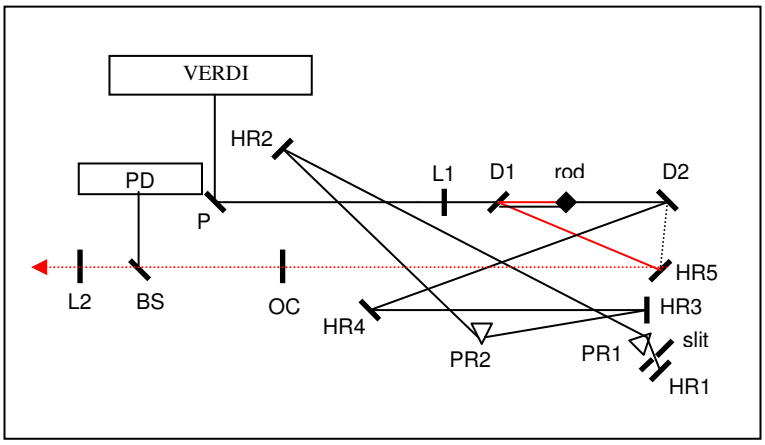

Figure 2.6 Micra Ti:Sapphire oscillator optical schematic. Rod = Ti:Sapphire laser crystal; D1, D2 = curved cavity mirrors; HR1 = high reflectivity end mirror; HR2-HR5 = high reflectivity cavity folding mirrors; P = power track mirror; OC = output coupler; PR1 and PR2 = intracavity fused silica prisms; slit = intracavity slit; L1 = pump focusing lens; BS = beamsplitter; PD = fast and slow photodiode assembly. The end cavity mirrors are HR1 (100% mirror) and the output coupler. The two paths of the fluorescence are denoted by red and black lines.

2.5.2 Chirped pulse regenerative amplifier

The pulses from the oscillator are sent into a chirped pulse amplification (CPA) system (Figure 2.7) which is pumped by a nanosecond Q-switched Nd:YLF laser (Coherent Evolution).

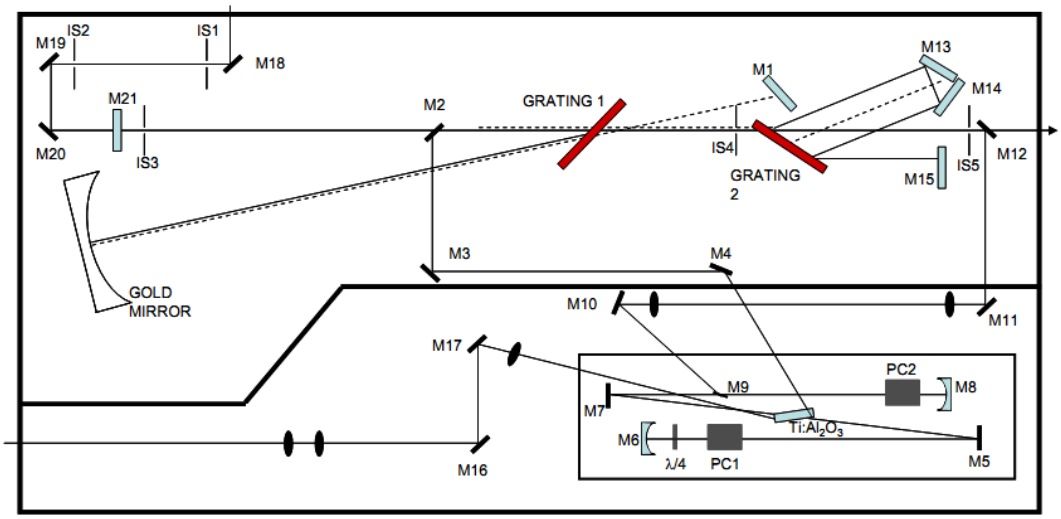

Figure 2.7 Schematic diagram showing the optical layout of the Coherent Legend amplifier for the chirped pulse amplification system. Femtosecond pulses from the oscillator first enter the stretcher *via* mirrors M18-M20. After four passes, pulses are sent *via* mirrors M2 – M4 to the regenerative laser cavity. The regenerative laser cavity consists of a Ti:Sapphire crystal that is pumped from both sides by a frequency doubled Nd:YLF laser, two end mirrors (M6 and M8), two folding mirrors M5 and M7, two Pockels cells (PC1 and PC2) and a λ/4 waveplate. While in the resonator, the pulse experiences a gain of over 10^6. The pulse then enters the compressor part of the amplifier that consists of a diffraction grating and another set of mirrors M13-M15. In the compressor, grating 2 induces a negative chirp to the pulse to compensate for the positive chirp induced by the stretcher. Figure taken from reference 1.

Femtosecond pulses from the oscillator first enter the stretcher. The stretcher consists of a diffraction grating, a gold mirror and a retroreflective mirror. The stretcher induces a positive chirp on the femtosecond pulses so that they are lengthened temporally to picosecond duration. After four passes, the pulses are sent to the regenerative laser cavity. The regenerative laser cavity consists of a Ti:Sapphire crystal that is pumped from both sides by the frequency doubled output of a nanosecond Nd:YLF laser, two end mirrors, two folding mirrors, two Pockels cells (PC1 and PC2) and a $\lambda/4$ waveplate. The Pockels cells and $\lambda/4$ waveplate are part of the optical switch. The femtosecond laser pulse enters the resonator by reflection off the laser window. The pulse passes

through PC1 and the $\lambda/4$ waveplate and is reflected by mirror M6 and retraces its path. The first Pockels cell also acts as a $\lambda/4$ waveplate, so it negates the effect of the first waveplate. After a number of round trips (usually about 20), the second Pockels cell switches on, causing a half-wave rotation to the pulse, and the pulse is ejected from the resonator by a polarizer. While in the resonator, the pulse experiences a gain of over 10^6. The pulse then enters the compressor part of the amplifier that consists of a diffraction grating and a set of mirrors. In the compressor, the grating induces a negative chirp on the pulse to compensate for the positive chirp induced by stretcher.

2.6 Temporal laser pulse profile

An ultrashort laser pulse is a very short burst of electro-magnetic energy. The pulse, like any light wave, is defined by its electric field as a function of space and time, $E(x, y, z, t)$. In this section, the spatial portion of the electric field will be ignored. [2] The temporal dependence of the electric field of an ultrashort pulse can be described by Equation 2.1:

$$E(t) = \frac{1}{2}\sqrt{I(t)}\exp\{i[\omega t - \phi(t)]\} \tag{2.1}$$

where t is time, ω is the carrier angular frequency, and $I(t)$ and $\phi(t)$ are the time dependent intensity and the phase of the pulse, respectively. The pulse field can also be defined in the frequency-domain as a Fourier transform of the time-domain field. In that case, instead of the intensity and temporal phase $\phi(t)$, there is a spectrum, $S(\omega)$, and spectral phase, $\varphi(\omega)$. [2] The temporal and spectral phases are usually expanded as Taylor series around the central time, t_0, and the central frequency, ω_0, respectively:

$$\varphi(t) = \varphi(t_0) + \varphi'(t - t_0) + \frac{1}{2}\varphi''(t - t_0)^2 + \ldots \tag{2.2}$$

and

$$\varphi(\omega) = \varphi(\omega_0) + \varphi'(\omega - \omega_0) + \frac{1}{2}\varphi''(\omega - \omega_0)^2 + \ldots \tag{2.3}$$

The linear chirp, $\varphi''(\omega)$, in the frequency domain is called the group-delay dispersion (GDD). Group velocity dispersion (GVD) is usually expressed as the amount of GDD per unit length, usually measured in units of fs^2/ mm. [2] The second and other higher

order terms are the result of passing an ultrashort pulse through any medium. The short pulse has a very large bandwidth, and the frequency dependence of the refractive index of a material over that wavelength range will produce a temporal stretch of the pulse (a chirp).

When the laser system generating the pulse is ideal (without a chirp), then the approximate duration of a pulse can be obtained from a spectral bandwidth measurement. The spectral bandwidth can be related to the minimum pulse duration by the time-bandwidth product,

$$\Delta\nu\Delta t \geq 0.441. \qquad (2.4)$$

Together, the duration, Δt, and the bandwidth, $\Delta\nu$, are the fundamental properties of the ultrashort pulse. Light frequency, ν is defined as the angular frequency, ω divided by 2π. The bandwidth is defined as the full-width at half maximum (FWHM) of the frequency–domain intensity profile, $I(\nu)$, and the duration is defined as the FWHM of the time-domain intensity profile, $I(t)$, of the pulse. The bandwidth for the laser system used in this thesis is 1.2×10^{13} Hz, which corresponds to a duration of 40 fs for an ideal, unchirped pulse. The true pulse duration straight out of the amplifier was measured by a single-shot autocorrelator (see below). In all experiments, the autocorrelation width was about 50-60 fs, indicating that the pulse is chirped.

Autocorrelation using a second harmonic generation (SHG) crystal is the simplest method for measuring a pulse duration of a femtosecond laser. In a SHG autocorrelation measurement, the pulse is overlapped with a delayed replica of itself (produced using a beamsplitter and an optical delay line) in a nonlinear crystal and a signal will be detected at twice the frequency of the input pulse frequency. The magnitude of the frequency doubled signal will be proportional to the square of the temporal overlap of the two pulses. Hence the resulting measure of SHG intensity as a function of time will give an indication of the duration of the input laser pulses. For a Gaussian pulse profile, the autocorrelation intensity signal has a FWHM that is $\sqrt{2}$ times the duration of the electric-field pulse. The typical spectrum of an ultrashort pulse, $I(\lambda)$, and its temporal intensity, $I(t)$, are shown in figures 2.8 and 2.9, respectively.

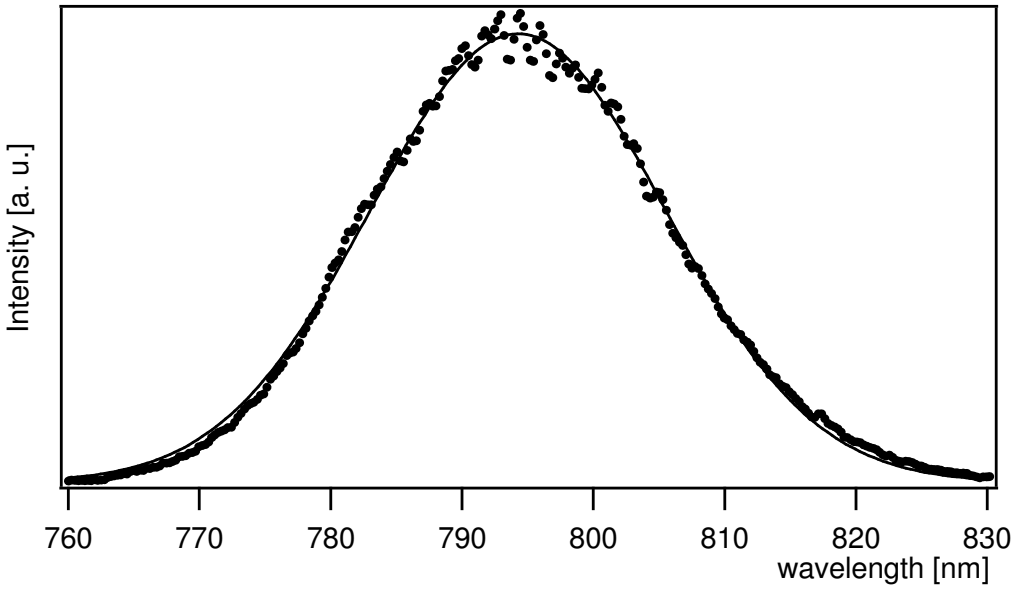

Figure 2.8 Spectrum of the amplified laser pulse. Assuming Gaussian shaped pulses (lines), one obtains a spectral FWHM of 25 nm.

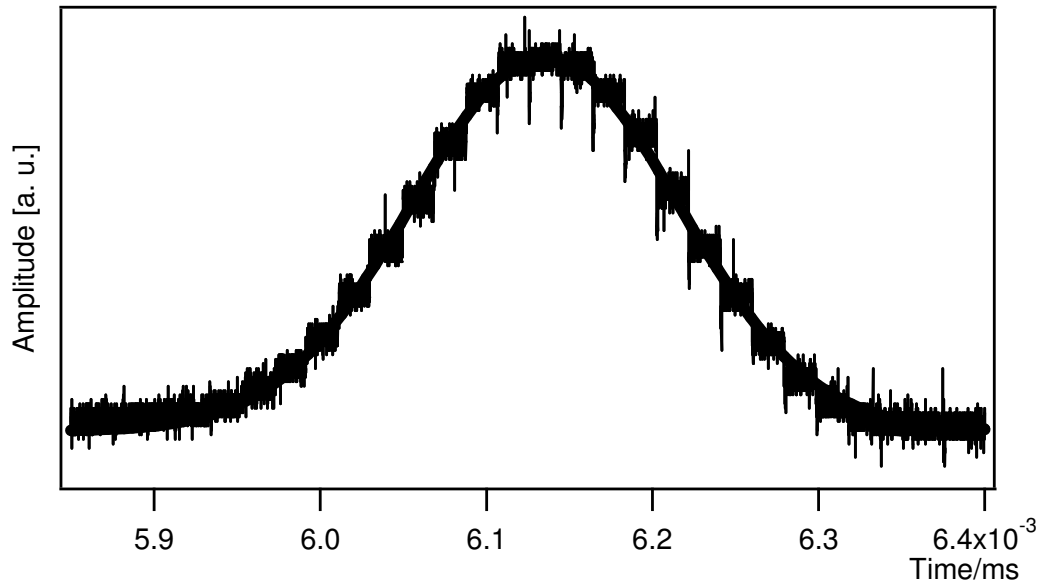

Figure 2.9 An autocorrelation trace obtained on an oscilloscope from the single shot autocorrelator. Assuming a Gaussian shaped pulse (line), one obtains a FWHM of 189 μs. The calibration factor is 0.417 fs/μs, so the autocorrelated width is 79 fs, and the Gaussian pulse width is 56 fs.

The pulse duration at the sample was not measured, but it was calculated roughly from Equation 2.5:

$$\Delta t_{new} = \sqrt{\Delta t^4 + (4\varphi'' \ln 2)^2} \,/\, \Delta t \qquad (2.5)$$

where the factor φ'' is a GDD that can be calculated from a literature value of GVD or is itself found in literature, Δt is the initial time duration and Δt_{new} is the new time duration. [3]

In this experimental set-up there were numerous materials through which the laser pulse passed: 5 m through air from the amplifier to the sample, 4 broadband 45° mirrors, a ½ achromatic waveplate made of quartz and MgF_2, a polarising beam splitter, a pair of lenses (converging and diverging) and a fused silica window 2 mm thick. GDD was calculated for almost all of them: air (100 fs^2), ½ achromatic waveplate made of quartz and MgF_2 (45 fs^2), polarising beam splitter (140 fs^2), and fused silica window 2 mm thick (72 fs^2). Based on the above, a 56 fs pulse centred at 800 nm will be stretched to 59 fs when passing from the amplifier to the sample, which is not significant.

2.7 Beam waist measurement

For an accurate measure of the laser fluence, we require a measure of the laser pulse spatial profile. The intensity beam profile was measured by placing a knife blade on a translation stage and stepwise moving the blade through the beam. Behind the blade was a power meter which measured the power at each point from when the blade completely blocks the pulse to when the whole beam passes the blade. This process is performed in both the *x* and *y* directions. As the blade moves across the beam, the power changes from a maximum to zero, as shown in Figure 2.10.

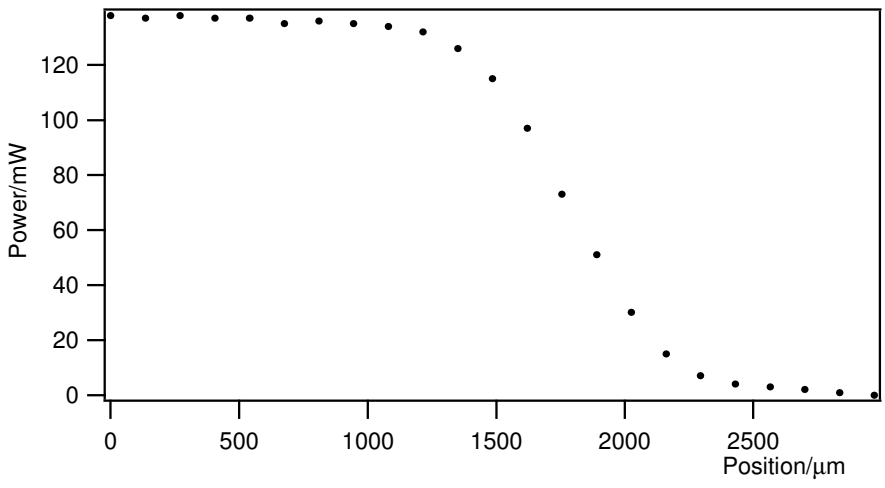

Figure 2.10 Changes in power as a knife blade moves through the beam in the *x* direction for the third sample mount.

In order to obtain the intensity for a particular position in the *x* or *y* direction, the first derivative of the power with respect to *x* or *y* at that position needs to be taken. The step size of the translation stage is very small (133 μm) and is constant through the beam, so that the first derivative in this case is proportional to the power difference between the adjacent positions of a translation stage. The intensity distribution that results from the power distribution shown by Figure 2.10 is shown in Figure 2.11.

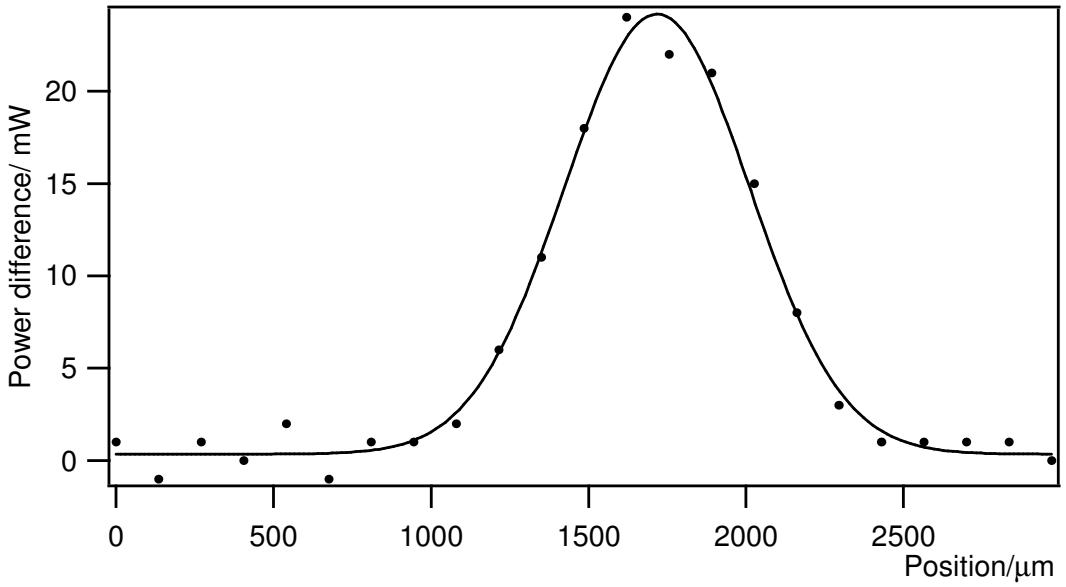

Figure 2.11 Intensity as a function of the position across the beam in the *x* direction for third sample mount. It can be seen that the intensity distribution can be represented well by a Gaussian.

From Figure 2.11 it can be seen that the intensity distribution is approximately Gaussian. The next step is to define the laser fluence. The laser fluence can be defined as the intensity at a particular point within the beam divided by the laser repetition rate. The relation between the laser fluence and the energy per pulse is the same as the relation between the laser intensity and the laser power.

The average energy per pulse can be calculated from Equation 2.6:

$$E = \frac{P_{\text{average}}}{\text{repetition rate}} \tag{2.6}$$

The intensity or fluence beam profile could be fitted by an elliptical Gaussian function, and the average fluence then follows from Equation 2.7:

$$E = \int F(r)dr$$
$$E = \iint F \exp\left[-\left(\frac{(x-x_0)^2}{a^2} - \frac{(y-y_0)^2}{b^2}\right)\right]dxdy \tag{2.7}$$
$$F = \frac{E}{ab\pi}$$

where $F(r)$ is the fluence spatial profile with x and y the spatial coordinates in the plane of the sample. x_0 and y_0 are the mean values, and together with a and b parameters can be calculated from the Gaussian fit. Parameters a and b are related to the standard deviation, σ:

$$a = \sqrt{2}\sigma(x)$$
$$b = \sqrt{2}\sigma(y) \tag{2.8}$$

It was mentioned earlier in this Chapter (Section 2.4) that the design of the sample mount is such that it needs to be replaced every few months. For the experiments described in this thesis, three sample mounts were used for photodesorption experiments. A charge coupled device (CCD) beam profile camera was also used to measure the beam profile for the first two mounts. The camera was borrowed from Coherent inc, and was designed for nanosecond pulses. The femtosecond pulses in all experiments had an average energy per pulse of 1.5 mJ and a very high peak power so that the camera was easily saturated. The femtosecond laser pulses therefore had to be attenuated by a factor of more than 1000 times. This required using a combination of a waveplate and polarizing beam splitter and reflective neutral density filters. The a and b parameters required for the fluence calculations could be obtained from BeamView-USB Analyzer software which gave a Δx (Δy) value equal to twice the difference between the points ($x_0(y_0)$ + $a(b)$) and ($x_0(y_0)$ − $a(b)$). Hence, Δx (Δy) is four times the parameter a or b, respectively. Figures 2.12 and 2.13 show the intensity profiles obtained by the knife edge method and the CCD beam profile camera. The measurements obtained by these two methods are within 10% of each other.

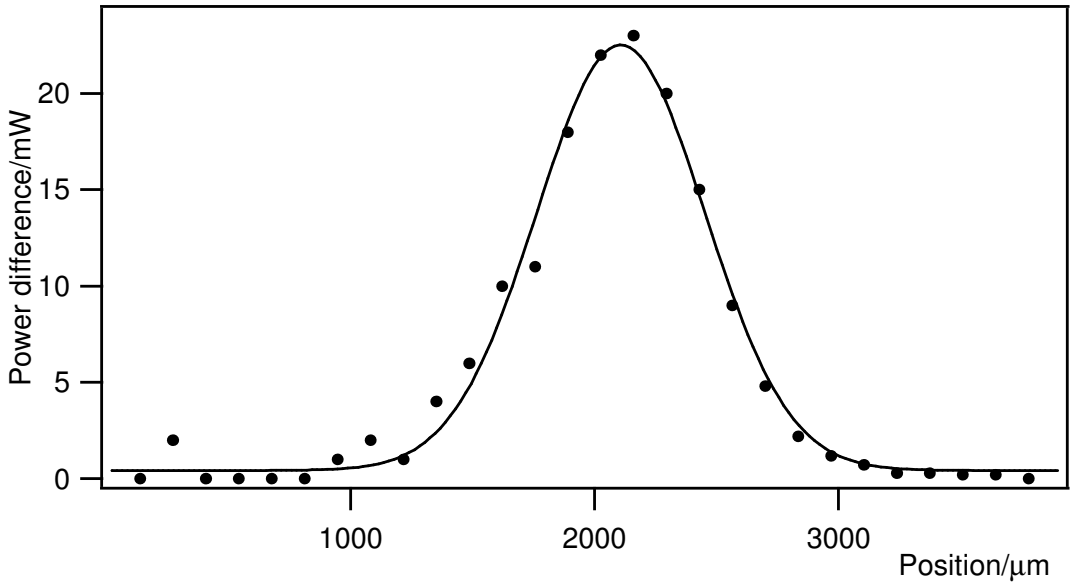

Figure 2.12 Intensity beam profile in x direction obtained by knife edge method. The parameter a is obtained from the Gaussian fit to the data: $a = 487 \pm 14$. This figure represents the intensity beam profile for the first mount.

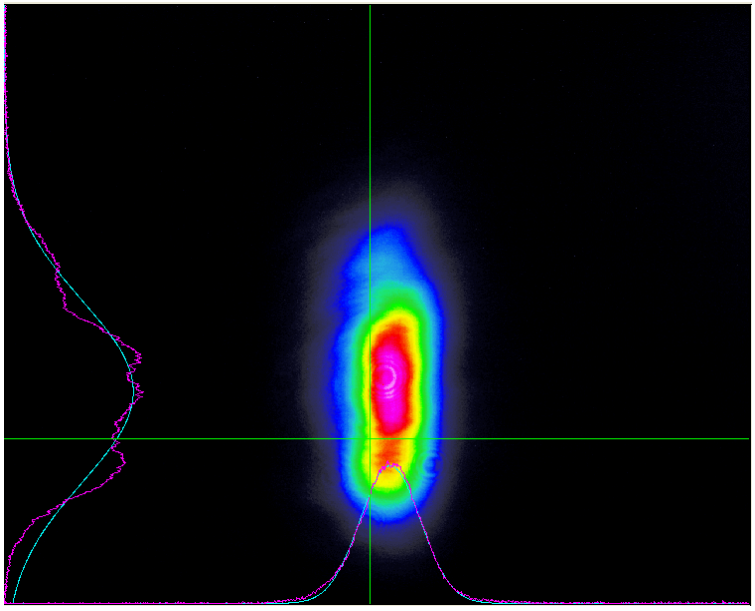

Figure 2.13 The beam profile measured at 100 Hz by the CCD beam profile camera. Δx is 1653 µm, Δy is 4204 µm. These values are obtained for the first mount.

Parameters a, b for sample mounts used in all the fs-LID experiments obtained by the knife edge method or by the CCD are shown in Table 2.1.

Table 2.1 Parameters *a*, *b* obtained for the three sample mounts used in all of the experiments performed in this thesis. Parameters are obtained using either the knife edge method or the beam profile CCD camera. Values presented have approximately 10% error.

	Knife edge method		CCD		system
Mount 1	a = 470 μm		a = 410 μm	$b = 10^3$ μm	10 L CO (^{13}CO) 10 L NO 4 L ^{13}CO/ 2 L NO
Mount 2	a = 330 μm		a = 380 μm	$b = 10^3$ μm	2 L ^{13}CO/ 2 L NO
Mount 3	a = 280 μm	b = 990 μm			2 L NO/ 2 L ^{13}CO
	a = 410 μm	b = 990 μm			4 L NO/ 2 L ^{13}CO (2, 4) L NO (2, 4) L ^{13}CO

2.8 Experimental techniques

2.8.1 RAIRS

Reflection absorption infrared spectroscopy (RAIRS) is a powerful vibrational spectroscopic technique for studying adsorbates on metal surfaces. It allows identification of adsorbate species as well as giving information about binding geometry. The standard experimental set-up is shown in Figure 2.14. [4-6]

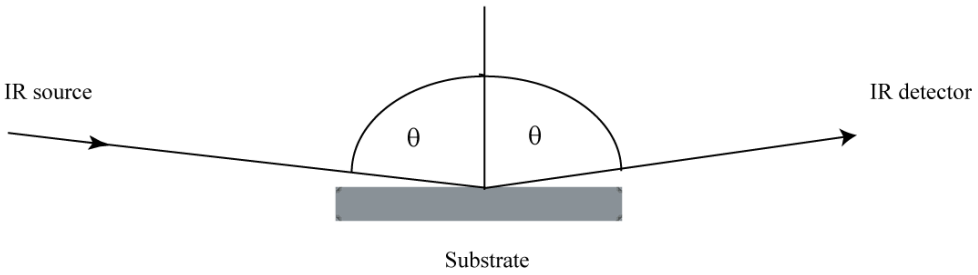

Figure 2.14 Schematic of RAIRS set up. Angle θ is nearly 90˚.

Broadband infrared (IR) radiation is passed through an IR transparent window onto the sample surface at grazing incidence. The sample reflects the light, which is then directed onto a detector such as a mercury cadmium telluride (MCT) detector.

The IR spectrum of the adsorbate is recorded by monitoring the absorption of IR light reflected from the substrate. Vibrational excitation of the molecules is based on the interaction of the electromagnetic field of the incident infrared radiation with the dipole moment of the molecule. The spectrum is therefore produced in the form of $\Delta R/R$ *vs* wavenumber, where ΔR denotes the difference in reflectivity between the clean and adsorbate covered metal surface and R denotes the reflectivity of the clean metal sample. Grazing angles are required because of the metal surface selection rule (see below). Grazing incidence also increases the sensitivity as the path of infrared light through the adsorbing layer is increased by increasing the incidence. The *s*-polarized component of the electric field (perpendicular to the plane of incidence) reverses in phase upon reflection for all angles of incidence, so that the resultant field at the surface is approximately zero. The *p*-polarized component of light (parallel to the plane of incidence) changes very little in phase and the resulting local field is almost doubled. Consequently, the *p*-polarized component of light can interact only with vibrational modes that give rise to a change of the electric dipole perpendicular to the surface. Another way to look at the surface selection rule is to consider the response of the valence electrons of the substrate to vibrations of the adsorbate, as shown in Figure 2.15 for a CO molecule on a surface. It can be seen that the polar CO molecule induces an image charge in the substrate. In the upright configuration, molecular and image dipoles re-enforce each other giving rise to strong IR absorption, but for a molecule that is aligned parallel to the surface the molecular and image dipoles cancel out, so there is no IR absorption in this case.

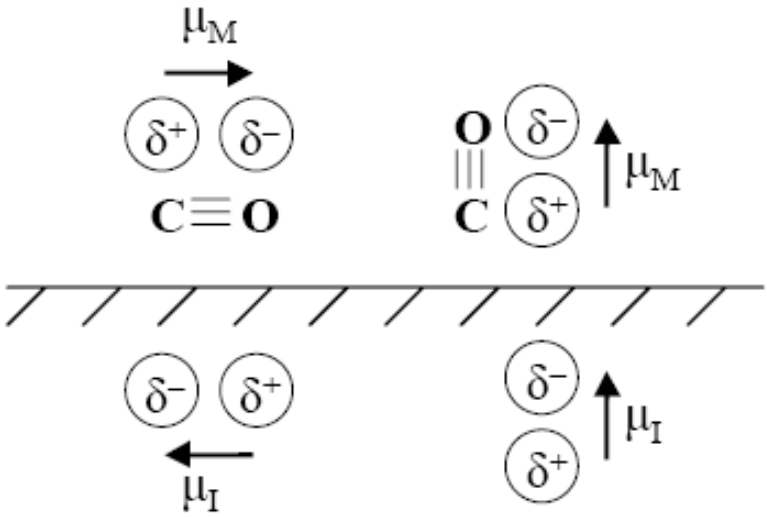

Figure 2.15 Illustration of the surface selection rules in terms of the molecular, μ_M and image, μ_I dipoles. Figure taken from reference 4.

The study of vibrational modes in the very low energy region, corresponding to adsorbate-substrate vibrations, is limited by the window materials available (for NaCl 600 cm^{-1} and KBr 400 cm^{-1}) and detectors that show inadequate sensitivity in this region. This means that attention is instead concentrated on the intrinsic vibrations of the adsorbate species in the range 600 cm^{-1}-3600 cm^{-1}. [4-6]

2.8.2 TPD

Temperature programmed desorption (TPD) involves monitoring of the desorption process as a function of temperature. Analysing TPD spectra may yield the activation energy of desorption and the relative and absolute (in combination with LEED) surface coverage. The experimental set up requires a method for heating the sample so that the heating rate is constant in time (resistive heating), monitoring the temperature of the sample (thermocouple), and a mass detector positioned close to the sample to detect desorbing species. The mass detector used for the TPD experiments was a quadrupole mass spectrometer (QMS) positioned so that the surface normal points to the ionisation volume of the QMS. The sample was linearly and uniformly heated by resistive heating.

During heating, the temperature, the partial pressure of the desorbing species and the time were all recorded. It was possible to record data for up to 5 masses in one experiment.

The rate of desorption can be described by the Polanyi-Wigner equation [4]:

$$r_{des} = -\frac{\partial \vartheta}{\partial t} = \nu_n \vartheta^n \exp\left(-\frac{E_{des}}{RT_s}\right). \tag{2.9}$$

This equation relates the rate of the desorption (r_{des}) to the surface coverage (ϑ), pre-exponential factor (ν), order of desorption (n), the temperature of the surface (T_{s}) and the energy of desorption (E_{des}). The order of desorption, n relates to the way the adsorbate molecule leaves the surface. In first order desorption, as the molecule is heated it leaves the surface in a one-step process. However, desorption is rarely this simple. Desorption usually occurs in combination with other surface processes such as diffusion, recombination of atoms at the surface or surface mediated reactions. These desorption processes are second or higher order. Equation 2.9 can be rewritten for first and second order desorption, where T_{p} is the temperature at which maximum desorption occurs, and β is the applied heating rate:

$$\frac{E_{\mathrm{des}}}{RT_{\mathrm{p}}^2} = \frac{\nu}{\beta}\exp\left(\frac{-E_{\mathrm{des}}}{RT_{\mathrm{p}}}\right), \tag{2.10}$$

$$\frac{E_{\mathrm{des}}}{RT_{\mathrm{p}}^2} = \frac{2\nu^2}{\beta}\theta\exp\left(\frac{-E_{\mathrm{des}}}{RT_{\mathrm{p}}}\right). \tag{2.11}$$

These equations show that for first-order desorption, the position of the maximum desorption does not depend on surface coverage, while it shifts towards lower temperatures for second order desorption. [4-7] In the studies presented in this thesis, the pre-exponential factor was not known, therefore, as a first approximation to obtain the desorption energy for first order desorption, the Redhead equation [8] is used,

$$E_{\mathrm{des}} = RT_p\left[\ln\left(\frac{\nu T_p}{\beta}\right) - 3.46\right]. \tag{2.12}$$

In Equation 2.12, ν is assumed to be 10^{13} s^{-1}, which is the approximate frequency of the adsorbate-surface vibration.

2.9 Photodesorption experiments on Pd(111)

Having discussed the details of the experimental components as well as the diagnostic experimental methods in the previous sections, the purpose of this section is to describe the realization of the main surface science experiments described in this thesis**.** A schematic representation of the experimental set-up for laser-induced desorption experiments is shown in Figure 2.16.

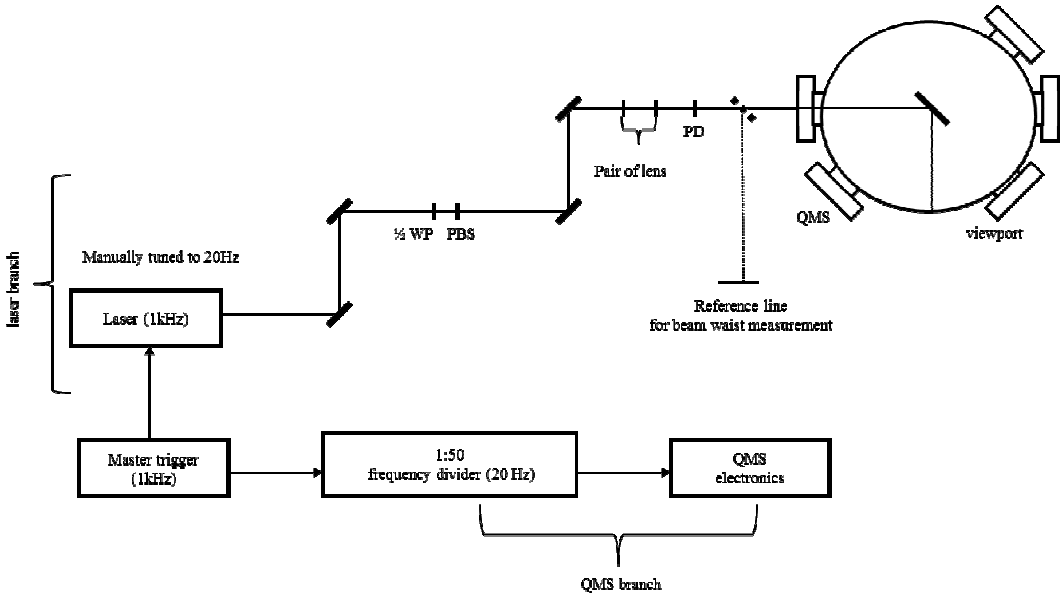

Figure 2.16 Schematic of the experimental set-up for femtosecond laser-induced desorption experiments. ½ WP – half waveplate, PD – photodiode used to adjust the delay between femtosecond and the transistor-transistor logic (TTL) pulse, PB – polarizing beam splitter.

A schematic of the electronics for synchronization of the laser pulses with the QMS is shown in Figure 2.16, and in more detail in the timing diagram, Figure 2.17.

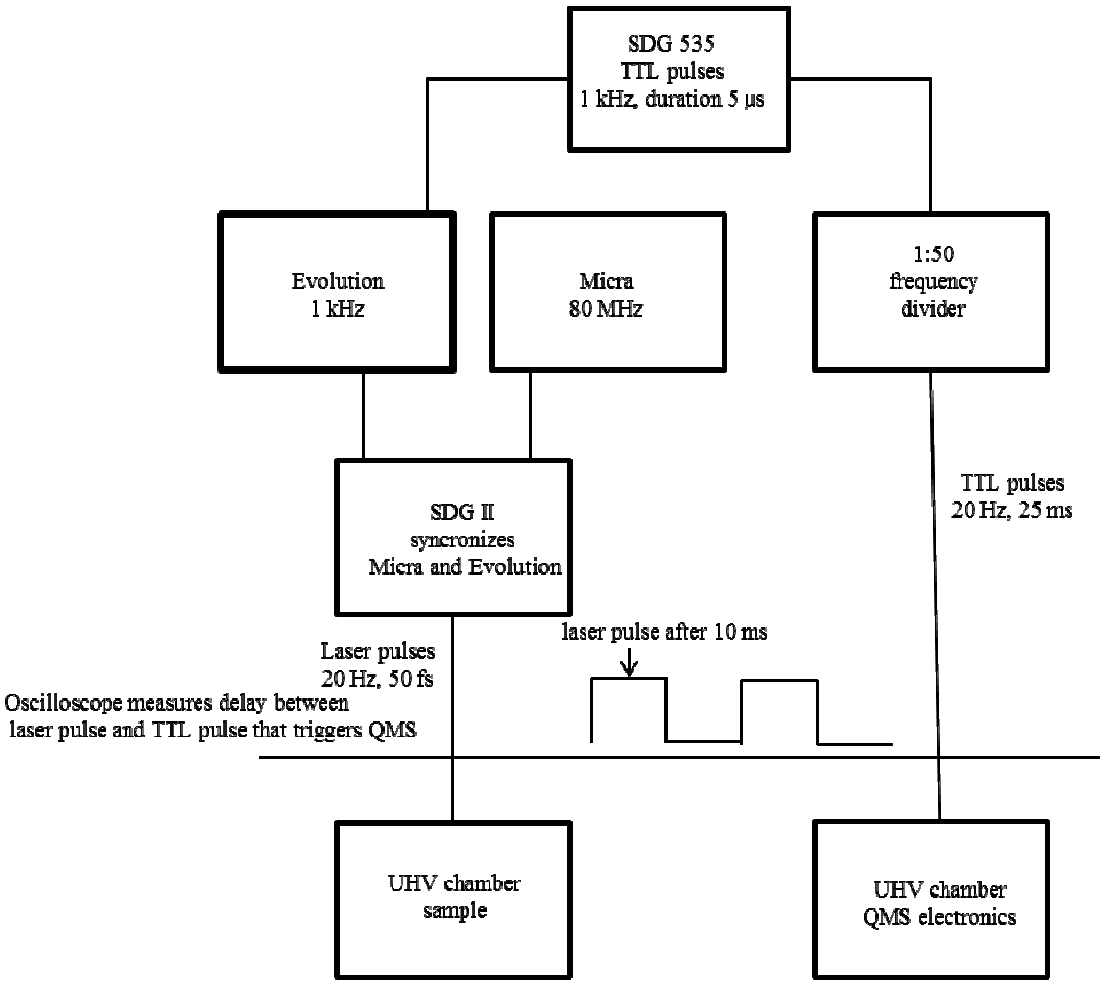

Figure 2.17 Timing diagram showing how the synchronization of the laser pulses with QMS is performed.

The SDG 535 produced a 1 kHz TTL pulse train which acted as a master trigger. This master trigger is used to externally trigger the Evolution laser (laser branch) and to trigger the QMS (QMS branch). The repetition rate of the master trigger is reduced to 20 Hz in both branches. In the QMS branch, this is achieved using a 1:50 frequency divider. In the laser branch, a second delay generator (SDG II) enables fine tuning of the repetition rate of the laser pulses coming out of the amplifier so that the frequency of the laser pulse is matched to the frequency of the TTL pulse triggering the QMS. The SDG II is a pulse generator that syncronises the Evolution, Micra and Legend. The delay, between the femtosecond pulses (photodiode signal in front of the UHV chamber) and the TTL pulses triggering the QMS, was monitored on an oscilloscope.

This synchronization was necessary so that the QMS can collect the data in the single shot operating mode, so that a desorption yield after a single pulse could be recorded.

As already mentioned, a regeneratively amplified Ti:sapphire laser system generates laser pulses of 55 fs duration, with a central wavelength of 790 nm and a maximum pulse energy of 2.5 mJ at the maximum repetition rate of 1 kHz. The repetition rate of the laser could be manually reduced to 10 Hz. The pulse energy was adjusted with a variable attenuator constructed from a half-waveplate and a polarizing beam splitter, allowing surface science measurements to be made as a function of the absorbed fluence. The fluence can be calculated from the energy per pulse.

The maximum energy per pulse in front of the UHV chamber was measured to be 1.7 mJ. The maximum energy per pulse at the sample was calculated to be 0.5 mJ.

First the measured energy per pulse in front of the UHV chamber needs to be corrected for transmission of 800 nm light through the fused silica window. Then, using the Fresnel formula [9] for reflectance of the incident polarized light from a metal surface (Equation 1.6b, Chapter 1) and assuming that only absorption and reflection occur in the experimental wavelength region, the energy per pulse at the sample can be obtained. The absorbed fluence is then calculated from the knowledge of the laser beam profile. A pair of lenses in front of the UHV chamber was employed to reduce the beam size at the sample to an ellipse with a FWHM ~ 0.8 mm in the *x*-direction and 1.7 mm in the *y*-direction (average values of FWHM in *x* and *y* direction for all sample mounts used). The fluence could then be adjusted from 0 to 35 mJ cm^{-2}. The beam profile was measured in the reference beam path at the same distance from the laser as the sample, as shown in Figure 2.17. It is important to mention that even though the femtosecond laser light was not reflected out of the chamber, this did not cause any technical problems in performing fs-LID experiments.

The photodesorption experiments were performed in the following way: first a background QMS signal of CO/NO was collected for 1 minute, the black shielding in front of the UHV chamber was then removed so that the QMS signal arising from 400 individual laser pulses (t ~ 20 s) could be collected. After approximately 200 laser pulses, the surface is found to be depleted. The sample was then translated to a new point, and a new spot was irradiated in a single experiment. Up to about 5 points on the sample could be irradiated. The maximum desorption yield occurs with the first shot, falling biexponentially with additional shots. The first shot yield as a function of the

initial coverage is derived by fitting a biexponential decay through the yield as a function of laser shot number, as shown in Figure 2.18.

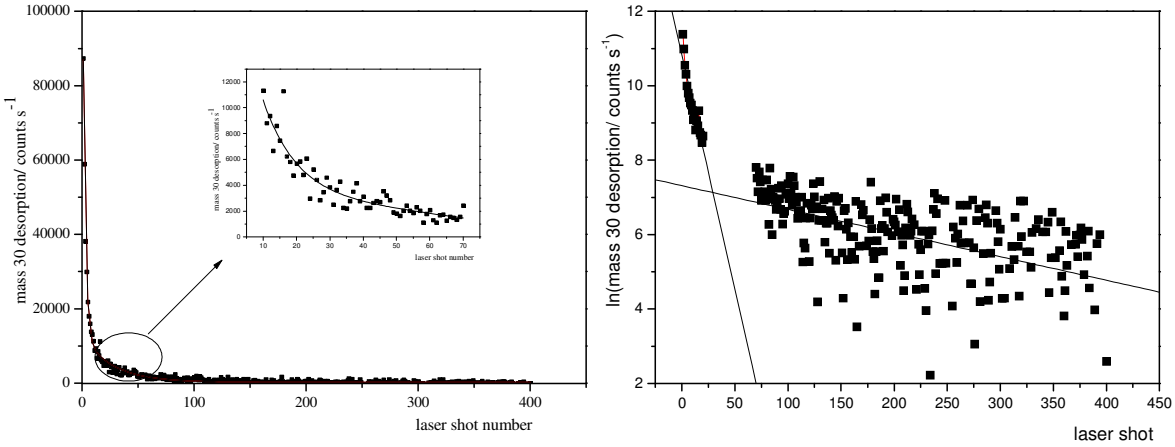

Figure 2.18 a Example of the depletion curve from one experiment. The data points are assigned by ■, and the biexponential curve by —. The first shot yield is calculated from the biexponential curve. **b** Natural logarithm of the mass 30 QMS signal in Figure 2.18 a as a function of the laser shot number. The straight lines show regions where the biexponential decay can be replaced by an exponential decay.

The biexponential dependence of the QMS signal on the surface coverage is called the depletion curve. The origin of the biexponential dependence can be explained by taking the natural logarithm of the QMS signal, as shown in Figure 2.18b. The depletion of the coverage by the femtosecond laser is represented by a fast component in the biexponential decay for approximately 20 laser shots. The exponential decay then becomes influenced by the diffusion of the adsorbate molecules into the illuminated surface area. Surface diffusion into the depleted laser area is the dominant process after approximately 100 laser shots, and the slow component is enough to describe the depletion of the surface coverage.

Using the variable attenuator, the energy of the pulse can be varied, and consequently the fluence, so for a particular fluence a set of depletion curves is obtained. The fluence dependence of the photodesorption yield is obtained as follows: all of the first shot yields obtained from the depletion curves are plotted as a function of laser fluence; the empirical function $Y_{FS} \sim F^n$ or $Y_{FS} \sim (F\text{-}F_0)^n$ (where F_0 is the fluence threshold) is then fitted through the data.

The Pd(111) crystal is cleaned between each set of five experiments, either by performing a TPD cycle (CO experiments), or by performing the proper cleaning

procedure (NO and NO/CO mixtures). TPD cleaning proved to be efficient for CO but not for NO or NO/CO experiments because the oxygen from the NO dissociation desorbs at high temperatures (> 900 K) so oxygen could not be removed in the thermal desorption of NO.

2.10 Summary

This chapter has described the experimental components and diagnostic methods for photodesorption experiments and the realization of the main surface science experiments described in this thesis. The results and discussion of the photodesorption experiments are described in detail in chapters 4 and 5.

2.11 References

1. A. Nunn, *Experimental and theoretical investigations of the photochemistry of styrene and the creation and characterization of shaped ultraviolet femtosecond pulses*. (PhD thesis, University College London, 2010).
2. R. Trebino, *Frequency-Resolved Optical Gating: The measurement of Ultrashort Laser pulses*. (Kluwer Academic Publishers, 2002).
3. Newport Corporation. January 2011. The effect of Dispersion on Ultrashort Pulses. [online]. Available from: http://www.newport.com/The-Effect-of-DispersionnUltrashortPulses/602091/1033/catalog.aspx.
4. E. M. McCash, *Surface Chemistry* (New York, Oxford University Press, 2001).
5. R. J. Mukerji, *Studies of adsorption and reaction on the stepped Pt(2111) surface.* (PhD thesis, University College London, 2003).
6. Dr. R. M. Nix. June 2003. An introduction to surface chemistry. [online]. Available from: http://www.chem.qmul.ac.uk/surfaces/scc/.
7. Leiden University. March 2008. [online]. Available from: https://openacesss.leidenuniv.nl/dspace/bitstream/1887/4322/11/02.pdf.
8. P. A. Redhead, *Vacuum* **12**, 203 (1962).
9. D. E. Gray, *American Institute of Physics Handbook - 3rd ed.* (McGraw-Hill, New York, 1972).

CHAPTER 3

DEVELOPMENT OF AN EXPERIMENTAL SET-UP FOR HHG

3.1 Introduction

This chapter focuses on the design of a femtosecond extreme ultraviolet (XUV) laser source for photoelectron spectroscopy (both in the gas phase and at surfaces). It describes the theory behind high harmonic generation (HHG), how the design parameters of the capillary waveguide XUV source were determined and it describes the generation of the 9th and 11th harmonics of 800 nm femtosecond laser pulses in a glass capillary waveguide.

3.2 Overview

The experimental research described in this chapter belongs to the field of non-linear optics. This field covers a broad range of optical effects that can convert light of a given frequency into light of different frequencies. An illustrative example is second harmonic generation (SHG), which was the first experimentally induced non-linear optical effect observed. It was demonstrated and reported by Franken in 1961. [1] He irradiated crystalline quartz with light from a ruby laser at a wavelength of 694 nm, converting a fraction of the energy of the incident red laser beam into ultraviolet light with a wavelength of 347 nm. This ultraviolet light has a frequency that is twice that of the incident beam, and hence is referred to as the second harmonic of the incident beam.

Non-linear effects are associated with the non-linear dependence of the electric polarization, P on the electric field, E. When the magnitude of the electric field is small, the magnitude of the electric polarization is linearly proportional to the electric field, E:

$$P = \varepsilon_0 \chi E , \tag{3.1}$$

where χ is the electric susceptibility tensor, and ε_0 is the permittivity of free space [2]. In the case of a weak electric field, even second harmonic generation is not possible.

However, when the magnitude of the electric field is large, the induced polarization has a non-linear dependence on the electric field. The induced polarization can then be expressed as a power series of the electric field,

$$P = \sum_n \varepsilon_0 \chi^{(n)} E^n . \qquad (3.2)$$

The first non-linear term, $\chi^{(2)}$ in Equation 3.2 is responsible for SHG [2].

There are also non-linear optical processes that yield considerably higher frequency multiples. The produced beams are then called higher order harmonics, and the order of the harmonic refers to the factoral increase in frequency with respect to the incident beam. For instance, an infrared light beam at a wavelength of 800 nm can be partly converted into third harmonic light, at a frequency three times that of the incident light. A frequency increase implies a wavelength decrease by the same factor. Thus, this light conversion process, known as third harmonic generation, yields new light with a wavelength that is reduced by a factor of three with respect to the incident beam [3]. The third harmonic light has a wavelength of 267 nm and falls in the ultraviolet part of the spectrum, as illustrated at the bottom of Figure 3.1. Third and other odd harmonics can only be produced in centrosymmetric media (gases), while second and other even harmonics are produced only in non-centrosymmetric media [2].

Harmonics of much higher order can be produced through the process of high harmonic generation (HHG). HHG enables the conversion of infrared light into light with wavelengths so short that it falls within the XUV (30-100 nm), or soft X-ray regime (0.2-30 nm). It is clearly seen from Figure 3.1, that the 9th and 11th harmonics of 800 nm radiation belong to XUV part of the electromagnetic spectrum. The 27th harmonic is between the soft x-ray region and the XUV region.

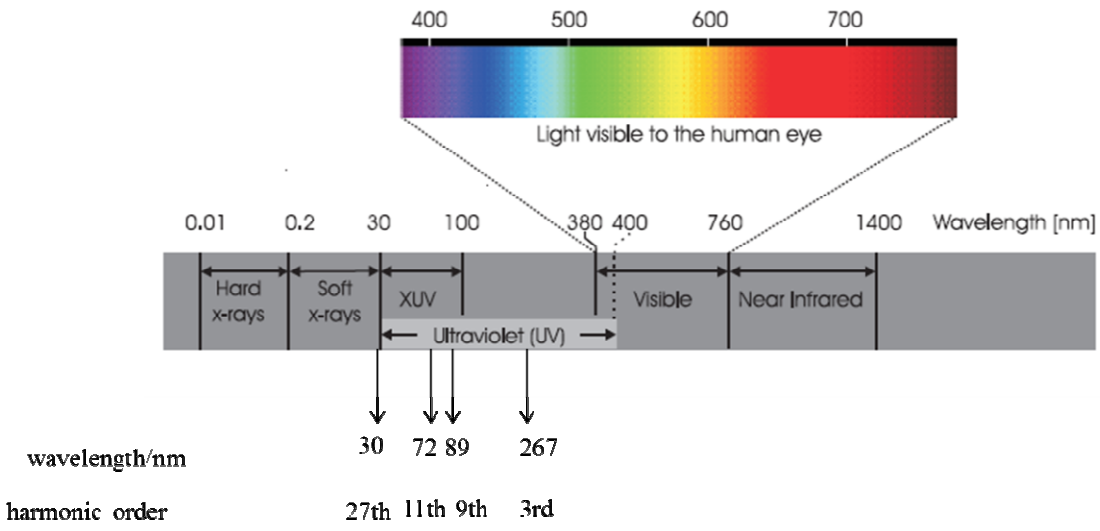

Figure 3.1 A part of the electromagnetic spectrum from x-rays to near infrared. The enlarged section on the top shows colours in the spectral region visible to human eye. At the bottom of figure, the spectral locations of several harmonics of 800 nm light are shown. Figure taken from reference 3.

HHG is enabled only under extreme conditions when intense, linearly polarised, ultrafast laser pulses are focused into a non-linear gas. There are two experimental set-ups frequently used to generate HHG: pulsed nozzles and capillary waveguides. These set-ups will be described in more detail in Section 3.3. HHG has many applications such as in attosecond science, lithography, plasma analysis [3], surface microscopy and holography and finally in photoelectron spectroscopy. [4] In this thesis, the interest is in photoelectron spectroscopy, specifically, for this project, surface photoelectron spectroscopy. Since the project involved designing and building the harmonic source from scratch, the first step was to produce and detect any high harmonics of the fundamental 800 nm radiation. Gas phase photochemistry experiments generally require a coherent source of XUV radiation of around 10 eV, and so the 9th harmonic of 800 nm is a good starting point. Although not within the scope of this thesis, the next step would be to generate the 27th harmonic for surface science experiments.

Time-resolved photoelectron spectroscopy (TRPES) is a pump-probe technique that can be exploited to follow molecular dynamics in real time. Generally, a pump-probe experimental setup employs a “pump” pulse and a “probe” pulse. The pump pulse initiates the physical phenomenon under study. Then, the probe pulse is sent into the system with a time delay to “probe” the system status at that moment. This process is

similar to taking stroboscopic pictures of the phenomenon at various times after it starts. The pump and the probe pulses should both be faster than the changes of the system otherwise, the "snap-shots" will be blurred. So, pulses with sub-picosecond duration are required to study photoinduced surface dynamics. Infrared pulses are often employed to initiate surface reactions and XUV pulses are required for TRPES measurements. Infrared pulses are commercially available with less than 50 fs duration. Since the complete high harmonic generation process happens within one optical cycle of the infrared ultrafast pulse, the generated high harmonic pulses are typically shorter than the driving infrared pulse.

Laser driven reactions can have different channels if compared to thermally driven reactions. The main reason is that ultrashort laser pulses create hot substrate electrons that can drive the reaction with a different mechanism to phonon driven thermal reactions. However, direct experimental confirmation of these highly excited surface electrons was not available until the work of J. Boker *et al.* in 1992. [5–6] In their experiments, a gold film was heated with 1.84 eV photons to generate hot surface electrons. A second laser pulse was frequency-doubled to 337 nm, and subsequently frequency-mixed again with the 674 nm light to generate 5.52 eV photons. The work function of the gold film is only 5.1 eV, and hence the 5.52 eV photons will have high enough photon energy to photoeject electrons close to the Fermi-edge. For long time delays, the electron energy distribution function can be fitted nicely by the Fermi-Dirac function for a particular electronic temperature. However, for time delays within the first picosecond, significant discrepancies happen at the energy region above the Fermi-edge where "hot" or nonthermal electrons exist. Because of the rapid excitation process, these hot electrons cannot be described by a Fermi-Dirac energy distribution, which is only valid when the physical system is in thermal equilibrium.

For the study of valence levels of an adsorbate-substrate system the energy of the harmonic source needs to be at least 20 eV, analogous to ultraviolet photoemission spectroscopy (UPS). In general, a large number of valence levels are contained within a rather narrow range (typically ~10 eV), and a work function is typically not higher than 10 eV.

In this section, a brief overview of TRPES in surface science will be given. The first TRPES experiment (infrared (IR) pump and XUV probe) on an adsorbate covered surface was for O_2/Pt(111) and was carried out by Lei *et al.* [7–8] At liquid nitrogen

temperatures, oxygen is adsorbed molecularly onto a Pt(111) surface, and it occupies bridge sites. This configuration is known as superoxo oxygen (O_2^-). The oxygen becomes negatively charged because one electron is transferred between the platinum d-band and the $1\pi_g^*$ molecular orbital of oxygen. If the surface temperature is raised to 145 K, a large amount of oxygen desorbs and the rest of the oxygen on the surface starts to occupy the three-fold hollow sites to lower the adsorption energy. This configuration is called peroxo oxygen (O_2^{2-}). In this case, two electrons are transferred between the platinum d-band and the $1\pi_g^*$ molecular orbital of oxygen. When the surface is heated above 145 K, the oxygen molecules gain enough energy to dissociate into two oxygen atoms, and they again reside in three-fold hollow sites on the surface. All three types of oxygen were observed in the TPD experiments carried out by this group.

Puglia *et al.* [9] reported a peak at 6 eV above the Fermi level for the peroxo and pure oxygen configurations in detailed UPS experiments of O_2/Pt(111). This peak appears in the energy range of the oxygen valence states that are due to the interaction of the oxygen with the platinum *d* bands, [10–12] so the peak is very sensitive to the chemical bond character of the chemisorbed oxygen. This peak has been seen by others [13] using synchrotron radiation sources, and was assigned to the $1\pi_g^*$ molecular orbital of oxygen. The static UPS studies carried out by Lei *et al.* [8] are in qualitative agreement with the work of Puglia *et al.* [9], and they show a change in the peak shape (at 6 eV above the Fermi level) between the peroxo and superoxo oxygen states, but not between the peroxo and pure oxygen adsorbed on Pt(111). The spectra of peroxo oxygen and pure oxygen are similar because oxygen resides in a similar geometry (3-fold hollow site). The geometry of superoxo oxygen is different (bridge site), so it is not surprising that the peak shape changes due to the change in bond character of chemisorbed oxygen.

The time-resolved photoelectron spectroscopy experiment of O_2/Pt(111) at liquid nitrogen temperature (superoxo oxygen configuration) shows a transient peak at 6 eV that starts to appear for 250 fs pump probe delays and is also visible for 500 fs delays. This peak is similar to the peak in the static photoemission spectrum of peroxo oxygen and the static spectrum of atomic oxygen. It is definitely not due to a permanent change in the sample because the photoelectron spectrum at time zero recorded immediately after the 500 fs delay does not contain a peak at 6 eV binding energy. Therefore, two possibilities for this transient peak are either the excitation of superoxo oxygen into two

dissociated atomic oxygen atoms, or into peroxo oxygen. These two processes are in fact similar, since peroxo oxygen can be considered as a precursor state for dissociation.

Very recently, Dachraoui *et al.* [14] have reported a TRPES (ultraviolet (UV) pump pulse and XUV probe pulse) investigation of self-assembled monolayers of iodophenylphenol on Si(100). Complex photoreaction dynamics were revealed, proceeding *via* several intermediate states, finally re-establishing the initial state. These examples show that TRPES has great potential for unravelling dynamical processes in surface science, however, this technique is still in its infancy.

3.3 Semiclassical modelling of HHG

The theory behind HHG is based on the numerical solution of the three dimensional Schrödinger equation for a one electron atom in a strong electromagnetic field. In this chapter, the "semiclassical" model developed in [15–16] will be described. This model helps to understand the mechanism of the effect, but it is not very suitable for quantitative investigations. It is related to the work of Burnett, Corkum and Brunel [17–18] who investigated the energy distributions of electrons formed by above threshold ionization. From their work, a model for high harmonic generation was developed [15–16]. HHG is a periodic process (due to the oscillating electric field that drives it), so can be described by the following expression:

$$A + n\hbar\omega \rightarrow A + \hbar n\omega, \tag{3.3}$$

where A denotes the atom, $n\hbar\omega$ denotes n photons of energy $\hbar\omega$, and $\hbar n\omega$ denotes the energy of the photon of frequency $n\omega$.

The elementary process consists of three stages, represented in Figure 3.2.

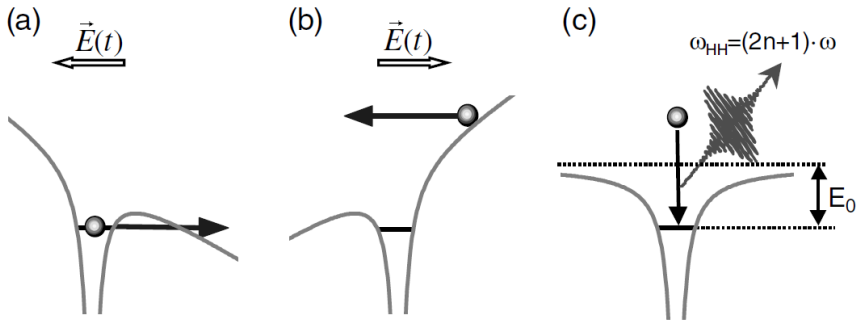

Figure 3.2 Three steps in the production of high harmonics. [19] **(a)** An electron tunnels through the Coulomb barrier and accelerates in the electric field. **(b)** The electron returns to the ion core after reversal of the electric field. **(c)** Odd frequency photons are emitted after the electron returns to the initial bound state.

It is assumed that directly after ionization, at the position where the laser potential plus the Coulomb potential equals the ionization potential, the electron velocity is zero. From the equations of motion for the electron in the laser field, the kinetic energy of the recombining electron can be calculated (see Appendix B). The final expression for the kinetic energy of the recombining electron is given by Equation 3.4:

$$E_k = 2U_p \left(\frac{2 - 2\cos\omega\tau - \omega\tau\sin\omega\tau}{1 - \cos\omega\tau - \omega\tau\sin\omega\tau + \frac{1}{2}\omega^2\tau^2} \right), \tag{3.4}$$

where U_p is the ponderomotive potential, ω is the laser frequency and τ is the difference between the recombination and ionization times. U_p is given by the following expression:

$$U_p = \frac{e_0^2 I}{2m_e\varepsilon_0 c\omega^2} = 9.34\times10^{-20}(\lambda/\mathrm{nm})^2 I/(\mathrm{Wcm}^{-2})\mathrm{eV}, \tag{3.5}$$

where e_0 is the electron charge, m_e is the electron mass, ε_0 is the permittivity of free space, c is the speed of light in a vacuum, ω is the angular frequency, λ is the wavelength of the electromagnetic radiation and I is the laser intensity. Figure 3.3 shows the kinetic energy of the electron in units of the ponderomotive potential (U_p), as a function of $\omega\tau$.

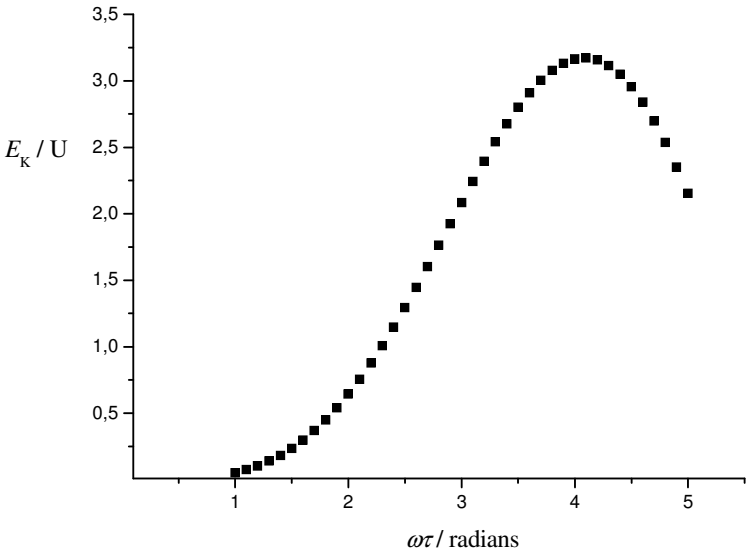

Figure 3.3 The dependence of the energy of the recombining electron on $\omega\tau$ (ω is the laser angular frequency and τ the difference between recombination and ionization time).

If the electron recombines with the parent ion in the ground state and emits a photon, conservation of energy dictates that the maximum energy of the emitted photon cannot exceed $E = E_I + 3.17U_p$, where E_I is the ionization energy of the non-linear medium. This determines the maximum photon energy that can be emitted in a HHG process, and it is often called the cut off energy of the high order harmonic plateau. In proposed experimental set-up, two noble gases will be used for HHG: Xe (9th and 11th harmonics) and Ar (27th harmonic). The main reason for using these gases is that the intensity of the lower harmonics will be higher in Xe than Ar. The harmonics with maximum intensity are shifted towards lower energy for Xe because of its lower cut-off energy. As a result of its spectral structure (only odd harmonics are emitted), the time structure of the HHG consists of bursts of harmonics every half cycle of the laser field and the energy of a photon emitted as a result of recombination is equal to the sum of the binding energy and the kinetic energy acquired by the electron.

For the generation of high harmonics, different experimental schemes are used. [19] In a typical high harmonic generation setup, a pulsed gas nozzle creates a well-defined high density region of non-linear gas inside a vacuum chamber. The gas nozzle pulses synchronously with the incoming focused laser pulses. The reason to use a pulsed valve to generate harmonic light is to avoid re-absorption of the harmonics by the non-linear

gas. However, with this design it is difficult to achieve high fluxes of the harmonics since harmonic photons are generated in a very limited region with varying pressure. Experiments in this thesis will be performed using a hollow capillary waveguide scheme. The phase matching conditions for gas filled glass capillaries, together with the simulations for phase matching pressures for the 9th and 11th harmonics in Xe, and the 27th harmonic in Ar, are explained in detail in the next section.

3.4 Simulations of HHG

The equation for the electric field of the *q*th harmonic, in the presence of absorption can be written as:

$$\frac{dE}{dz} \approx -\alpha E + iN_a \chi_{eff}^{(q)} E_0^s \exp(-i\Delta k z), \tag{3.6}$$

where α is the field absorption coefficient of the harmonic, s is the effective order of the nonlinear process, E_0 is the driving electric field, χ is the nonlinear susceptibility tensor of order $q + 1$, N_a is the atomic number density and Δk is the phase mismatch between the driving laser light and the generated harmonic. [20]

Assuming a constant axial atomic number density profile, and performing the integration in Equation 3.3, the following relation for the intensity of the *q*th harmonic is obtained:

$$\left|E\right|^2 \approx N_a^2 \left|\chi_{eff}^{(q)} E_0^s\right|^2 \left(\frac{1 + e^{-2\alpha L} - 2e^{-\alpha L} \cdot \cos \Delta k L}{\alpha^2 + \Delta k^2}\right), \tag{3.7}$$

where L is the length of the nonlinear medium. The signal strength is determined by the shorter of the coherence length, $l_c = \frac{\pi}{\Delta k}$, and absorption depth, $l_a = \frac{1}{2\alpha}$. Now it has to be considered how the coherence length can be maximised. If harmonic generation occurs in a waveguide of radius a, filled with a medium of refractive index, n, the propagation constant for the fundamental travelling in the lowest mode $(EH_{11})^{**}$ is: [21]

** EH_{nm} are electric hybrid modes of the guided laser beam. Index numbers n and m are related to the propagation profile.

$$k_f^2 = n^2 k_0^2 - \left(\frac{u_{11}}{a}\right)^2, \tag{3.8}$$

where k_0 is the vacuum wavenumber, and u_{11} is the first zero of the Bessel function J_0. [22] If Equation 3.8 is rearranged, one can easily obtain the following expression,

$$k_f^2 = n^2 k_0^2 \left(1 - \frac{1}{n^2 k_0^2}\left(\frac{u_{11}}{a}\right)^2\right). \tag{3.9}$$

By taking the square root of Equation 3.9, the wavenumber for the fundamental is,

$$k_f = n k_0 \left(1 - \frac{1}{n^2 k_0^2}\left(\frac{u_{11}}{a}\right)^2\right)^{1/2}. \tag{3.10}$$

If Equation 3.10 is written as a power series, where only the first two terms are considered, the approximate expression for the fundamental wavenumber is given by Equation 3.11:

$$k_f \approx n k_0 - \frac{1}{2}\frac{u_{11}^2}{k_0 a^2}. \tag{3.11}$$

For a partially ionized gas, the expression for the index of refraction is: [23]

$$n = 1 + \frac{P(1-\eta)\delta(\lambda)}{P_{\text{atm}}} - \frac{P N_{\text{a, atm}} \eta r_e \lambda}{P_{\text{atm}}} + \frac{(1-\eta) P n_2 I}{P_{\text{atm}}} \tag{3.12}$$

Here P is the pressure in atmospheres, P_{atm} is the pressure of 1 atmosphere, $N_{\text{a, atm}}$ is the atomic number density at 1 atmosphere, λ is the fundamental wavelength, r_e is the classical electron radius, n_2 is the nonlinear refractive index at the pressure of 1 atmosphere, $\delta(\lambda)$ is the refractive index for the gas at 1 atmosphere, η is the ionization fraction of the gas and I is the pulse intensity. The first term of the equation corresponds to the propagation of light in free space, the second term to propagation of light in the gas, the third term to propagation through the plasma, and the last term is due to the optical Kerr effect. [24] Finally, the expression for the phase mismatch is (without a nonlinear index contribution):

$$\Delta k = k_q - q k_f, \tag{3.13}$$

which can be rewritten as

$$\Delta k \approx q\frac{u_{11}^2\lambda_0}{4\pi a^2} + \frac{\eta P N_{\text{atm}}}{P_{\text{atm}}} r_{\text{e}}(q\lambda_0 - \lambda_q) - \frac{2\pi P}{P_{\text{atm}}\lambda_q}(1-\eta)(\delta(\lambda_0) - \delta(\lambda_q)) \qquad (3.14)$$

In the case of high harmonic generation, there are two very widely spaced wavelength regimes in which the refractive index must be determined: the near infrared (800 nm radiation), and the XUV regime (the 9th, 11th and 27th harmonics of 800 nm radiation). These two regions must be treated separately. For the refractive indices of noble gases in the infrared region, the model of Dalgarno and Kingston is used: [25]

$$n^2 = 1 + A\left(1 + \frac{B}{\lambda^2} + \frac{C}{\lambda^4} + \frac{D}{\lambda^6} + \frac{E}{\lambda^8} + \frac{F}{\lambda^{10}}\right). \qquad (3.12)$$

where A, B, C, D, E and F are constants characteristic for each of the gases, and λ is the wavelength in angstroms. In the XUV region, the real part of the refractive index at 1 atmosphere is calculated using atomic scattering factors from Chantler *et al.*:[26]

$$n = 1 - \frac{r_e}{2\pi}\lambda^2 N_{atm} f_1 \qquad (3.13)$$

where r_e is the classic electron radius, λ is the wavelength of the particular harmonic, N_{atm} is the atomic number density at 1 atmosphere and f_1 is the real part of the atomic scattering factor. The field absorption coeficients [27] are calculated using photoionization cross sections from references [28–29].

Numerical simulations based on phase matching conditions were performed in Excel. First of all, to test the proposed model, simulations were carried out reproducing the conditions in the work of A. Rundquist *et al.*. [30] The output of the 29th harmonic in argon for four different conditions is calculated, and is described in Figure 3.4 below. Figure 3.5 shows the output of the 29th harmonic in argon calculated by Rundquist *et al.* [30]

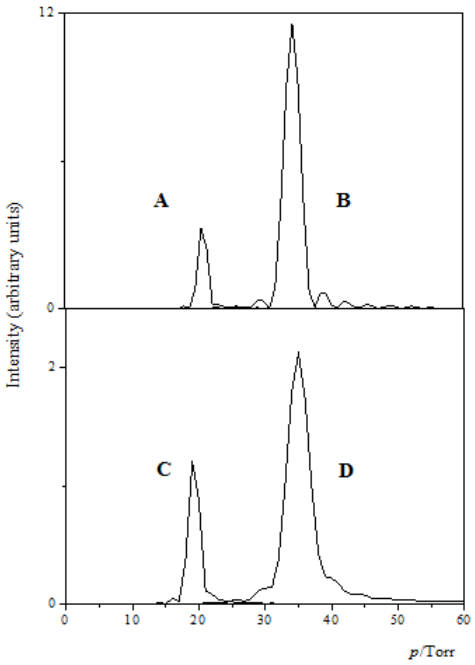

Figure 3.4 (**A**) Calculated output of the 29th harmonic (without absorption and ionization), (**B**) in the presence of constant 2% ionization, (**C**) in the presence of absorption, and (**D**) net output in the presence of absorption and constant 2% ionization; l = 3 cm, a = 75 μm, η = 2%.

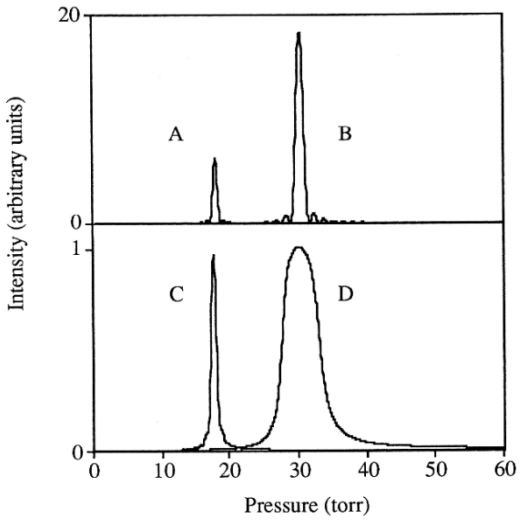

Figure 3.5 (**A**) Calculated output of the 29th harmonic, (**B**) in the presence of constant 2% ionization, (**C**) in the presence of absorption, and (**D**) net output in the presence of absorption and varying levels of ionization around 2%. [30]

If the results of the simulations shown in Figure 3.4 are compared with the results of Rundquist *et al.* in Figure 3.5, [30] it can be seen that they are in good qualitative agreement. Because Rundquist *et al.* [30] did not mention the source of their data, it is possible that this is the cause of the slight deviations in relative intensities observed. The maximum in the presence of 2% ionization in reference [30] occurs at 30 Torr, but according to simulations in this laboratory it occurs at 35 Torr. However, in the same paper it is written that "at pressures of 35 Torr, phase matching is predicted and observed to occur and caused a dramatic increase in harmonic output."

Next, the intensity as a function of pressure was calculated for the 23rd harmonic and the 15th harmonic in Xe, comparing them with the work of Constant, [31] and Durfee. [21] These results are shown in Figure 3.6 and Figure 3.7 and compare very well with the literature calculations.

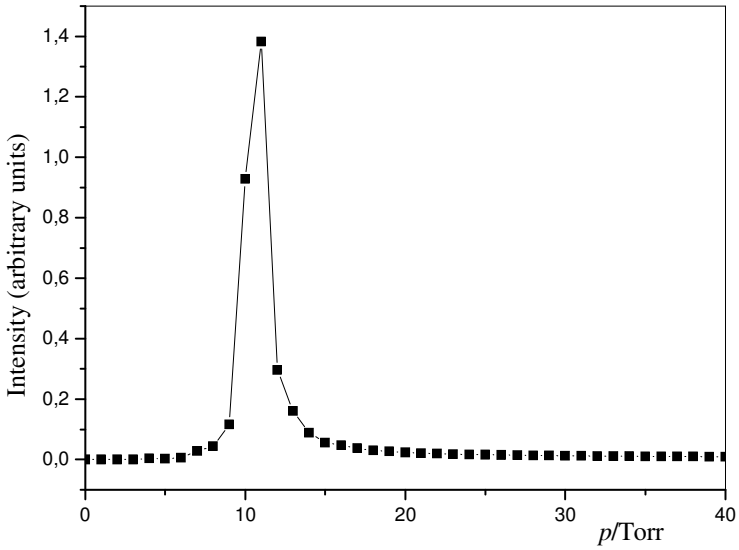

Figure 3.6 The calculated pressure dependence of the 23rd harmonic in Xe. Simulations are based on conditions from the work of Durfee, η = 6% (at the peak of the pulse), l = 3 cm, a = 75 μm. [21]

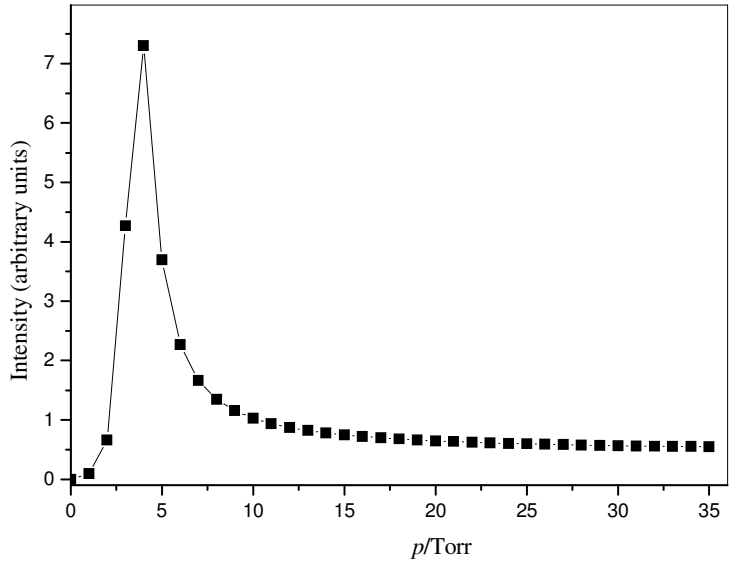

Figure 3.7 The calculated pressure dependence for the 15th harmonic in Xe for negligible ionization. Simulations are based on conditions from the work of Constant, a = 100 μm, l = 4 cm, $\eta \approx 0$. ($I = 5\times10^{-13}$ W cm^{-2}). [31]

After confirming the validity of the model, the radius was optimized for growth of the 9th and 11th harmonics in Xe and the 27th harmonic in Ar. The bore radius of the capillary was varied from 60 μm to 150 μm. Figure 3.8 shows the radius dependence of the growth of each of the harmonics *versus* the pressure of the gas inside the capillary. For experiments in this thesis it was decided to choose capillaries of radii 80 and 100 μm, mostly because the pressure of the gas (Ar or Xe) inside these capillaries is easily achievable, and intensities for all harmonics are within the optimal range, as shown in Figure 3.8. Another important reason is that these radii are available commercially.

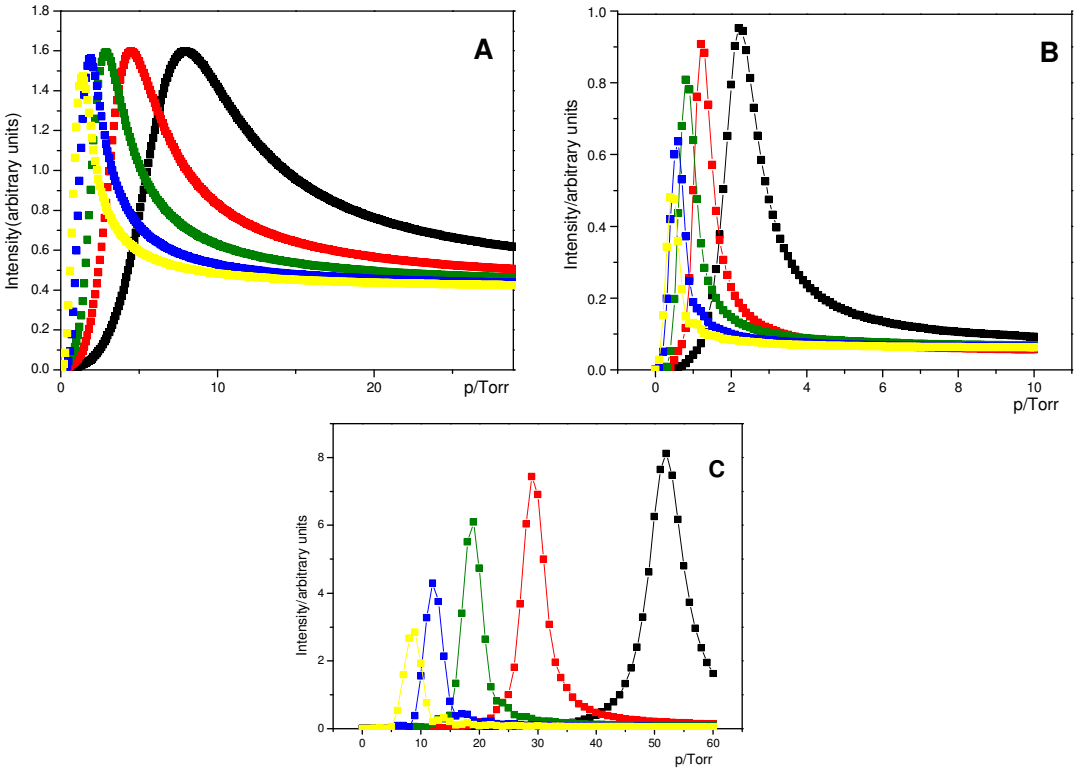

Figure 3.8 A) Radius dependence of the growth of the 11th harmonic in Xe for a capillary of length 3 cm, η = 6% (at the peak of the pulse). **B)** Radius dependence of the growth of the 9th harmonic in Xe for a capillary of length 3 cm, η = 6% (at the peak of the pulse). **C**) Radius dependence of the growth of the 27th harmonic in Ar for a capillary of length 3 cm, η = 2% (at the peak of the pulse). For all plots ■ r = 60 µm, ■ r = 80 µm, ■ r = 100 µm, ■ r = 125 µm, ■ r = 150 µm.

From Figure 3.8 it can be seen that the pressure at which phase matching is predicted for the 11th harmonic in Xe (η = 6%) [21] is for a = 80 µm, p = 4.5 Torr, and for a = 100 µm, p = 2.9 Torr. If ionization is varied from 0 to 6%, the position of the maximum changes only slightly. For the 9th harmonic in Xe, phase matching pressures are: 1.2 Torr for a = 80 µm, and 0.8 Torr for a = 100 µm. For the 27th harmonic, the ionization fraction, η was estimated to be about 2%, [30] and the values for the pressure for a 100 µm, and 80 µm capillary at which phase matching occurs are 19 and 29 Torr, respectively.

3.5 Experimental set-up for HHG

3.5.1 Design of the XUV apparatus

The original idea was to select and detect the 9th harmonic of 800 nm radiation (E = 14 eV), because this is the energy useful for gas photochemistry experiments and an appropriate spectrometer was already available in the lab. The diffraction grating used was optimized for 120 nm radiation (88% diffraction efficiency) with diffraction efficiency of ~4% for the 9th harmonic, 89 nm. The problem was that this diffraction grating (concave holographic grating with aluminum and MgF_2 coating, Princeton instruments) had even lower efficiency for diffraction of harmonics whose order was higher than 9. An indium filter was chosen to get rid of the large background 800 nm light that is scattered in the apparatus. It is highly selective for the 9th harmonic as is shown in Figure 3.9.

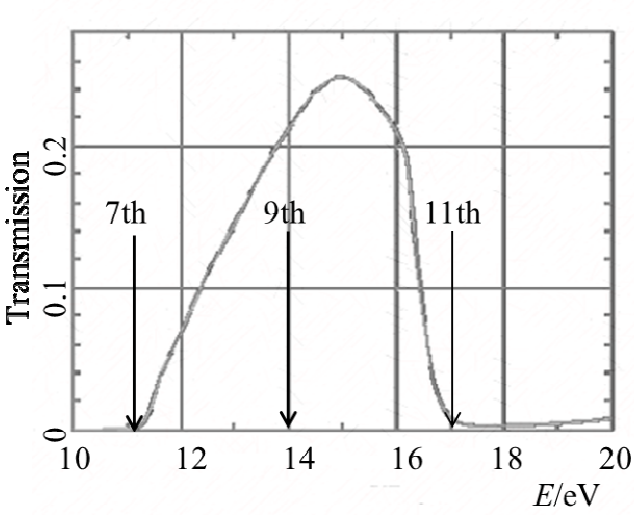

Figure 3.9 Transmission curve for indium filter, thickness 200 nm. 22% of the 9th harmonic of fundamental 800 nm radiation (E = 14 eV) is transmitted. [32]

From Figure 3.9 it can be observed that only the 9th harmonic of 800 nm radiation will be transmitted. The 7th harmonic (E = 10.8 eV) and the 11th harmonic (E = 17 eV) cannot be transmitted at all. The problem is that thin indium filters are very fragile, but thin materials are necessary to get acceptable transmission in the XUV region. Transmission is determined by the physics of the chosen material and its thickness.

During the large number of modifications that this set-up required, the filter was moved in and out of the vacuum system a number of times, and at the end, it had a number of tiny little holes that transmitted the unwanted 800 nm radiation. Finally it was decided to opt for the 11th harmonic instead of buying new indium filters. The 11th harmonic is the first harmonic that can be seen using aluminium filters, which are considerably less expensive than indium filters and have shorter delivery times. The transmission curve for the aluminium filter is shown in Figure 3.10.

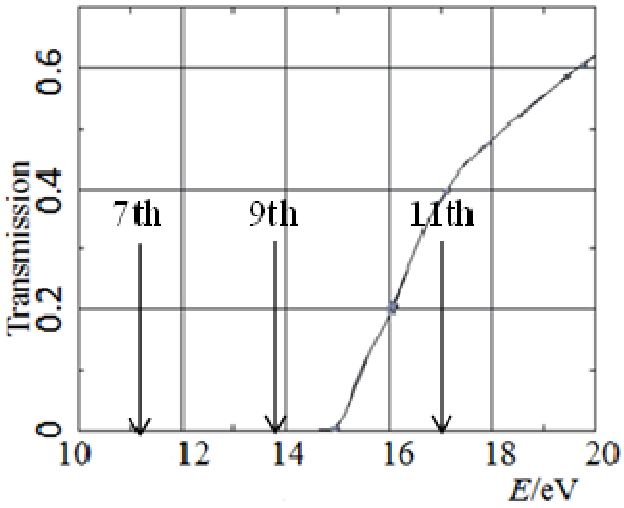

Figure 3.10 Transmission curve for aluminum filter, thickness 200 nm. 40% of the 11th harmonic of fundamental 800 nm radiation (E = 17 eV) is transmitted. [32]

It can be seen that a higher percentage of harmonic radiation will be transmitted in this case (40%), but unfortunately the diffraction grating in the Acton spectrometer is even less efficient for 17 eV (11th harmonic) than for the 9th harmonic.

3.5.1.1 1st design of capillary XUV source

Figure 3.11 shows one of the first set-ups for HHG, and Figure 3.12 shows a schematic of the cross section of the same set-up.

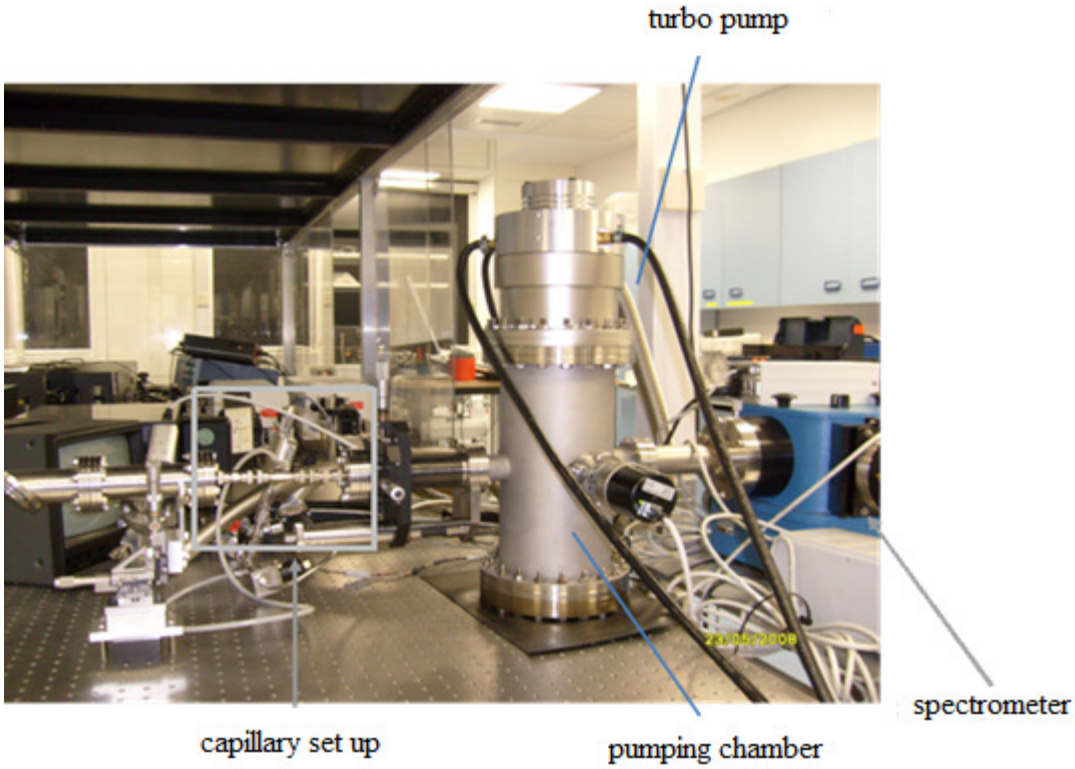

Figure 3.11 Photo of the first set-up for XUV radiation.

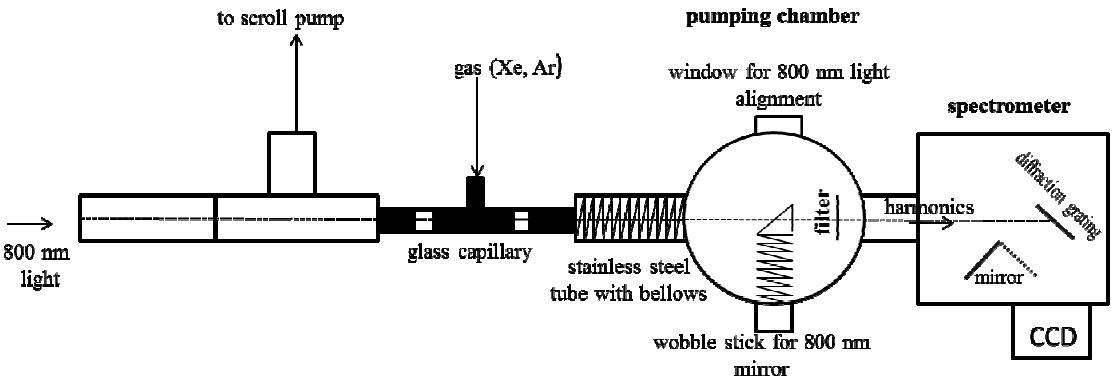

Figure 3.12 Schematic drawing of the first set-up for XUV radiation.

In the first design of the XUV apparatus, the aluminium filter was put in the pumping chamber and it was screwed to the bottom of the chamber. The alignment of 800 nm radiation through the capillary was first performed in air with the CCD camera held at room temperature, and the filter was positioned such that the influence of 800 nm

radiation on the background was minimized. The temperature of the CCD camera can be lowered while the system is under vacuum so that the background counts are lower than at 25 ˚C, but the sensitivity to any stray 800 nm radiation grows. In all designs, the capillary waveguide was movable so that the alignment was easier, but unfortunately this meant that the alignment in vacuum was not the same as in air.

Testing this first XUV set-up revealed two main problems. The background signal due to the scattered 800 nm radiation grew significantly in vacuum compared to air, because any slight difference in alignment caused by evacuating the system can result in multiple reflections from the chamber walls due to the filter position. The other point is that the alignment of the 800 nm radiation could not be checked after the pumping chamber due to the fixed position of the filter. Hence, the alignment of the 800 nm radiation through the capillary was checked in the pumping chamber, through the mirror that reflected the light outside of the silica fused window (nicely seen in the schematic drawing, Figure 3.12). This design was modified in a number of stages that resulted in the optimal configuration described below.

3.5.1.2 Final design of capillary XUV source

In the final design (shown in Figure 3.13 and 3.14), the aluminium filter was positioned in the small T-tube between the pumping chamber and the spectrometer, and it could be moved in and out using a stick with a bellows that enabled stretching and compressing it in vacuum.

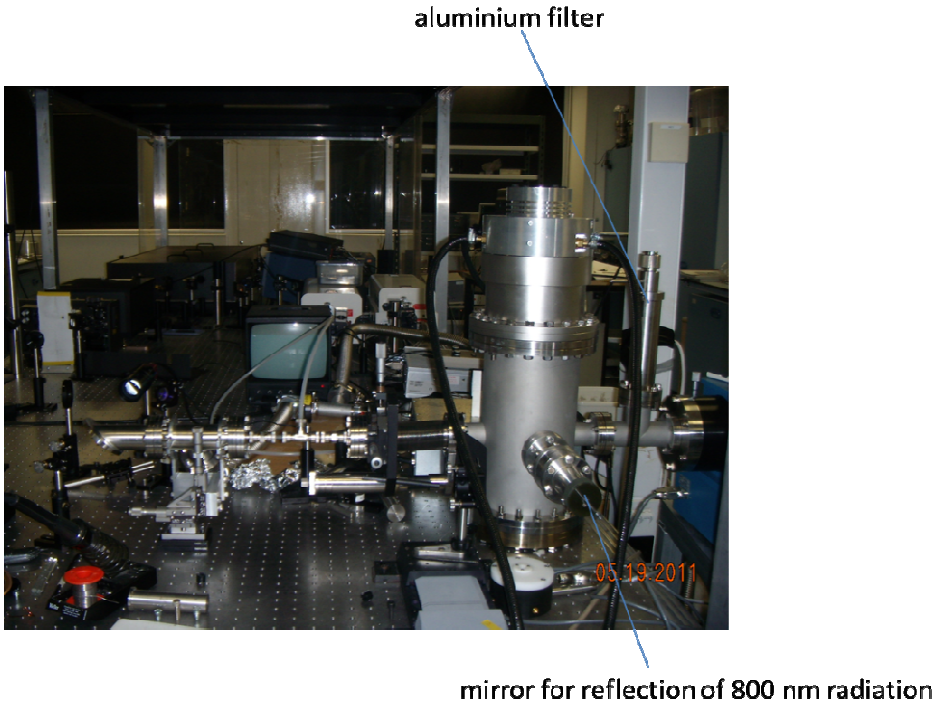

Figure 3.13 Final set-up for XUV generation.

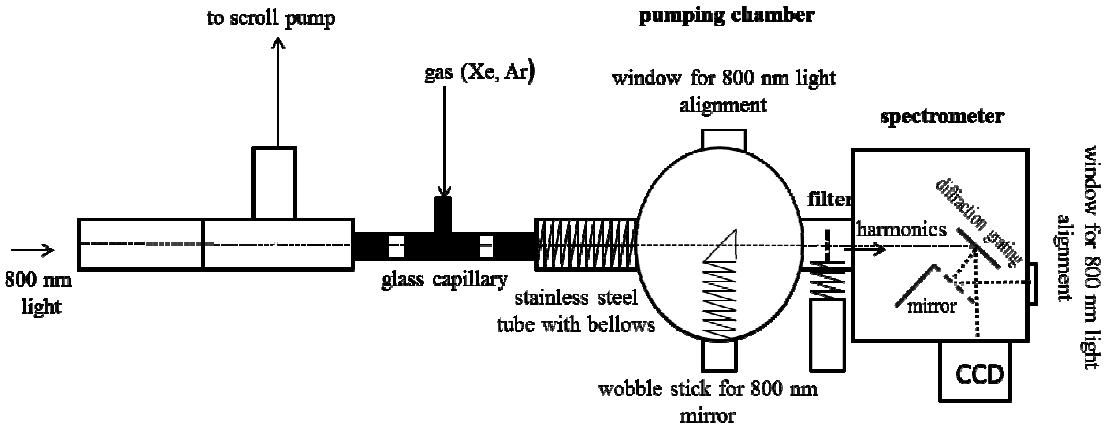

Figure 3.14 Schematic drawing of the final set-up for XUV radiation.

The fused silica mirror for checking the alignment and the conversion efficiency of the 800 nm light remained in the pumping chamber. The additional feature added in the set-up was the small window at the end of the spectrometer that enabled rough checking of the alignment inside of the spectrometer. With this set-up, the 11th harmonic of the 800

nm radiation was finally detected with the charge coupled device (CCD) camera, at pressures of 8, 9 and 10 Torr.

There are also a number of design considerations concerning the glass capillary waveguide, which will be outlined below.

3.5.2 Design of the glass capillary waveguide

In the first design of the capillary, the glass capillary was held inside a stainless steel tube that was divided into three parts. The capillary waveguide was screwed to the walls of the tube so that the central part (l = 3 cm) of the capillary was in the central part of the tube. There were two issues associated with this set-up: 800 nm light could not be detected at the capillary exit and the gas that was introduced in the central tube leaked into the vacuum system, so the pressure in the whole system grew to a few mbars.

The simplest and most inexpensive solution was a three section capillary waveguide formed by using two straight and one T-shaped, compression fitting. Figure 3.15 shows a photograph of the capillary and a schematic of the cross section of this design.

a)

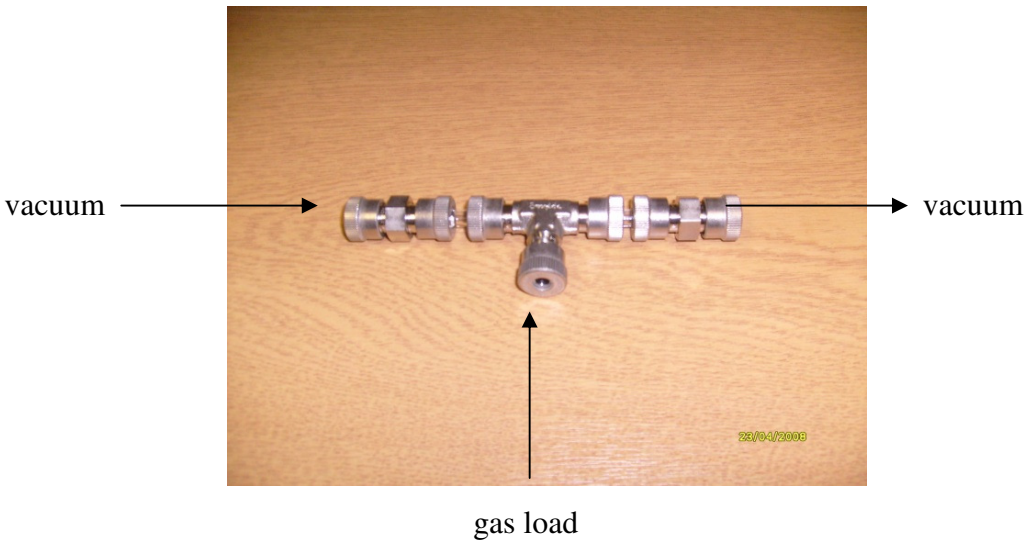

b)

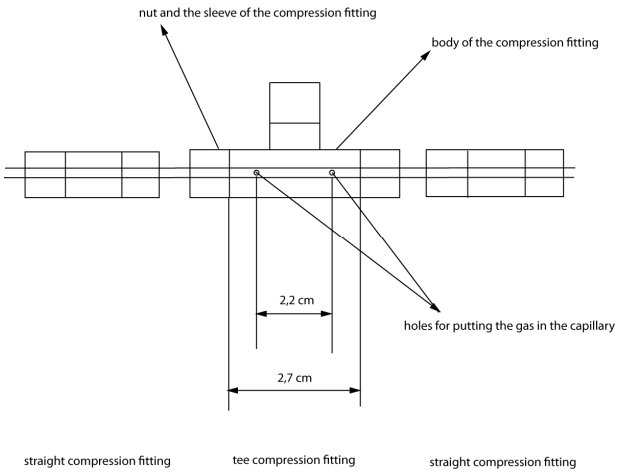

Figure 3.15 a) Three section capillary waveguide set up. b) Cross section of the capillary waveguide.

From Figure 3.15, it can be seen that the length of the central section of the capillary waveguide is limited by the length of the vacuum sealed part in the T-shaped compression fitting. This length was 2.7 cm, therefore the central part of the capillary could not be longer than 2.2 cm so that two drilled holes could fit in the T compression

fitting. Figure 3.16 shows simulations for the dependence of the intensity of the 9th harmonic in Xe with pressure for different lengths of the central capillary.

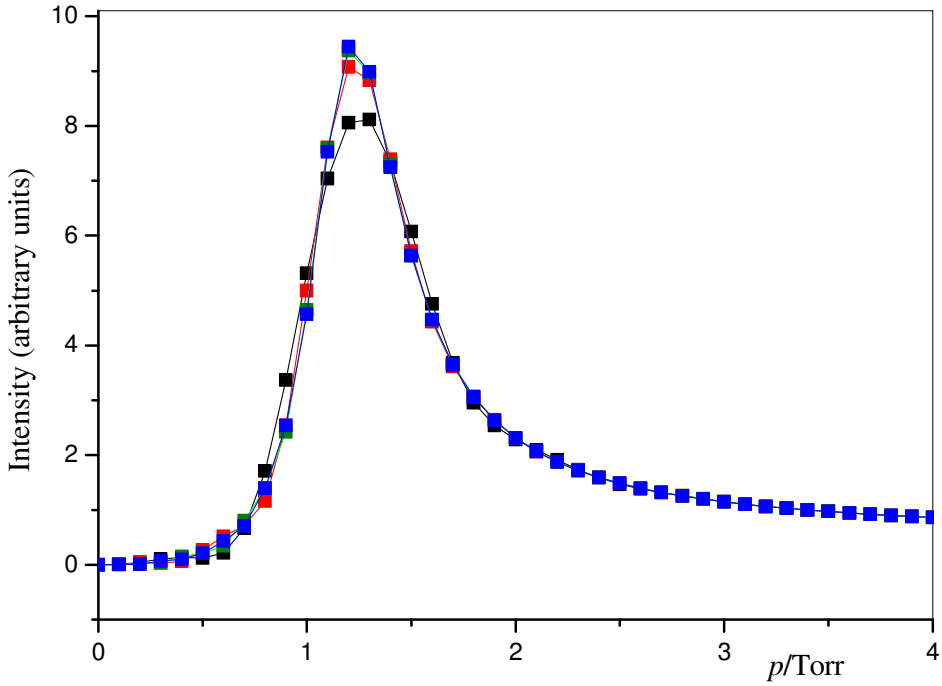

Figure 3.16 Harmonic growth dependence for the 9th harmonic of 800 nm light in Xe on the capillary length, $2 < l/\text{cm} < 5$, $\Delta l = 1$ cm, $a = 80$ µm, $\eta = 6\%$. ■ $l = 2$ cm, ■ $l = 3$ cm, ■ $l = 4$ cm, ■ $l = 5$ cm. Details about the theoretical modelling of harmonics can be found in Section 3.4.

From 2 cm upwards, the intensity of the 9th harmonic changes only slightly with the length, so 2.2 cm is an acceptable length for the central part. The difference between the intensity of the maximum for $l = 2$ and $l = 5$ cm is only 10%. The glass capillary waveguides were ordered from Wilmad, having an outer radius of ¼ inch, and inner radius of either 80 or 100 µm. The glass capillary waveguide was cut to a length of 10 cm in the lab (the mimimum length required to fit all of the compression fittings) using a standard glass cutting tool. Two holes were then drilled into the glass capillary waveguide. The holes were made using a 0.5 mm cadmium drilling bit.

3.5.3 Gas line

Figure 3.17 shows the experimental set-up for introducing the gas at the desired pressure into the glass capillary waveguide.

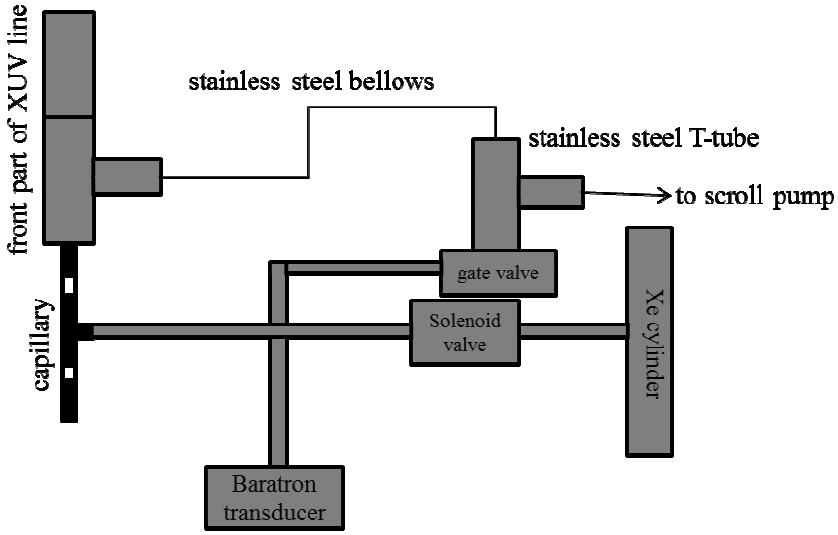

Figure 3.17 Schematic of the gas line designed for introducing gas into the glass capillary.

The capillary is pumped from both sides as can be seen from Figure 3.11 and Figure 3.13. The front part of the capillary is pumped by an Edwards scroll pump (35 m^3 h^{-1}) and the back part of the capillary is pumped by two turbomolecular pumps that are backed by a scroll pump (Edwards, 35 m^3 h^{-1}). It is assumed that the pressure in the middle part of the capillary is constant and equal to the gas cylinder pressure (based on earlier dynamic flow calculations [33]) with a rapid linear decrease in pressure moving away from the holes, falling to the background pressure at the end of the capillary. The pressure in the gas line was regulated by a flow controller (MKS 250E) that had a solenoid valve for fine pressure regulation and a baratron transducer for measuring the gas pressure in the middle part of the capillary. A pirani gauge could not be used to measure the pressure since it becomes insensitive to Xe pressures more than 2 mbar. Before each of the experiments, the gas line was evacuated so both of the gate valves were opened. The gate valves had to be closed when the gas was introduced to the gas line so that only the front part of the capillary was being pumped.

3.5.4 Spectrometer

A VM-502 spectrometer was used for the detection of high harmonics, with a concave holographic diffraction grating and a CCD detector. The spectrometer can have a wide operating range depending on the type of coating used on the diffraction grating. For the XUV generation experiments, a broadband XUV Al+MgF_2 coating was used. The grating efficiency is best for wavelengths between 120 and 150 nm (88% at 120 nm), but it could also be used at 100 nm (grating efficiency is around 4%) and at lower wavelengths with the diffraction efficiency being very low (less than 4%). For 60 nm the diffraction efficiency becomes negligible. This grating was the best choice at the time, because the iridium coating was no longer produced. The detector was a PIXIS-XO: 100 B camera that utilized CCD detection for very low energy x-ray detection. The quantum efficiency of the CCD was higher for 800 nm radiation (ca 50%) than for the 9th (13 eV) or 11th (17 eV) harmonic – less than 20%, which caused a few technical problems due to scattered light.

3.6 Experimental results

In this section, the experimental results showing the 11th harmonic signal as a function of gas pressure are shown. The 11th harmonic signal was recorded for three different pressures. Unfortunately, the glass capillary waveguide broke in the middle of these experiments, so it was not possible to collect the high harmonic signal for a wider range of gas pressures. Figure 3.18 shows intensity *versus* wavelength for the 11th harmonic in 8, 9 and 10 Torr of Xe.

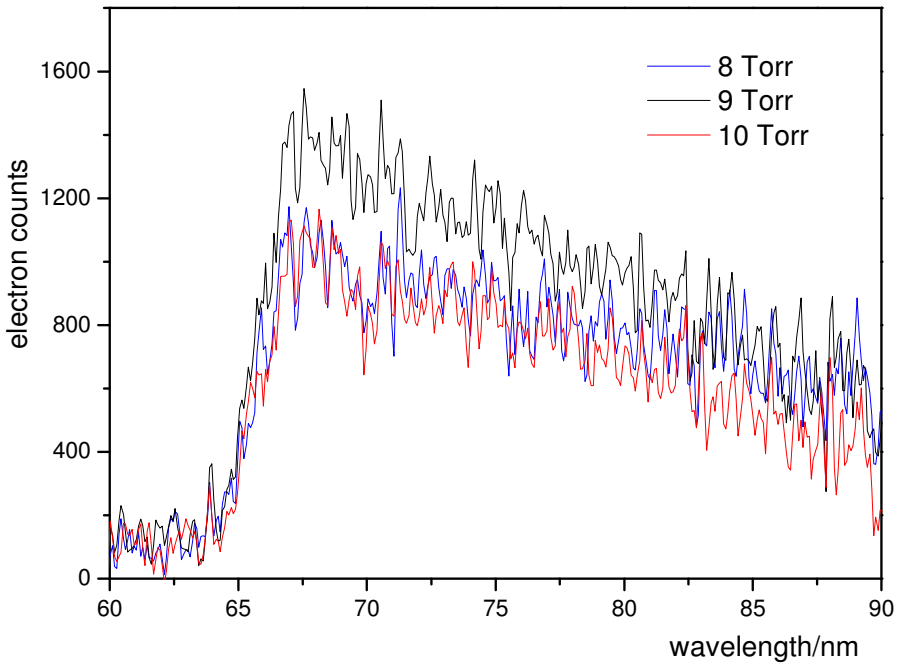

Figure 3.18 Intensity profiles of the 11th harmonic measured for three different Xe pressures inside the glass capillary. Shown is the number of counts registered by the CCD *versus* the wavelength. The wavelength assignment is only approximate, since calibration of the spectrometer was performed with a mercury lamp.

It is difficult to obtain any quantitative information about the harmonic, especially because the spectral profile is slightly broadened due to the contribution of scattered background 800 nm light. From these three pressures, it can be seen that the intensity of the 11th harmonic changes only slightly with pressure, and that the intensity is the highest for 9 Torr. The maximum intensity is around 68 nm, which is in fair agreement with the expected 72 nm. The spectrometer calibration was performed with a mercury lamp positioned outside the spectrometer. In order to reach a diffraction grating, the light from the mercury lamp had to pass through a fused silica window, which absorbs radiation significantly below 250 nm. Therefore, the calibration of the spectrometer was performed down to 253 nm only, so the pixel to wavelength conversion is only approximate for wavelengths below 100 nm.

3.7 Summary and outlook

This chapter describes the design of a femtosecond XUV source and theoretical simulations predicting the phase matching pressure for the 9th, 11th and 27th harmonics of 800 nm radiation. The XUV apparatus was successfully tested by generation of the 11th harmonic of the 800 nm radiation. Generation of the 11th harmonic of the 800 nm radiation (72 nm) was recorded at 8, 9 and 10 Torr of Xe in a capillary of radius, a = 100 μm. This femtosecond radiation can be used in gas phase photoelectron spectroscopy experiments, but is not so useful for photoelectron spectroscopy on surfaces. In order to study femtosecond laser-induced dynamics on surfaces, the femtosecond source must be at least 20 eV. This requires modification of the XUV apparatus, since the current spectrometer cannot detect high harmonics. The 27th harmonic of the 800 nm radiation (42 eV) would be a good starting wavelength for surface experiments.

3.8 References

1. P. A. Franken, G. Weinreich, C. W. Peters and G. Weinreich, *Physical Review Letters*, **7** (4), 118 (1961).
2. E. Hecht, *Optics*. (Addison-Weasley, 1987).
3. M. W. Hendrikx, *High harmonic generation in gas-filled capillary waveguides*. (PhD thesis, University of Twente, 2009).
4. T. Haarlammert and H. Zacharias, *Current Opinion in Solid State & Materials Science*, **13** (1-2), 13 (2009).
5. W. S. Fann, R. Storz, H. W. K. Tom and J. Bokor, *Physical Review B*, **46** (20), 13592 (1992).
6. W. S. Fann R. Storz, H. W. K. Tom and J. Bokor, *Physical Review Letters*, **68** (18), 2834 (1992).
7. M. Bauer, C. Lei, K. Read, R. Tobey, J. Gland, M. M. Murnane and H. C. Kapteyn, *Physical Review Letters*, **87** (2), 025501 (2001).
8. C.-F. Lei, *Using extreme-ulttraviolet pulses for time-resolved dynamics of molecules chemisorbed on metal surfaces*. (PhD thesis, University of Michigan, 2003).

9. C. Puglia, A. Nilsson, B, Hernnas, O. Karis, P. Bennich, and N. Martennson, *Surface Science*, **342** (1-3), 119 (1995).
10. M. L. Bocquet, J. Cerda and P. Sautetet, *Physical Review B*, **59** (23), 15437 (1999).
11. A. Eichler and J. Hafner, *Physical Review Letters*, **79** (22), 4481 (1997).
12. A. Eichler, F. Mittendorfer and J. Hafner, *Physical Review B*, **62** (7), 4744 (2000).
13. W. Eberhardt, T. Upton, S. Cramm and L. Incoccia, *Chemical Physics Letters*, **146** (6), 561 (1988).
14. H. Dachraoui, M. Michelswirth, P. Siffalovic, P. Bartz, C. Schafer, B. Schnatwinkel, J. Mattay, W. Pfeiffer, M. Drescher and U. Heinzmann, *Physical Review Letters*, **106** (10), 107401 (2011).
15. P. B. Corkum, *Physical Review Letters*, **71** (13), 1994 (1993).
16. K. J. Schafer, B. Yang, L. F. Dimauro and K. C. Kulander, *Physical Review Letters*, **70** (11), 1599 (1993).
17. N. H. Burnett and P. B. Corkum, *Journal of the Optical Society of America B Optical Physics*, **6** (6), 1195 (1989).
18. P. B. Corkum, N. H. Burnett, and F. Brunel, *Physical Review Letters*, **62** (11), 1259 (1989).
19. M. Bauer, *Journal of Physics D-Applied Physics*, **38** (16), R253 (2005).
20. C. G. Durfee, A. R. Rundquist, C. Backus, Z. Chang, C. Herne, H. C. Kapteyn and M. M. Murnane, *Journal of Nonlinear Optical Physics & Materials*, **8** (2), 211 (1999).
21. C. G. Durfee, A. R. Rundquist, C. Backus, C. Herne, H. C. Kapteyn and M. M. Murnane, *Physical Review Letters*, **83** (11), 2187 (1999).
22. E. A. J. Marcatili and R.A. Schmeltzer, *Bell System Technical Journal*, **43**, 1783 (1964).
23. J. P. Brichta, M. C. H. Wong, J. B. Bertrandt, H. C. Bandulet, D. M. Rayner and V. R. Bhardwaj, *Physical Review A*, **79** (3) (2009).
24. H. H. Telle, A. G. Urena, and R. J. Donovan, *Laser Chemistry: Spectroscopy, Dynamics and Applications*. (John Wiley & Sons, 2007).
25. A. Dalgarno and A. E. Kingston, *Proceedings of the Royal Society of London. Series A, Mathematical and Physical Sciences*, **259** (1298), 424 (1960).
26. C. T. Chantler, *Journal of Physical and Chemical Reference Data*, **24** (1), 71 (1995).

27. A. L'Huillier, X. F. Li, and L. A. Lompre, *Journal of the Optical Society of America B*, **7** (4), 527 (1990).
28. G. V. Marr and J. B. West, *Atomic Data and Nuclear Data Tables*, **18** (5), 497 (1976).
29. J. B. West and J. Morton, *Atomic Data and Nuclear Data Tables*, **22** (2), 103 (1978).
30. A. Rundquist, C. G. Durfee, Z. H. Chang, C. Herne, S. Backus, M. M. Murnane and H. C. Kapteyn, *Science*, **280** (5368), 1412 (1998).
31. E. Constant, D. Garzella, P. Breger, E. Mevel, C. Dorrer, C. Le Blanc, F. Salin and P. Agostini, *Physical Review Letters*, **82** (8), 1668 (1999).
32. Sharon Roessler. September 2011. Lebow Company. [online]. Available from: www.lebowcompany.com/foils_list.htm
33. E. T. F. Rogers, *Modelling of Capillary High Harmonic Generation*. (PhD thesis, University of Southampton, 2008).

CHAPTER 4

FS-LID OF CO AND OF NO ON Pd(111)

4.1 Abstract

The overall aim of the work described in this thesis is the study of the photoinduced reaction of CO + NO on the Pd(111) surface. To understand this reaction, it is necessary to understand the behaviour of the species adsorbed on Pd(111) individually. To this end, a number of femtosecond laser-induced desorption experiments (fs-LID) have been performed, which have been analysed in conjunction with previously obtained measurements using classic surface science techniques: reflection absorption infrared spectroscopy (RAIRS) and temperature programmed desorption (TPD).

4.2 Introduction

The CO + NO reaction on Pd takes place in 3-way car exhaust catalytic converters. In the catalytic converter, the reaction takes place on Pd nanoparticles deposited on a metal oxide support under atmospheric pressure, with the fundamental chemistry of the process still not fully understood. The first step towards a better understanding of the reaction is to investigate it on well-defined single crystal surfaces. For the studies described here, the well-defined Pd(111) surface was chosen as a model surface. In this chapter, the photodesorption of CO and NO adsorbed on the surface individually is discussed, before looking at the behaviour of the co-adsorbed system in the next chapter. Extensive research has been undertaken into CO and NO individually adsorbed on Pd(111), using a wide range of classic experimental and theoretical surface science techniques, for examples see [1–8].

The adsorption of CO on Pd(111) has been reviewed by Ozensoy *et al.* [3] as part of a study of the reaction of CO + NO on Pd(111) model catalysts. The study concluded that CO overlayers on Pd(111) at elevated pressures reveal similar adsorption structures to those in ultra high vacuum (UHV) conditions. The main findings for CO overlayers on

Pd(111) under UHV conditions as a function of coverage are detailed below. At a CO coverage of θ = 0.33 ML, scanning tunnelling microscopy (STM) studies [9] suggested the $(\sqrt{3}\times\sqrt{3})$R30° structure, with CO occupying primarily three-fold hollow adsorption sites. It was previously demonstrated [10, 11], using a combination of low energy electron diffraction (LEED) and RAIRS, that this structure results in a low C–O vibrational frequency of ~1850 cm^{-1}. Further increase in coverage leads to the formation of two c(4×2)R45° structures at θ = 0.5, where CO occupies either three-fold hollow or bridge sites [9]. Changes in the structure are associated with a change in the position of the C–O vibrational band to 1920 cm^{-1} as observed in RAIRS [10, 11]. Within the coverage range 0.5 < θ/ML < 0.75, various overlayer structures are proposed, and the position of the C–O vibrational band shifts further to ~1965 cm^{-1}. [11] STM and density functional theory (DFT) studies suggest that at this coverage, the adsorbed CO primarily occupies bridge sites [9]. At θ = 0.75 ML, saturation is obtained, leading to a (2×2) structure with CO residing on atop and three-fold hollow sites [9], with corresponding infrared (IR) frequencies at 2110 and 1895 cm^{-1}, respectively [10, 11].

Adsorption of NO on Pd(111) was described by Hansen *et al.* [12] using a combination of STM and DFT studies. In terms of their structure, NO overlayers are very similar to those of CO on Pd(111). Four different overlayer structures are observed for NO adsorbed on Pd(111) in the temperature regime from 100 to 300 K. The first structure that has long range order and a c(4×2) structure appears at θ = 0.5 ML. At θ = 0.625 ML, a c(8×2) structure is observed, and at θ = 0.75 ML a (2×2) structure is observed. The fourth structure does not have long range order, and appears at θ = 0.25 ML. In the same report, the long-standing controversy in assigning the adsorption sites to these structures *via* vibrational spectroscopic techniques is solved. DFT calculations, in combination with STM, predicted that for θ = 0.5 ML, NO molecules reside on three-fold hollow sites, for θ = 0.625 and 0.75 ML, they occupy three-fold hollow and atop sites. At room temperature, the saturation coverage for adsorption of NO on Pd(111) is 0.5 ML. Nakamura *et al.* [13] showed only one IR band positioned at 1539-1581 cm^{-1}, associated with the adsorption of NO on Pd(111) at room temperature, that would correspond to NO adsorbed in the three-fold hollow site.

As a complement to these classic surface science techniques, laser-induced desorption experiments can provide new insight into the chemical processes occurring, such as desorption, dissociation or chemical reaction. Fs-LID from a surface results in a distinctive non-linear relationship between the reaction yield and the absorbed laser fluence. This is in contrast to the linear rise in desorption yield with the absorbed laser fluence that is characteristic of continuous wave (cw-) or nanosecond-laser-induced photodesorption. Typically, yield-*vs*-fluence dependence has been parametrized by a power law of the form:

$$Y = aF^b . \qquad (4.1)$$

Y is the photodesorption yield, F is laser fluence, and a and b are the prefactor and exponent, respectively, with b ranging from 3 to 8, depending on the molecule and the surface [14]. The observed fluence dependence is introduced only empirically, and a clear deviation from this power law behaviour is found near saturation. Even though the power law has been used extensively, the physical meaning of the parameters, a and b in Equation 4.1 has not been explained successfully. In this thesis, the main focus is to study the CO and NO reaction for particular CO/NO coverages. In order to study the reaction or desorption of adsorbed species, the behaviour of the pure systems at these coverages needs to be explained. Therefore, a and b parameters were calculated for the three CO and NO coverages that were subsequently used in the experiments investigating co-adsorbed CO and NO. These parameters a and b are then explained qualitatively in terms of the different overlayer structures.

Photoinduced desorption serves as a starting place for exploring the complicated dynamics associated with adsorbate covered surfaces. It is very important to find the link between the photoinduced processes and the real world processes that involve a thermal mechanism. A lot of models treat photoinduced desorption as an activated process in a one dimensional framework [15, 16, 17]. However, in some models, the process can be divided into two steps: vibrational excitation and subsequent desorption. The vibrational excitation step can be modelled either quantum mechanically [18] or with electronic or lattice friction, within the electronic friction model [19]. The desorption step can be modelled as surmounting the activation barrier, either by the Arrhenius equation in the friction approach, or quantum mechanically. The important thing is, however the system is modelled, that the activation barrier for photoinduced desorption is the same

as the one used to describe thermally driven processes, even if the reaction mechanisms are different. [20, 21]

A significant number of investigations of surface femtochemistry have studied the desorption of diatomic molecules on transition metal surfaces such as NO on Pt(111) [22] and Pd(111) [19, 23–24], O_2 on Pt(111) [17, 25–26] and Pd(111) [27, 28], and CO on Pt(111) [26], Cu(100) [20], Ru(0001) [21, 29], Pt(111) [26], Cu(111) [30] and Pt(533) [31]. Many techniques have been used to study femtosecond laser-induced desorption, such as fluence dependence of the reaction yield (yield-FD), two pulse correlation experiments (2PC), state selective detection of the internal energy content, second harmonic generation (SHG) and sum frequency generation (SFG). In the next two paragraphs, a brief overview of previous femtosecond laser-induced desorption experiments of NO on Pd(111) and CO on Pd(111) will be presented.

The first investigation of desorption of a molecular adsorbate induced by subpicosecond laser excitation was performed by Prybyla *et al.* [24] for NO adsorbed on a Pd(111) surface. The measured desorption yield as a function of the absorbed fluence of the 200 fs pulses showed a non-linear rise that could be represented by Equation 4.1 with an exponent, $b = 3.3$, shown in Figure 4.1.

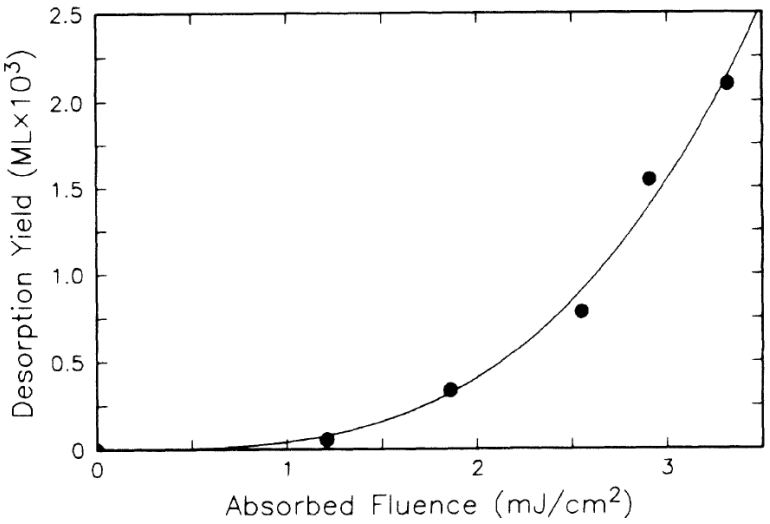

Figure 4.1 Desorption yield of NO as a function of the absorbed laser fluence. The solid line is a power-law fit to the data. Figure taken from reference 24.

The experiments used resonance enhanced multiphoton ionisation (REMPI) to detect the number of desorbed molecules as well as to measure the internal energy distributions of the desorbing species. The measured vibrational energy distributions and desorption cross sections were much higher than in thermal desorption of NO/Pd(111), induced by laser pulses of nanosecond duration. The high vibrational energy content of the desorbed NO molecules can be explained by desorption *via* the excited electronic state of the NO-Pd complex. Such a process may occur *via* a repulsive or attractive excited state potential energy surface. For NO on Pd(111) the relevant electronic excitation probably involves the $2\pi^*$ valence levels. The high desorption cross section and non-linear fluence dependence of the yield can be explained in terms of desorption induced by multiple electronic transitions (DIMET), shown in Figure 1.4.

In this model, the laser produces an enhanced flux of electrons for each absorbed photon above the energy threshold required for the relevant electronic transition in the adsorbate–substrate complex. These electrons then induce multiple electronic transitions between the ground and excited electronic state of a molecule, with each transition increasing the vibrational energy in the complex. The important point about the mechanism, is that each transition occurs before vibrational relaxation can occur. To obtain a better understanding of the mechanism, experiments using the 2PC technique have been performed. These measurements proved that the reaction is driven by hot electrons, as the full width at half maximum (FWHM) of the correlation trace was ~600 fs, much less than the electron-phonon equilibration time, which is 1-2 ps.

Szymanski *et al.* [32] investigated temperature dependant femtosecond desorption induced in the CO/Pd(111) system. The non-linear dependence of the desorption yield *versus* fluence was measured at a number of temperatures. The method involved saturating the CO/Pd(111) surface at 380 K, briefly annealing it at that temperature, and then lowering it to a desired temperature in the range 85 K to 375 K. This ensured that the coverage remained constant in all of the experiments. The experiments showed a dependence of the exponent on the temperature, with a value ranging from 8.8 at 200 K to 6.7 at 375 K. As well as the change in exponent, an increased photoyield at 375 K with respect to 200 K was also observed. Reasons for these observations will be given in the next two paragraphs.

Some complementary 2PC experiments also showed significant differences in the observed FWHM with temperature: ~3 ps at 200 K, compared with ~20 ps at 375 K [32]. The model used to explain the data was the friction model, with a temperature dependant electronic friction and a temperature independent phonon friction. Simulations predicted the electron adsorbate coupling time, $\tau_e \sim 500$ fs which suggested that the desorption was electron mediated. A phonon-adsorbate coupling time predicted by the same model was ~ 20 ps. The influence of the phonons on the desorption yield only became effective after the hot electrons have equilibrated with the phonons. The phonon contribution could not explain the observed broadening of the 2PC FWHM within the proposed model.

The observed broadening of the 2PC FWHM, the increased photoyield and decrease in the non-linearity with the increased initial substrate temperature could only be explained by the influence of the initial substrate temperature. The measured linear relationship between the first shot yield and the initial substrate temperature was very similar to the simulated linear relationship between the peak desorption rate and initial substrate temperature. This suggested that at higher initial substrate temperatures there would be an increase in the population of vibrationally excited states so fewer transitions were required and increased the probability of reaching the desorption continuum.

The CO/Pd(111) system can be compared with the only other two CO/metal systems for which 2PC has been performed: CO/Cu(100) [20] and CO/Ru(0001). [29] Photoinduced desorption for CO on Cu(100) showed a highly nonlinear rise (Equation 4.1) with $b = 8$ and a 2PC FWHM ~3 ps. Hence the reaction was considered to be purely electron mediated. For CO/Ru(0001), the FWHM of the 2PC measurements was ~20 ps, with $b = 4.5$, therefore the reaction was said to be purely phonon mediated.

The difference between these two systems was explained in terms of the DIMET mechanism. Substrate electrons were probably excited into the $2\pi^*$ CO resonance, so that the position of this resonance determined whether there would be enough electrons of sufficient energy to excite the adsorbate–substrate complex. For Cu(100), a doublet resonance at 2.4 and 3.9 eV above the Fermi level was observed and a resonance at 4.9 eV above the Fermi level was detected on Ru(0001).

When the CO/Pd(111) system was compared with the CO/Ru(0001) system in terms of the DIMET mechanism, then the $2\pi^*$ CO resonance would be nearly 1 eV closer to

the Fermi level for CO adsorbed on Pd(111) (similar to the position of the resonance for CO/Cu(100)), explaining the difference in the mechanism of the photoinduced desorption.

The remainder of this chapter presents the results of experiments investigating the fs-LID of CO on Pd(111) and NO on Pd(111). These systems are also characterized using standard surface science techniques, RAIRS and TPD.

4.3 Experimental

4.3.1 RAIRS and TPD experiments

RAIRS data were recorded using a Thermo Nicolet 6700 Fourier transform infrared (FTIR) spectrometer with a liquid nitrogen cooled mercury cadmium telluride (MCT) detector. All RAIR spectra shown were the result of the coaddition of 256 scans and were taken at a resolution of 4 cm^{-1}. In the RAIRS experiments, an initial clean surface spectrum was taken (a background spectrum). The sample gas was then admitted to the vacuum chamber *via* a high precision leak valve, and a sample spectrum was then collected.

TPD experiments were carried out using a Hiden pulse ion counting quadrupole mass spectrometer (QMS), at a heating rate of 0.5 K s^{-1}, and the desorption yields were collected for up to 5 masses simultaneously.

Care was taken to ensure that the sample was positioned in the same place for each experiment, so that TPD spectral intensities could be compared easily. The integrated areas of the desorption peaks were used to estimate the relative amounts of the desorption products evolved from the surface. The integrated areas were found by subtracting the background intensity from the spectrum and then using the trapezium rule to find the area below the TPD peak.

As described in Chapter 2, the vacuum chamber has two levels on which different experimental apparatus is located. RAIRS experiments were performed at a different level to the TPD and fs-LID experiments. The pumping speed is different for different levels of the UHV chamber, therefore the amount of gas adsorbed on the metal surface depends on the experimentation level. Hence for the same exposure, the coverage in the

RAIRS experiments will be slightly different to the coverages in the TPD and fs-LID experiments.

4.3.2 Photoinduced desorption experiments

All of the photodesorption experiments were performed with a regeneratively amplified Ti:Sapphire laser system (790 nm, ~50 fs pulses, 2.5 mJ/pulse) operated at a repetition rate of 20 Hz. The QMS was synchronized with the laser, and the laser light was incident at 45˚ with respect to the surface normal. The experimental set up for these experiments was described in detail in Chapter 2, Section 2.8.

4.4 Results and discussion of RAIRS and TPD experiments

Before presenting the results, it is important to mention that in the TPD and LID experiments involving carbon monoxide, the ^{13}CO isotope was used. The reason for this was to distinguish between any photochemically produced CO_2 and N_2O which would otherwise have the same mass. There is no isotope effect associated with desorption of CO or ^{13}CO in TPD experiments because the process is phonon driven. The isotope effect in fs-LID experiments, where the desorption process involves electronic excitations, is negligible because of the small difference in reduced mass between ^{12}CO and ^{13}CO. [14] All of the RAIRS experiments were performed with ^{12}CO because it was easier to analyse spectra that contained just one species, ^{12}CO, whereas in ^{13}CO experiments spectra would contain vibrational peaks associated with ^{12}CO and ^{13}CO. The position of ^{13}CO stretching frequencies would be slightly shifted towards lower wavenumbers, because of the slightly different reduced mass. However the coverage dependent behaviour of the CO in both cases would be the same.

4.4.1 RAIRS and TPD characterisation of CO/Pd(111)

All of the RAIR spectra were collected in separate experiments performed by a co-worker. However, the data had not been analysed, so it is analysed and discussed here because of its relevance to the fs-LID results described in this thesis. Figure 4.2 shows RAIR spectra as a function of increasing CO coverage on Pd(111) at $T = 320$ K.

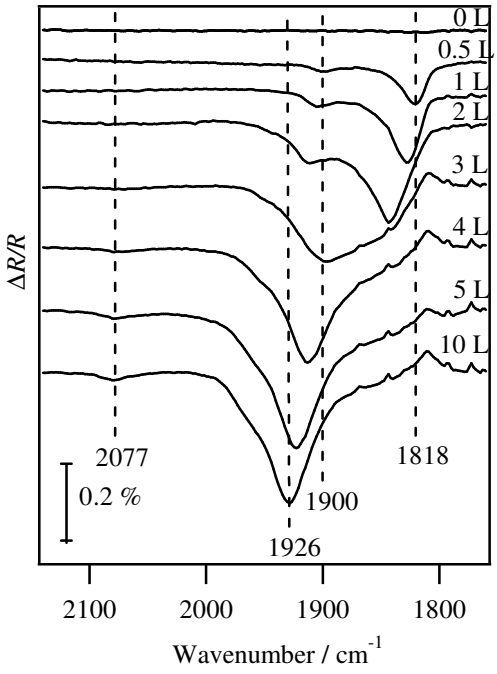

Figure 4.2 RAIR spectra taken for different coverages of CO on Pd(111) at 320 K. Exposure is varied from 0 to 10 L.

The exposure was measured in Langmuirs (1 L = 10^{-6} Torr s). At low exposure, 0.5 L, a sharp peak at 1818 cm^{-1} is observed. This vibrational frequency agrees well with that of previous RAIRS studies [1] at 1823 cm^{-1} and is assigned to CO adsorbed in three-fold hollow sites. Another, weaker, peak at 1900 cm^{-1} is also observed. This peak probably corresponds to CO adsorbed on defect sites [33]. With increasing coverage, both of the peaks shift to higher wavenumbers because of dipole coupling, until the main C-O stretching frequency is observed at 1926 cm^{-1} for 10 L exposure. Following a 2 L exposure, the low wavenumber C-O vibrational band moves to 1828 cm^{-1}. This exposure probably corresponds to a $\left(\sqrt{3}\times\sqrt{3}\right)R30^\circ$ LEED structure, θ = 0.33 ML, since in previous RAIRS studies [1] this structure generates a similar band at 1836 cm^{-1}. Above a coverage of 0.33 ML the structure starts to change. At 3 L an extremely broad band is observed in the RAIR spectrum in Figure 4.2. This corresponds to the coverage regime between 0.42-0.43 ML [1]. Between θ = 0.33 and 0.5 ML, CO occupies either bridge or three-fold hollow sites [9]. After 0.5 ML, CO also begins to occupy atop sites [1, 9]. In Figure 4.2 this corresponds to an exposure of 5 L, where the CO stretching frequency for the atop site is seen at 2077 cm^{-1}. TPD data recorded as a function of coverage also

agreed well with previous studies [5, 34], with one main desorption peak at a peak temperature at 530 K. This desorption peak corresponds to the desorption of CO from the three-hollow sites [34]. TPD spectra after laser irradiation were the same as TPD spectra without laser irradiation because only a few points on the sample were irradiated with the laser, so the depleted area was negligible.

Figure 4.3 shows TPD spectra performed after femtosecond laser-induced desorption at 320 K for 3 different ^{13}CO exposures: 2, 4 and 10 L.

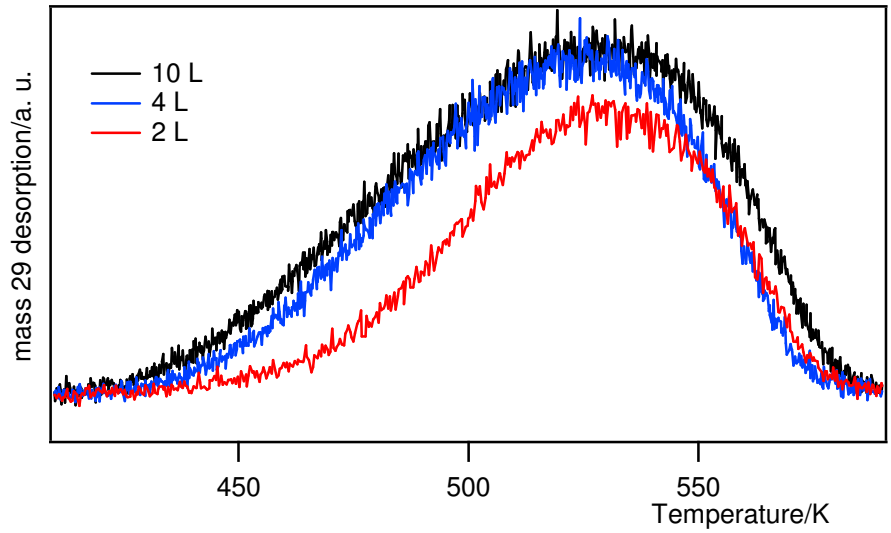

Figure 4.3 TPD spectra of ^{13}CO/Pd(111) taken at 2 L —, 4 L — and 10 L — exposure. The heating rate was 0.5 K s^{-1}. The desorption yield was monitored simultaneously for 3 masses (mass 29, mass 45 and mass 28) by the QMS.

From the TPD curves the integrated areas under the main mass 29 desorption peak were calculated. The average areas obtained from several TPD experiments are shown in Table 4.1. Areas under the TPD curves were reproducible within ± 5%. This percentage was calculated from standard deviation of the data.

Table 4.1 Average integrated areas for different exposures of ^{13}CO on Pd(111) at T = 320 K.

Exposure/L	Mass 29 integrated area under TPD curve
0	0
2	5.0×10^5
4	6.7×10^5
10	8.0×10^5

In order to undertake detailed analysis of photodesorption data, it is necessary to estimate the coverage for a particular exposure. The relative coverage can be calculated from the calibration curve that shows the mass 29 TPD integrated area *versus* exposure, shown in Figure 4.4. Error bars are calculated as ± 5% of the average values shown in Table 4.1. From Figure 4.4 it can be observed that saturation is reached for exposure around 10 L. The saturation coverage at room temperature corresponds to a coverage ~0.6 ML [1]. For the exposure of 2 L the integrated area under the mass 29 TPD curve was 60% of the area for 10 L. Hence a 2 L exposure corresponds to a coverage of ~0.33 ML.

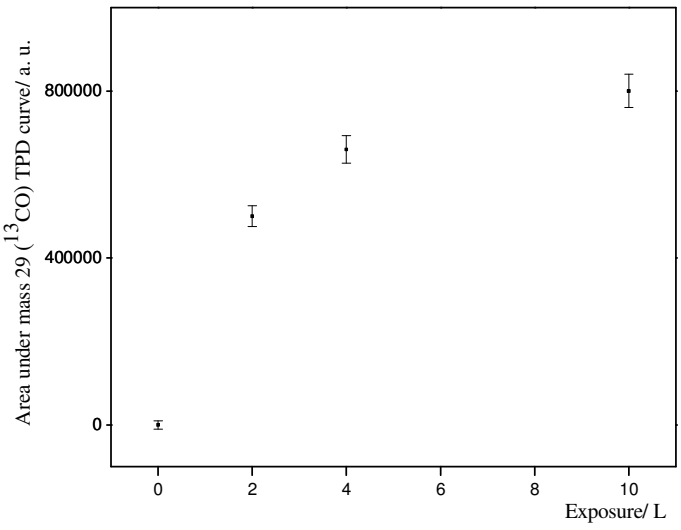

Figure 4.4 Integrated area under mass 29 (^{13}CO) desorption curve as a function of ^{13}CO exposure on Pd(111) at T = 320 K.

As was discussed in Chapter 2, Section 2.8.2, the desorption energies for first order desorption can be estimated from the Redhead [35] equation (Equation 2.12). From Figure 4.2, the temperature of the desorption peak, T_p is ~530 K, hence the first order desorption energy for CO is 147 kJ mol^{-1}.

4.4.2 RAIRS and TPD characterisation of NO/Pd(111)

Figure 4.5 shows RAIR spectra of NO on Pd(111) at room temperature for a range of different exposures. Three bands are observed, at 1816 cm^{-1}, 1652 cm^{-1} and 1518-1572 cm^{-1}.

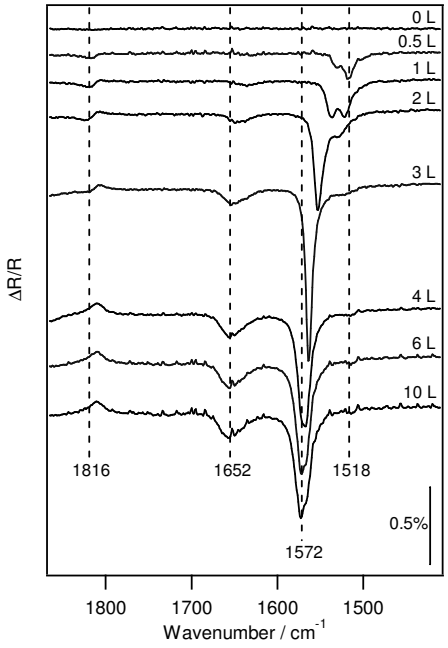

Figure 4.5 RAIR spectra for NO/Pd(111) as a function of NO exposure, at T = 320 K.

Here, the main vibrational band at 1518-1572 cm^{-1} is assigned to the NO stretching frequency for NO adsorbed in a three-fold hollow site. This assignment is based on the only previous RAIRS room temperature study of NO/Pd(111) [13]. The main band shifts from 1518 cm^{-1} at 0.5 L to 1572 cm^{-1} at 10 L exposure. A band at 1816 cm^{-1} appears at 0.5 L, which increases in intensity until an exposure of 1 L is reached, and then decreases until it disappears at 3 L exposure. This band is assigned to the presence of a

small amount of CO adsorbed on three-fold sites which is displaced gradually by NO. The assignment is based on recent STM and DFT studies [9] and also on TPD and RAIRS data of CO + NO (see Chapter 5) that show clearly that NO displaces CO. This CO adsorption occurs because there is background CO gas in the UHV chamber which adsorbs during the cooling of the sample from annealing (1100-1200 K) to the experimentation temperature (320 K). The amount of CO adsorbed on Pd(111) from the background gas can be estimated from RAIR spectra and from TPD experiments. If the area under the three-fold hollow CO peak in Figure 4.5 (NO/Pd(111)) is compared with the area under the three-fold hollow CO peak for Pd(111) saturated with CO, then ~6% of the Pd(111) is contaminated with background CO. The same procedure can be applied for TPD experiments, and the contamination is about 5%. The band at 1652 cm^{-1} can be assigned either to NO adsorbed in bridge sites, as postulated by DFT calculations [36], or to NO adsorbed on defect sites [37]. A band of a similar frequency was observed but not assigned, in experiments by Xu *et al.* [37], where CO and NO were coadsorbed. They suggested that NO is observed in the bridge site due to the influence of a small amount of CO. In addition, they studied CO and NO co-adsorption on Pd(100). In this case, the NO band appears around 1652 cm^{-1}. [37] Figure 4.5 clearly shows that the band at 1652 cm^{-1} increases in intensity, even after CO is replaced by NO, hence this band is probably more likely due to NO adsorbed on (100) steps.

TPD spectra of NO adsorbed on Pd(111) typically show that there is no NO dissociation [13], or that the dissociation is negligible [38, 39]. Here, TPD spectra of NO on Pd(111) show a small, but significant, amount of desorption of both N_2 (mass 28) and N_2O (mass 44), as well as NO (mass 30). This is probably due to the presence of defect sites on the surface [39]. Table 4.2 shows the integrated areas under mass 28 (N_2/ CO), mass 30 (NO) and mass 44 (N_2O/ CO_2) TPD desorption curves for exposures of 2, 4 and 10 L NO. The absolute percentage of NO dissociation could not be calculated as it is difficult to quantify the effects of spectrometer sensitivity and pumping speeds, making absolute values difficult to obtain; therefore, relative yields are calculated. The relative yield of mass 28 (CO/ N_2) or mass 44 (CO_2/ N_2O) is calculated as the ratio of the integrated area of the TPD curve in question, to that of the mass 30 TPD curve [39].

Table 4.2. Integrated areas under the TPD curves for mass 28 (N_2/ CO), 30 (NO) and 44 (N_2O/ CO_2) for 3 different NO exposures. The areas under the TPD curves are reproducible within ± 5% (calculated from several TPD experiments) and relative areas (with the respect to the area of mass 30) contain 7% uncertainty (calculated from the ratio of errors in the area under the TPD curves).

	TPD				
	mass 28		mass 44		
	Integrated area (A_{28})	Relative integrated area (A_{28}/A_{30})	Integrated area (A_{44})	Relative integrated area (A_{44}/A_{30})	mass 30 integrated area (A_{30})
2 L NO	2.2×10^5	0.52	4.6×10^4	0.12	4.0×10^5
4 L NO	1.2×10^5	0.22	3.7×10^4	0.07	5.5×10^5
10 L NO	1.2×10^5	0.20	4.0×10^4	0.07	6.1×10^5

From Table 4.2 it can be noted that the relative areas (yields) for mass 28 (CO/ N_2) and mass 44 (CO_2/ N_2O) decrease with increasing NO exposure. This means that the fraction of dissociation is higher at lower NO coverage. The interpretation of these results is easier if it is discussed in combination with the TPD spectra shown in Figure 4.6.

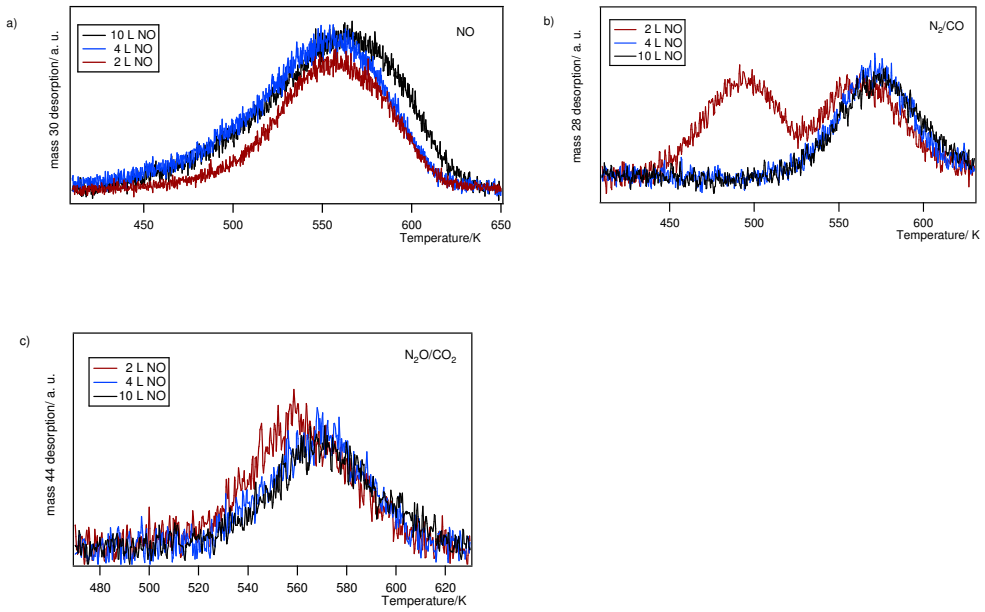

Figure 4.6 TPD spectra of **a)** mass 30 (NO), **b)** mass 28 (N_2/ CO) and **c)** mass 44 (N_2O/ CO_2) following NO adsorption on Pd(111) at T = 320 K taken at 2 L —, 4 L — and 10 L — exposure. The heating rate was 0.5 K s^{-1}. The desorption yield was monitored simultaneously for 3 masses (mass 28, mass 44 and mass 30) by the QMS.

TPD curves are shown for masses 30 (NO) (Figure 4.6a), 28 (CO/ N_2) (Figure 4.6b) and 44 (CO_2/ N_2O) (Figure 4.6c). The TPD curve for mass 30 (NO) shows one desorption peak at 560 K corresponding to NO adsorbed in a three-fold hollow site. The slightly higher peak temperature in TPD spectra of pure NO, compared to the peak temperature of pure ^{13}CO on Pd(111), suggests a stronger metal-adsorbate bonding. The desorption energy for the first order desorption can be estimated from the Redhead [35] equation (Equation 2.12). From Figure 4.6, the temperature of the desorption peak, T_p is ~560 K, hence the first order desorption energy for NO is 156 kJ mol^{-1}.

The position of the maximum slightly changes with coverage, but the desorption kinetics will not be discussed in this thesis, as only three exposures have been studied. The mass 44 (CO_2/ N_2O) TPD curves for 4 and 10 L exposure show one desorption peak at the same peak temperature as for mass 30 (NO), indicating that mass 44 (CO_2/ N_2O) is N_2O rather than CO_2. For 2 L NO, the mass 44 (CO_2/ N_2O) peak is broader, indicating the desorption of not only N_2O, but perhaps also CO_2 as well. The mass 28 (CO/ N_2) desorption curves have only one desorption peak at 560 K for 4 and 10 L exposure, but for 2 L exposure there are two desorption peaks, at 560 K and 490 K. This

suggests that at 2 L mass 28 desorption is due to both CO (desorption peak at 490 K) and N_2 (desorption peak at 560 K) desorption.

For the analysis of the photodesorption results, it is important to bear in mind that the photodesorption of NO for 2 L exposure is influenced by the highest fractional dissociation of NO (Table 4.2). TPD curves for mass 28 (CO/ N_2), 30 (NO) and 44 (N_2O/ CO_2) together with the relative yield for mass 28 (CO/ N_2) and 44 (N_2O/ CO_2) are similar for 4 and 10 L exposure, the biggest difference is in the area under the mass 30 (NO) desorption curve. In order to determine relative coverage, a calibration curve for NO is presented in Figure 4.7.

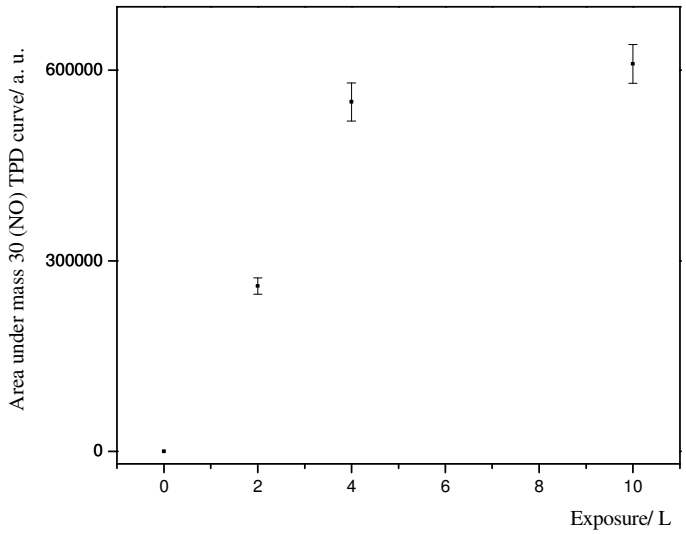

Figure 4.7 Integrated area under mass 30 (NO) TPD desorption curve as a function of NO exposure on Pd(111) at T = 320 K.

Similar to the ^{13}CO calibration curve, for each of the exposures, several TPD areas were calculated and then the average area was plotted. The error bars represent 5% error in the area calculated from the standard deviation of the data. From Figure 4.7 it can be seen that the area under the mass 30 TPD curve increases linearly with exposure until 4 L and then it plateaus. After a 10 L exposure the saturation coverage (0.5 ML) is reached. Since 2 L represents about 40% of the area for 10 L exposure, then a 2 L exposure corresponds to a coverage of ≈0.2 ML.

4.5 Analysis procedure

The experimental procedure for obtaining yield-*vs*-fluence dependence curves is described briefly here but was already described in Chapter 2. One example of a yield-*vs*-fluence dependence curve for NO on Pd(111) is shown in Figure 4.8.

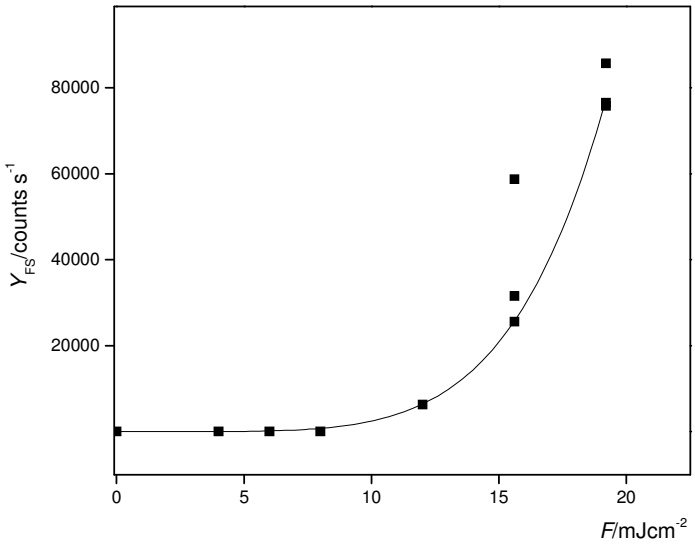

4.8 Example of a yield-*vs*-fluence dependence curve. This curve is for NO on Pd(111) at an NO exposure of 4 L, T = 340 K. ■ represent all measurements for a particular fluence (up to 3 data points), and — represents a power fit to the data, $Y_{FS} = aF^b$.

The parameters a and b are are used to characterize and compare the photodesorption behaviour of ^{13}CO and NO systems and are obtained from curves such as this one. After a particular gas (CO or NO) has been dosed on a clean surface, a set of depletion curves is collected by the QMS operating in a single shot mode. Figure 4.9 shows examples of two sets of depletion curves collected at two particular laser fluences.

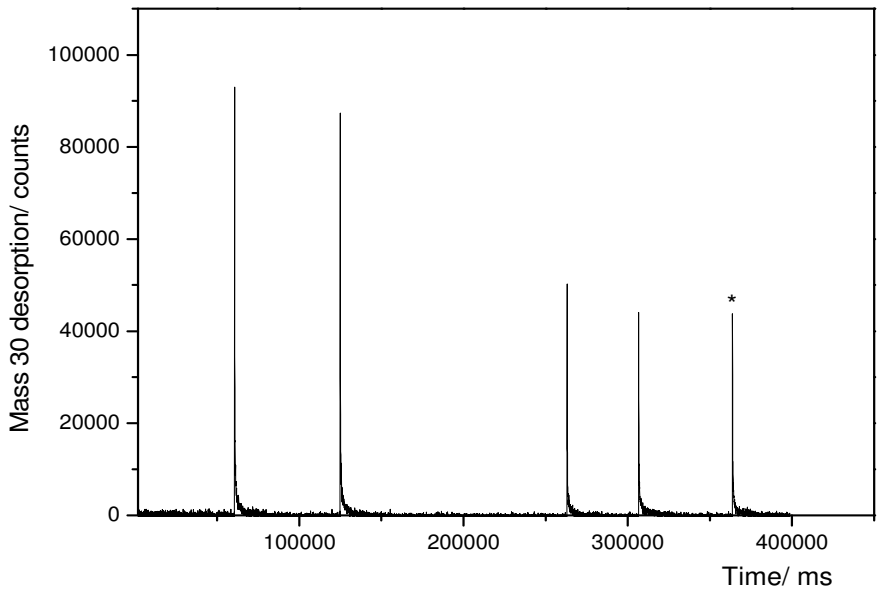

Figure 4.9 Five different depletion curves obtained from 5 different spots on a sample during one experiment for NO photodesorption. The exposure was 2 L. The first two depletion curves were taken at F = 24.4 mJcm^{-2}, the other three at F = 19.5 mJcm^{-2}. The first depletion curve, assigned with a *, will be shown in more detail in the next figure.

Depletion curves show the mass 30 desorption yield recorded every 50 ms, after each laser pulse. After approximately 400 laser shots, the surface is totally depleted and the desorption yield is equal to the background signal, or slightly higher because of diffusion of the adsorbed molecules into the illuminated area. If one of the depletion curves is shown in the form of the mass 30 desorption yield as a function of laser shot number, as is shown in Figure 4.10, then a biexponential decay curve can be fitted through the data points.

In order to determine the parameters that describe the photodesorption of ^{13}CO and NO and that enable a comparison of these two systems, the first shot yield needs to be calculated. Desorption recorded after the first laser shot is the most accurate because the initial number of molecules on the surface is the highest and so is the number of desorbed molecules. The first shot yield is calculated from a biexponential fit to the experimental data using a least squares method.

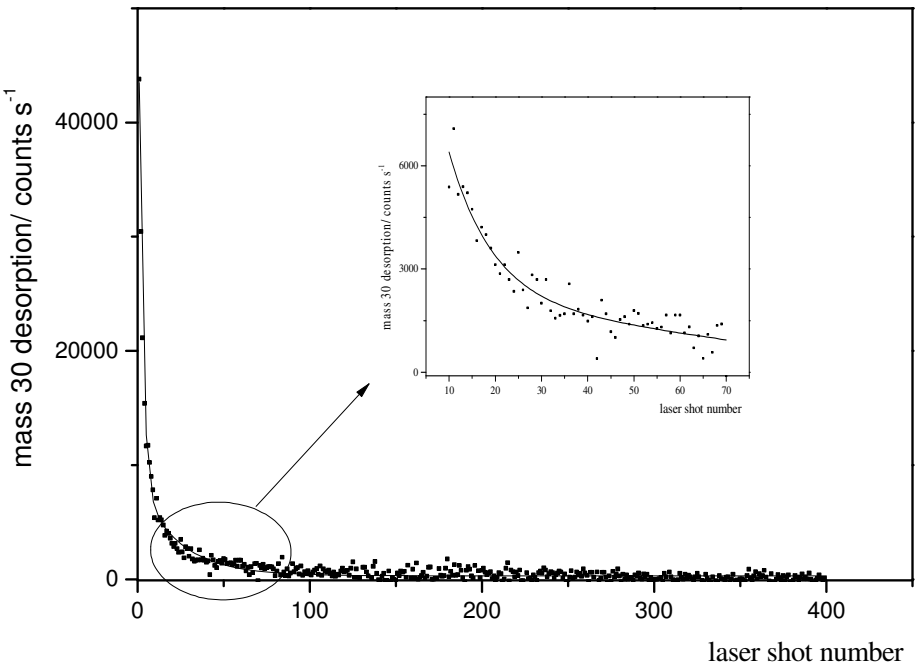

Figure 4.10 The depletion curve, assigned by a *, selected from Figure 4.9. The data points are assigned by ■, and the biexponential curve by —. The first shot yield is calculated from the biexponential curve.

All of the first shot yields obtained, either for the same, or for different fluences are plotted on the graph presented in Figure 4.8.

The above procedure was used to analyse all of the data. Yield-*vs*-fluence dependence curves will be presented first for ^{13}CO on Pd(111) and then for NO on Pd(111).

4.6 Results and discussion of fs-LID experiments

4.6.1 Fs-LID of CO on Pd(111)

Yield-*vs*-fluence dependence curves were obtained for 3 different exposures of ^{13}CO: 2, 4 and 10 L, for laser fluences between 0 – 35 mJ cm^{-2}. These are shown in Figure 4.11. Table 4.3 shows values of parameters obtained from power fits.

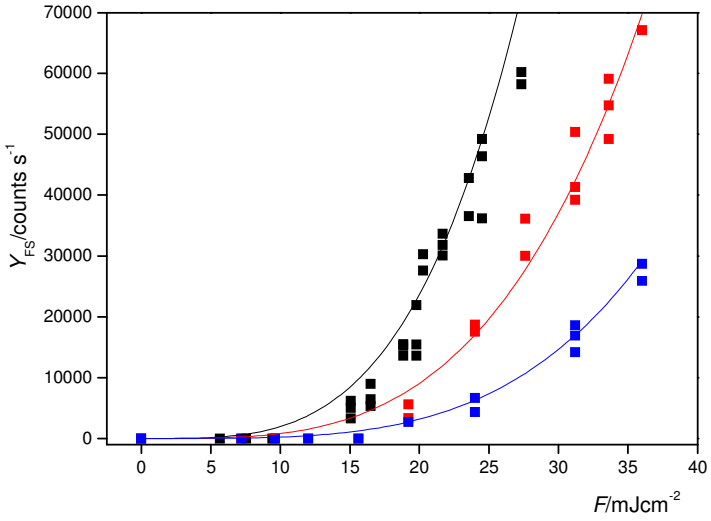

Figure 4.11 Yield-*vs*-fluence dependence curves for 2, 4 and 10 L exposure of ^{13}CO on Pd(111), at T = 340 K. ■ represents data for 10 L exposure, ■ represents data for 4 L exposure and ■ represents data for 2 L exposure. Solid lines are power fits ($Y_{FS} = aF^b$) to the data: ─ 10 L, ─ 4 L, ─ 2 L.

Table 4.3 Parameters a and b obtained by a linear fit, $\ln Y_{FS} = \ln a + b \ln F$ or by a power fit, $Y_{FS} = aF^b$ for the yield-*vs*-fluence dependence curves for the photodesorption of ^{13}CO on Pd(111) shown in Figure 4.11. R^2 values provide the information about goodness of fit.

10 L ^{13}CO	$Y_{FS} = aF^b$	$a = 0.5 \pm 0.3$	$R^2 = 0.957$
		$b = 3.6 \pm 0.2$	
	$\ln Y_{FS} = \ln a + b \ln F$	$a = 1.1 \pm 0.8$	$R^2 = 0.889$
		$b = 3.3 \pm 0.3$	
4 L ^{13}CO	$Y_{FS} = aF^b$	$a = 0.3 \pm 0.1$	$R^2 = 0.994$
		$b = 3.5 \pm 0.1$	
	$\ln Y_{FS} = \ln a + b \ln F$	$a = 0.5 \pm 0.2$	$R^2 = 0.986$
		$b = 3.3 \pm 0.1$	
2 L ^{13}CO	$Y_{FS} = aF^b$	$a = 0.04 \pm 0.01$	$R^2 = 0.966$
		$b = 3.8 \pm 0.1$	
	$\ln Y_{FS} = \ln a + b \ln F$	$a = 0.045 \pm 0.005$	$R^2 = 0.999$
		$b = 3.73 \pm 0.04$	

The experimental data was fitted to the power function with the parameters *a* (preexponential factor) and *b* (power exponent) in the power fit obtained in two ways: either directly by fitting the power function or by fitting the straight line, $\ln Y_{FS} = \ln a + b \ln F$ using non-linear regression analysis. Both methods gave the same value for the parameters within experimental error (Table 4.3). The value of the parameter *a* will be discussed only using the values obtained from the power fit, because the error was smaller by this method.

As was mentioned earlier in this chapter, the physical meaning of the parameters *a* and *b* is not well understood. Hence it is very difficult to compare these parameters with those obtained by others, for example Szymanski *et al.* [32]. However, it is possible to compare the parameters for different coverages in the ^{13}CO on Pd(111) adsorption system with these for the NO on Pd(111) system in this experimental set-up.

One of the problems in finding a physical meaning for the parameters is that a power law is just an empirical law. However, it is used in almost all papers published studying fs-LID, for example Szymanski and co-workers [32]. If the photodesorption of the molecules from the surface was treated as a direct multiphoton process, as for gas phase molecules, then the product yield would scale as F^n, where *n* corresponds to the number of photons. However, this is not the case for fs-LID from surfaces. Even if the desorption efficiency from excited states was one, the absorption cross section would have to be impossibly large to satisfy the high desorption yield that is typical for fs-LID from surfaces. Instead, two models are usually used: the electron friction model [40] and the DIMET model. These models will be discussed only briefly below, since they are explained in detail in Section 1.8 of the Introduction.

In the electron friction model, one can show [40] that if there are *b* effective steps below the vibrational threshold *D*, on average the energy *D*/*b* is transferred to a bond in each step of the ladder, and the desorption yield will be proportional to F^b. In the DIMET model, short, intense laser pulses cause multiple excitations of the adsorbate. Often, the hot electrons are attached to the adsorbate and a negative ion resonance is formed. During the action of the laser pulse by vibration-electron coupling, the adsorbate-surface bond becomes vibrationally hot, thus leading to ladder climbing in the ground electronic state which results in desorption [15]. Therefore, in this case *b* is connected with the number of electronic excitations, but it is not simply the case that *b* = 3 means three electronic excitations. Consequently, until there is a better

explanation, *b* seems to be more or less a fitting parameter. The meaning of the prefactor *a* is even more difficult to explain. It is related to the reaction cross section, which depends on many parameters, such as the wavelength of the photon, and of course on the properties of the metal substrate [41].

From the above discussion, it can be seen that the comparison of the fits described in this thesis with those of others is very difficult, because there is a lot of arbitrariness due to the fact that the fitting function depends on the experimental parameters which will vary from one laboratory to another. However, for the systems described in this thesis, the pure ^{13}CO system, and later on the pure NO system, it is justified to use an empirical power law to observe a trend in the parameters *a* and *b* as a function of coverage.

From Figure 4.11 and Table 4.3, the following trends for the *a* and *b* parameters for ^{13}CO desorption from Pd(111) are observed. The power exponents *b*, for all 3 exposures, are almost the same within experimental error, with an average value, $b = 3.6 \pm 0.2$. For the prefactor, *a*, a decreasing value is observed with decreasing exposure. It is difficult to quantify the prefactor precisely because the error is the same order of magnitude (sometimes even as high as 50% of the actual value) as the prefactor. It decreases slightly from 0.5 ± 0.3 to 0.3 ± 0.1 when the exposure is changed from 10 to 4 L. It decreases more when the exposure is changed from 4 to 2 L: from 0.3 ± 0.1 to 0.04 ± 0.01.

From the calibration curve for ^{13}CO (Figure 4.4), it can be seen that the surface is almost saturated following a 4 L exposure of ^{13}CO, hence the photodesorption yield should be similar to that for a 10 L exposure, therefore a slight change in the prefactor *a* is expected. The prefactor is ~1.7 times lower for 4 L exposure than 10 L exposure. The change in the prefactor is higher than the change in the coverage, or in the overlayer structure, so only a trend can be explained, but not its value. The adsorbate overlayer for 2 L is, however, quite different from the adsorbate overlayer for 4 L in terms of the structure (see Section 4.2). For a 2 L exposure the relative coverage of ≈0.33 ML was assigned, and this coverage corresponds to a $\left(\sqrt{3}\times\sqrt{3}\right)R\,30^{\circ}$ structure (shown by LEED and RAIRS [1, 10–11]) where ^{13}CO can occupy only three-fold hollow sites. A 4 L exposure corresponds to ≈0.6 ML and ^{13}CO can occupy both three-fold hollow and bridge sites, with various overlayer structures proposed [3]. This difference in the structure does not influence the power exponent *b*, but the prefactor *a* is 7.5 times lower for 2 L than 4 L exposure. Clearly the prefactor *b* changes more rapidly than the

coverage, and perhaps this is due to the population of different types of sites (bridge and three-fold hollow) for these two exposures. The desorption energy of CO in bridge sites is lower (176 kJ mol^{-1}) [7] than the desorption energy of CO in three-fold hollow sites (192 kJ mol^{-1}) [7], therefore the bridge sites could be more photoactive. Hence, the fs-LID is more efficient for 4 L CO exposure where three-fold hollow and bridge sites are populated than for 2 L CO exposure where only three-fold hollow sites are populated. The different photoactivity of the overlayer structure explains the trend in the prefactor, but does not explain the big decrease in its value between 4 and 2 L exposure.

From close inspection of Figure 4.11, it can be seen that the power law does not fit the data properly at low fluences. This finding is consistent with Ho *et al.* [42] and Morgenstern *et al.* [43]. They suggested a linear behaviour at low fluences due to the DIET mechanism. Hence, they used two fitting functions to describe their data, a linear function for DIET at low fluences and a power function for the DIMET mechanism at high fluence. Other authors such as Szymanski *et al.* [32] observed the existence of a fluence threshold, which is similar to the work in this thesis where there is no photodesorption signal until a certain fluence is reached. The fluence threshold for CO/Pd(111) was 11 mJ cm^{-2} in Szymanski work, [32] while in this thesis it is approximately 15 mJ cm^{-2}. Szymanski *et al.* [32] did not discuss the existence of the fluence threshold. In this thesis, a modified power function is fitted to the data. The fitting function is $Y_{FS} = a\left(F - F_0\right)^b$. This fitting function fits the data across the whole fluence regime. F_0 is the fluence threshold, or the minimum fluence necessary to cause photodesorption. F_0 is probably connected with the coupling of the molecule surface vibration to the electronic excitations of the substrate. A lower value of F_0 means that a lower electronic temperature of the substrate is required to cause desorption of the adsorbed molecules. From Figure 4.11 it can be seen that F_0, for all three exposures of ^{13}CO, is the same and is around 15 mJ cm^{-2}. Fitting curves for all 3 exposures using the new power function are shown in Figure 4.12, and the parameters for all fits, *a* and *b* are presented in Table 4.4.

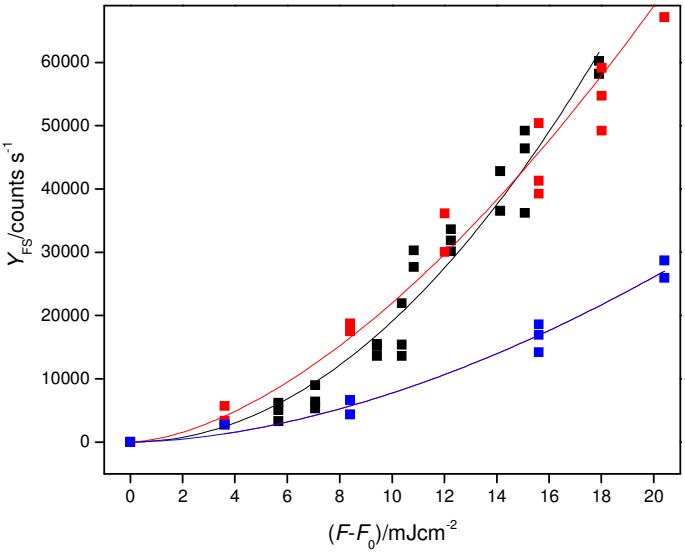

Figure 4.12 Yield-*vs*-fluence dependence curves with the fluence corrected for fluence threshold, F_0 for ^{13}CO on Pd(111) at 340 K. ■ represents data for a 10 L exposure, ■ represents data for a 4 L exposure and ■ represents data for a 2 L exposure. Solid lines are power fits ($Y_{FS} = a\left(F - F_0\right)F^b$) to the data: ─ 10 L, ─ 4 L, ─ 2 L.

Table 4.4 Parameters a and b obtained from the power fit, $Y_{FS} = a\left(F - F_0\right)^b$ for ^{13}CO on Pd(111) at T = 340 K. R^2 values provide the information about goodness of fit.

10 L ^{13}CO	$a = 190 \pm 60$ $b = 2.0 \pm 0.1$	$R^2 = 0.947$
4 L ^{13}CO	$a = 500 \pm 300$ $b = 1.7 \pm 0.2$	$R^2 = 0.947$
2 L ^{13}CO	$a = 140 \pm 70$ $b = 1.8 \pm 0.2$	$R^2 = 0.970$

Comparing the coefficients of determination, R^2 shown in tables 4.3 and 4.4 it can be observed that the modified power fit and the standard power fit are equally good to describe the data. However, the modified power fit takes into the account the existence of the fluence threshold, while the standard power fit neglects it. The power exponents

are now considerably lower compared to the power exponents from the power fit uncorrected for the fluence threshold. For all three exposures of ^{13}CO they are the same within the error, $b = 1.8 \pm 0.2$. In this case, the value of the prefactor a also does not change within the error. Unfortunately, the error in the prefactor a is the same order of magnitude as the actual value of the prefactor, hence it is very difficult to quantify changes precisely. Therefore, in order to more clearly see any trends in the prefactor, the fitting was performed with the exponent fixed at a value of 2.0 for all three exposures. Values of the prefactor a obtained from this new fit are shown in Table 4.5.

Table 4.5 Parameter a obtained from the power fit, $Y_{FS} = a(F - F_0)^b$, b = 2.0 for ^{13}CO on Pd(111) at T = 340 K. R^2 values provide the information about goodness of fit.

10 L ^{13}CO	$a = 192 \pm 5$	$R^2 = 0.949$
4 L ^{13}CO	$a = 180 \pm 6$	$R^2 = 0.940$
2 L ^{13}CO	$a = 67 \pm 2$	$R^2 = 0.973$

From Table 4.5 it can be noted that the same trend in the prefactors for decreasing exposures is observed as for the power fit uncorrected for fluence threshold (Table 4.3). Since the error of the fit is now considerably lower, changes in the prefactor a can be discussed. The prefactors for 10 and 4 L exposure are almost the same within experimental error, and the prefactor for 2 L exposure is almost three times smaller than for 10 L exposure. Using this new fitting procedure makes the interpretation of the change in prefactor easier. The small difference in the prefactor for 4 and 10 L exposure agrees well with the similar overlayer structure (similar population of bridge and three-fold hollow sites) and coverage. Between 4 and 2 L exposure the change in the prefactor is slightly higher than the change in coverage, and this agrees well with the slightly different overlayer structure. As was discussed before in this Section, for 4 L exposure bridge sites become populated, and they are expected to be more photoactive [7].

4.6.2 Laser-induced desorption of NO on Pd(111)

NO desorption was studied for 3 different exposures of Pd(111) at 340 K. Yield–*vs*-fluence dependence curves were obtained using the same procedure as before (Section 4.5) and they are shown in Figure 4.13.

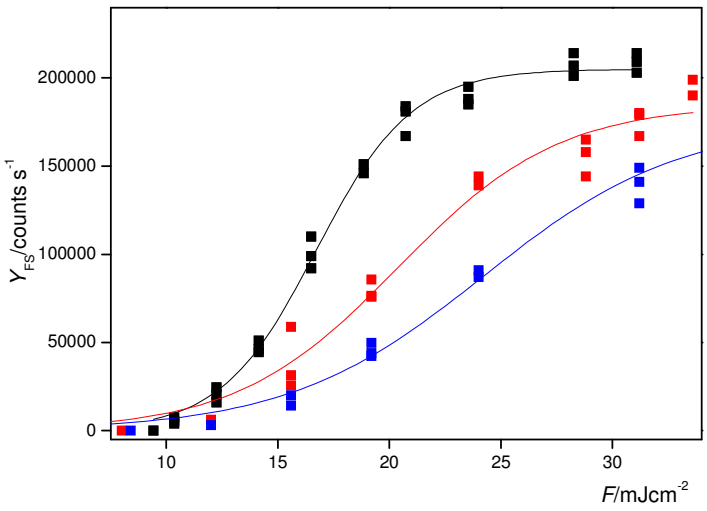

Figure 4.13 Yield-*vs*-fluence dependance curves obtained for 3 different exposures of NO on Pd(111) at 340 K. ■ represents data for a 10 L exposure, ■ represents data for a 4 L exposure and ■ represents data for a 2 L exposure. The solid lines represent a sigmoidal fit to the data: ─ 10 L, ─ 4 L, ─ 2 L.

It is obvious from Figure 4.13, that the power fit procedure will be more complex than for ^{13}CO (Figure 4.11). Even though the same fluence range was used as in the ^{13}CO experiments ($0 < F/(\text{mJ cm}^{-2}) < 35$), the NO molecules clearly desorb more readily from the surface than ^{13}CO molecules. This behaviour can be better understood if the molecular orbitals of NO are considered. The NO molecule has one more electron than the ^{13}CO molecule, and this extra electron is situated in an antibonding molecular orbital. NO bonding on metal surfaces is defined by amphoteric behaviour, hence it can either accept an electron from the surface, to fill the partially filled antibonding orbital, or donate an electron from this orbital to the substrate. For this reason, the NO molecule is expected to be more photoactive, and to photodesorb and photodissociate more easily than CO. From Figure 4.13, it can be observed that for all three NO exposures, yield-*vs*-fluence curves are sigmoidal, so saturation regime for NO is reached. It is known that for high fluences, saturation effects cause a deviation from power-law behaviour, and

there is a levelling-off in the first shot yield with increasing laser fluence [14]. This was observed, for example, in the highly efficient recombinative desorption of hydrogen from Ru(0001) [44]; however, it is the first time that such sigmoidal behaviour has been observed for a metal adsorbate system.

S-logistic curves can be fitted for both the 4 L and 10 L NO exposures. From the s-logistic curves, the saturation fluence can be calculated, and the results are presented in Table 4.6. An s-logistic curve could not be fitted to the 2 L NO data because there are not enough points around the saturation fluence.

Table 4.6 Saturation fluences calculated for systems shown in Figure 4.13. R^2 values provide the information about goodness of fit.

Adsorbate system	F_{sat}/ mJ cm^{-2}	R^2
2 L NO	–	–
4 L NO	59	0.978
10 L NO	41	0.994

From Table 4.6, it is apparent that decreased NO exposure corresponds to an increase in the value of the saturation fluence. This agrees well with the observation that the desorption activation energy decreases with increasing coverage for NO/Pd(111) [45]. For the system with the highest coverage (10 L NO), the lowest desorption activation energy is expected and hence the highest desorption yield. No saturation effects were observed for the ^{13}CO molecules in the fluence range of experiments in this thesis (Figure 4.11). This finding is consistent with the higher desorption yield for NO than CO in the fluence range studied and lower fluence threshold for NO ($F_0 \approx 9$ mJ cm^{-2}) than for CO ($F_0 \approx 15$ mJ cm^{-2}). These fs-LID experiments suggest that NO molecules are more photoactive than CO molecules on Pd(111), which is the opposite of what is observed in TPD experiments. This interesting finding will be discussed later in this section, when the results of fs-LID experiments for NO and CO will be compared. Fitting the sigmoidal curves presented in Figure 4.13 does not provide equivalent parameters to the power fit, so a subset of the data, that can be fitted to a power law, is selected. First, the s-logistic curve was fitted to the data using the least squares method. From the fitting curve, the inflection point can then be determined

easily. Only fluences before the inflection point were used for the power fits. Yield-*vs*-fluence curves were determined in this way for the three exposures of NO and are presented in Figure 4.14.

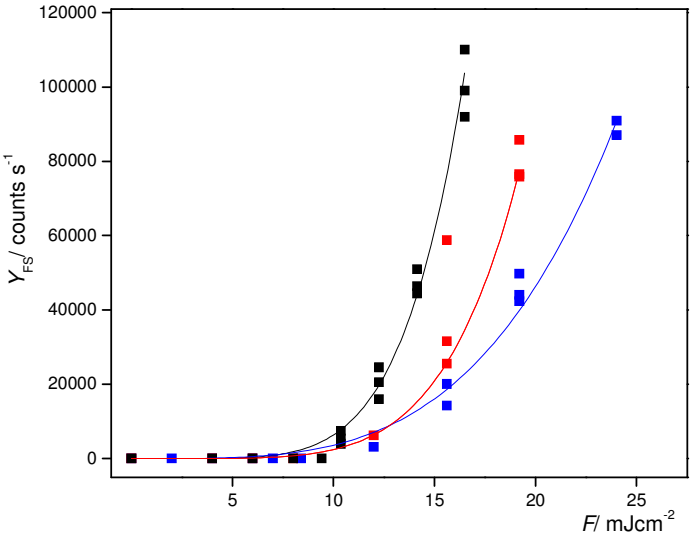

Figure 4.14 Final yield-*vs*-fluence dependence curves shown for 3 different exposures of NO on Pd(111) at 340 K: ■ 10 L, ■ 4 L and ■ 2 L. Solid lines represent power fits ($Y_{FS} = aF^b$) to the data: ─ 10 L, ─ 4 L, ─ 2 L.

Parameters a and b obtained from the yield-*vs*-fluence dependence curves, both by a linear fit ($\ln Y_{FS} = \ln a + b \ln F$) and a power fit ($Y_{FS} = aF^b$) are presented in Table 4.7.

Table 4.7 Parameters a and b obtained by a linear fit, $\ln Y_{FS} = \ln a + b \ln F$ or by a power fit, $Y_{FS} = aF^b$ for different exposures of NO on Pd(111) at 340 K. R^2 values provide the information about goodness of fit.

10 L NO	$Y_{\mathrm{FS}} = aF^b$	$a = 0.017 \pm 0.008$	$R^2 = 0.977$
		$b = 5.6 \pm 0.2$	
	$\ln Y_{FS} = \ln a + b \ln F$	$a = 0.022 \pm 0.008$	$R^2 = 0.990$
		$b = 5.5 \pm 0.2$	
4 L NO	$Y_{\mathrm{FS}} = aF^b$	$a = 0.012 \pm 0.009$	$R^2 = 0.995$
		$b = 5.3 \pm 0.2$	
	$\ln Y_{FS} = \ln a + b \ln F$	$a = 0.018 \pm 0.018$	$R^2 = 0.961$
		$b = 5.1 \pm 0.4$	
2 L NO	$Y_{\mathrm{FS}} = aF^b$	$a = 0.8 \pm 0.5$	$R^2 = 0.991$
		$b = 3.7 \pm 0.2$	
	$\ln Y_{FS} = \ln a + b \ln F$	$a = 2.2 \pm 1.6$	$R^2 = 0.967$
		$b = 3.3 \pm 0.2$	

From the table, it can be seen that the power exponent, b for 4 and 10 L NO is the same and the only slight difference is in the prefactor, a. The same findings are observed by both methods – either by the linear fit $\left(\ln Y_{FS} = \ln a + b \ln F\right)$ or by the power fit $\left(Y_{\mathrm{FS}} = aF^b\right)$.

This finding is completely consistent with the TPD and RAIRS data that are very similar for these two exposures (Section 4.3/Figure 4.5 and Figure 4.6). From the RAIRS data it can be seen that the intensity and position of the two IR bands (at $\approx 1652\,\mathrm{cm}^{-1}$ and $1792\,\mathrm{cm}^{-1}$) are almost the same for these two exposures, with the intensity being only slightly lower for an NO exposure of 4 L.

From the NO calibration curve (Figure 4.6), the surface coverage is slightly lower for 4 L NO ($\approx 10\%$) than for 10 L NO. From Table 4.2 it can be observed that the relative yields of mass 28 (N_2) and mass 44 (N_2O) with respect to mass 30 are the same for both exposures. Both of these findings support the fact that there is similar photodesorption behaviour of NO following 4 and 10 L exposure. For the exposure of 2 L the power exponent changes from 5.5 to 3.7 suggesting that there is a significant change in

structure between those two coverages that makes the fs-LID more difficult for the lower exposure.

The TPD and RAIR spectra for a 2 L exposure of NO are different from the TPD and RAIR spectra for 4 and 10 L NO exposures. In the RAIR spectra for a 2 L exposure (Figure 4.5) an additional band for CO adsorbed on a three-hollow site can be observed and CO adsorption is also seen in the TPD experiments (Figure 4.6). The influence of CO on NO photodesorption is negligible as was explained in Section 4.4 b, since only ~5% of Pd(111) is contaminated with CO from the background gas in the UHV chamber. The only real difference in the TPD spectra for 2 L NO exposure is in the higher relative yields of mass 28 (CO and N_2 together) and mass 44 (CO_2 and N_2O together) than for 4 L and 10 L exposure. It is known that at lower coverages, the degree of dissociation is usually higher [39]. The decrease in the power exponent, that results in the curve that is less steep for 2 L compared to 4 L and 10 L NO exposure, may be due to the contamination of the surface with atomic N and O.

The saturation coverage at room temperature for NO adsorption on Pd(111) is about 0.5 ML, so the coverage for 2 L NO should be approximately 0.25 ML. For that structure it is well known that there is no long range order. Repulsions between NO molecules are probably smaller at lower coverage, making the desorption more difficult. For example, in a detailed study of the thermal behaviour of NO on Pd surfaces, the activation energies as a function of coverage were calculated by threshold temperature programmed desorption [45]. It was observed that the desorption activation energy decreased rapidly from 180 kJ mol^{-1} (for ≈0.03 ML) to 90 kJ mol^{-1} (for 0.34 ML) for NO on Pd(111). This big decrease in the activation energy suggests that the assumption about increasing repulsion between NO molecules with increasing coverage is correct. The decrease in the power exponent for 2 L NO, with respect to 4 L and 10 L exposure, makes the interpretation of the yield-*vs*-fluence curve for this exposure more difficult. The yield-*vs*-fluence dependence curve for 2 L NO can be divided into two regions. In the low fluence region, the prefactor has more influence on the desorption, therefore at lower fluences the desorption yield will be larger for 2 L than for 4 or 10 L NO exposure. At higher fluences, the exponent has more influence on the desorption yield, so the overall desorption yield decreases with decreasing coverage. In the ^{13}CO case there is only one type of behaviour in the whole fluence range, and that is a decrease in the desorption yield with decreasing exposure.

As with the ^{13}CO photodesorption experiments, a modified power fit was also used to fit the yield-*vs*-fluence curves with the fluence corrected for a fluence threshold (defined in a Section 4.1) in the NO photodesorption experiments. The power fit curves for the fluence corrected for F_0, ≈9 mJ cm^{-2} can be seen in Figure 4.15.

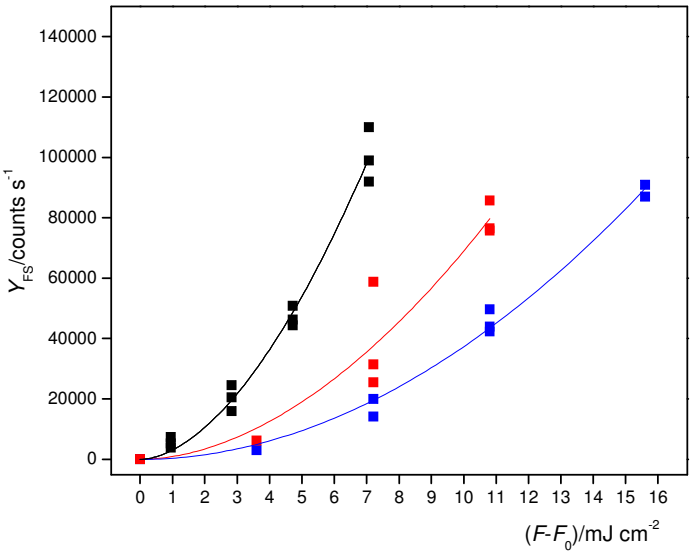

Figure 4.15 The yield-*vs*-fluence dependence curves with the fluence corrected for fluence threshold, F_0, for NO on Pd(111) at T = 340 K. ■ represents data for a 10 L exposure, ■ represents data for a 4 L exposure and ■ represents data for a 2 L exposure. Solid lines represent fits to the data: ─ 10 L, ─ 4 L, ─ 2 L.

The coefficients for the yield-*vs*-fluence dependence curves with the fluence corrected for F_0, are shown in Table 4.8.

Table 4.8 Parameters a and b obtained from the power fit $Y_{FS} = a(F - F_0)^b$, for NO on Pd(111) at T = 340 K. The value of the coefficient of determination, R^2 is also provided.

10 L NO	$a = 3100 \pm 700$ $b = 1.8 \pm 0.1$	$R^2 = 0.984$
4 L NO	$a = 900 \pm 900$ $b = 1.9 \pm 0.4$	$R^2 = 0.895$
2 L NO	$a = 400 \pm 100$ $b = 2.0 \pm 0.1$	$R^2 = 0.990$

As with the ^{13}CO experiments, the power exponent b, was then held constant, at 1.8, in order to compare the variation in the prefactor with exposure. The prefactors obtained by the power fit with the fluence corrected for F_0 and b = 1.8 are shown in Table 4.9.

Table 4.9 Parameter a obtained from the power fit, $Y_{FS} = a(F - F_0)^b$, b = 1.8 for NO on Pd(111) at T = 340 K. The value of the coefficient of determination, R^2 is also provided.

10 L NO	$a = 2960 \pm 71$	$R^2 = 0.976$
4 L NO	$a = 1090 \pm 72$	$R^2 = 0.910$
2 L NO	$a = 620 \pm 16$	$R^2 = 0.987$

The coefficients of determination, R^2 obtained for the standard power fit or the modified power fit in NO photodesorption experiments show that the data could be described equally well using the standard power fit or the modified power fit. The change in the coefficients with the coverage/exposure has an interesting trend that is difficult to link with the trend in the standard power fit. In contrast with the ^{13}CO experiments, the prefactor a, changes a lot with NO coverage. When the exposure is changed from 10 L to 4 L NO, the prefactor a, changes from 2960 to 1090, so it decreases by a factor of almost three. This cannot be explained either by a change in the overlayer structure or by coverage, since both of them are very similar for these exposures. Data in Table 4.8 reveal that the biggest error in the power exponent b is for 4 L NO exposure, 1.9 ± 0.4. Therefore, holding the power exponent b constant is less justified for 4 L NO than for

other two NO exposures. The value of the prefactor at 2 L exposure is ≈20% of the value for 10 L NO exposure and that cannot be explained by the change in coverage, because the coverage for a 2 L exposure is 40% of the coverage for a 10 L NO exposure. This change in the prefactor might be related to the different overlayer structure as was the case for CO. A 2 L exposure corresponds to a structure that has short range order, whereas the structure for 10 L exposure has long range order, as discussed in Section 4.2. This probably means, that the entropy change upon desorption will be higher for 10 L NO exposure, accounting for the higher desoption yield.

If the results for NO are compared with the results for ^{13}CO then the following differences in the power law behaviour can be observed:

1 The threshold fluence in the femtosecond laser-induced desorption experiments is higher for ^{13}CO ($F_0 \approx 15$ mJ cm^{-2}) than for NO adsorbed on Pd(111) ($F_0 \approx 9$ mJ cm^{-2}). The fluence threshold was defined earlier as the minimum fluence necessary to cause photodesorption. The fluence threshold was determined from the yield-*vs*-fluence dependence curves shown in Figure 4.11 and Figure 4.14. It is difficult to determine the threshold exactly, since the quality of the biexponential fit (used to determine Y_{FS}) at lower fluences, is worse than that for the higher fluences. However, even though the fluence threshold was not very accurate, it is clear that the fluence threshold for NO is lower than for ^{13}CO.

If the TPD desorption curves for mass 29 (^{13}CO) and mass 30 (NO) are compared, it can be observed that ^{13}CO desorbs at a lower temperature (T = 530 K) than NO (T = 560 K). As a first approximation in calculating the desorption energies (E_{des}), the Redhead equation [35] can be used (Equation 2.12, Section 2.8, Chapter 2). The desorption energy for NO is estimated to be 156 kJ mol^{-1} (Section 4.4.2) and for CO it is 147 kJ mol^{-1} (Section 4.4.1). This has also been predicted theoretically [46], but there is still a lack of direct experimental evidence. This trend contradicts that observed for fs-LID. The higher photoreactivity of NO can be explained by both the DIMET model and the friction model.

In the DIMET model, the fluence threshold would have to be associated with either the lifetime on the excited potential energy surface (PES) or with the energy difference between the ground and excited PES, as shown in equations 1.12 and 1.13 that model the excitation and deexcitation rate. Both NO and CO

are small chemisorbed species that are expected to have similar excited electronic states lifetimes. However, the energy gain in one cycle will also depend on the energy difference between the ground and excited PESs. Larger energy differences between the ground and excited PESs results in larger deexcitation and smaller excitation rates (Equations 1.12 and 1.13). It was explained in the Introduction (Section 1.6) that the energy difference between the Fermi level and the $2\pi^*$ orbital is larger for CO adsorbed on Pd(111). Therefore, the DIMET model justifies the larger fluence threshold for CO compared to NO. In the friction model, larger η_e results in a higher desorption yield, and a lower fluence threshold. This is clearer if the probability for desorption is calculated using the modified electronic friction model developed by Brandbyge and co-workers [16], Equation 1.12 (Introduction, Section 1.7). The friction coefficients can be understood as inverse energy relaxation times of the corresponding adsorbate-substrate vibrational mode [29]. Some of the modes that may play a role for desorption have a shorter vibrational lifetime (larger η_e) for NO on Pt(111) than for CO on Pt(111) [47].

2 The overall appearance of the yield-*vs*-fluence curves for femtosecond laser-induced desorption of ^{13}CO is quite different from the appearance of the curves for NO. The NO curves (Figure 4.13) are sigmoidal, with saturation fluence being lower for 10 L than 4 L NO exposure, as shown in Table 4.6. The ^{13}CO curves can be described by a power law for the whole fluence range studied, because there is no saturation of the photodesorption yield. NO seems to be more photoactive than CO, which is apparent from the lower fluence threshold for desorption, which explains why NO will completely desorb at lower fluences than CO. The reason for this behaviour can be explained in terms of the different molecular orbital occupations of NO and CO, i. e., the additional electron in the anti-bonding orbital of the NO molecule.

3 The overlayer structure of CO and NO on Pd(111) surfaces is quite similar [3]. The saturation coverage at room temperature for CO on Pd(111) is ≈ 0.6 ML (for 10 L exposure) and for NO on Pd(111) is 0.5 ML (for 10 L exposure). From the calibration curves for ^{13}CO and NO shown in figures 4.4 and 4.7, it can be

calculated that the integrated TPD area for 4 L ^{13}CO is about 83% of the integrated area for 10 L ^{13}CO which corresponds to a coverage ≈ 0.5 ML. For NO, the integrated area under the TPD curve for 4 L is about 90% of the area under the TPD curve for a 10 L exposure, which corresponds to a coverage of 0.45 ML. Therefore, the coverages for a 4 L exposure of both molecules are reasonably similar. When the exposure is changed from 10 L to 4 L, the yield-*vs*-fluence curves for CO and NO show similar behaviour: the power exponent, *b* remains the same and the prefactor *a* changes. However, when the exposure is changed from 4 to 2 L, the coverage for the NO molecule changes (≈0.2 ML) compared to the coverage for the CO molecule (≈0.33 ML). The power fit curve in the CO case again has the same power exponent *b*, and the prefactor *a*, changes a little. In the case of NO the power exponent changes from 5.5 to 3.7. In a paper published by Ramsier *et al.* [45], the kinetic parameters for NO adsorption on Pd(111) at room temperature were determined from TPD. The desorption activation energy change for a change in surface coverage between ~0.2 ML (2 L exposure) and ~0.35 ML (a little bit less than 4 L) was ~ 60 kJ mol^{-1}. In a paper published by Ertl *et al.* [48] the activation energy for desorption of CO on Pd(111) between 0.33 ML (2 L exposure) and 0.5 ML (4 L exposure) changes by ~ 46 kJ mol^{-1}. Hence, it can be seen that the activation energy for desorption between 2 and 4 L exposure changes with exposure more rapidly for NO than for CO. This large change in the desorption activation energy, together with the short range structure for 2 L exposure, are probably reasons for the observed change in power exponent.

4.7 Summary

Two well-known adsorbate-substrate systems, NO/Pd(111) and CO/Pd(111) were studied using classic surface science techniques: RAIRS and TPD in order to test the newly assembled apparatus and to enable comparison with co-adsorbed CO and NO (Chapter 5). The desorption energies for NO and CO on Pd(111) were estimated to be 156 kJ mol^{-1} and 147 kJ mol^{-1}, respectively using the Redhead equation for first order desorption.

Femtosecond laser-induced first shot desorption yields (Y_{FS}) have been measured as a function of laser fluence (F) for exposures of 2, 4 and 10 L of ^{13}CO. The data obtained have been fitted to a power law of the form $Y_{FS} = aF^b$ with the exponents, b = 3.8 ± 0.1, 3.5 ± 0.1 and 3.6 ± 0.2, respectively. It was found that a standard power law function was not appropriate to describe data in the low fluence region; hence, the experimental data were also fitted with a modified power law function, $Y_{FS} = a(F - F_0)^b$, where F_0 is the fluence threshold, below which a photodesorption signal cannot be observed. F_0 is ~15 mJ cm^{-2} and the retrieved exponents are: b = 1.7 ± 0.2, 1.7 ± 0.2 and 2.0 ± 0.1, for the different exposures respectively.

Femtosecond laser-induced desorption experiments were also performed for NO exposures of 2, 4 and 10 L. The data obtained were also fitted to a power law with the exponents, b = 3.7 ± 0.2, 5.3 ± 0.2, and 5.6 ± 0.1, respectively. These data were also fitted with the same modified power law function as for ^{13}CO, with the exponents, b = 2.0 ± 0.1, 1.9 ± 0.4 and 1.8 ± 0.1, and F_0 ~10 mJ cm^{-2}. Even though the NO photodesorption experiments were performed for the same fluence range as for CO/Pd(111), the data show dramatically different behaviour. For NO, the signal did not change with fluence once a certain maximum fluence was reached, *i.e.* the signal became saturated. For CO, no saturation effects were observed. The different photodesorption behaviours of these two adsorbates can be explained qualitatively either using the DIMET model or the friction model. In both models, the explanation is based on the shorter vibrational lifetime (larger η_e) for NO on Pd(111) than for CO on Pd(111).

4.8 References

1. A. M. Bradshaw and H. M. Hoffman, *Surface Science*, **72** (3), 513 (1978).
2. W. A. Brown and D. A. King, *Journal of Physical Chemistry B*, **104** (47), 11440 (2000).
3. E. Ozensoy, C. Hess and D. W. Goodman, *Topics in Catalysis*, **28** (1-4), 13 (2004).
4. S. G. Sugai, H. Watanabe, T. Kioka, H. Miki and K. Kawasaki, *Surface Science*, **259** (1-2), 109 (1991).
5. I. Stara and V. Matolin, *Surface Science*, **313** (1-2), 99 (1994).

6. J. Cortes and E. Valencia, *Chemical Physics Letters*, **463** (1-3), 251 (2008).
7. K. Honkala, P.Pirila and K. Laasonen, *Surface Science*, **489** (1-3), 72 (2001).
8. D. Loffreda, D. Simon and P. Sautet, *Journal of Catalysis*, **213** (2), 211 (2003).
9. M. K. Rose, T. Mitsui, J. Dunphi, A. Borg, D. F. Ogletree, M. Salmeron and P. Sautet, *Surface Science*, **512** (1-2), 48 (2002).
10. W. K. Kuhn, J. Szanyi and D. W. Goodman, *Surface Science*, **274** (3), L611 (1992).
11. F. M. Hoffmann, *Surf. Sci. Rep.*, **3**, 107 (1983).
12. K. H. Hansen, Z. Sljivancanin and B. Hammer, *Surface Science*, **496** (1-2), 1 (2002).
13. I. Nakamura, T. Fujitani and H. Hamada, *Surface Science*, **514** (1-3), 409 (2002).
14. C. Frischkorn and M. Wolf, *Chemical Reviews*, **106** (10), 4207 (2006).
15. P. Saalfrank, *Chemical Reviews*, **106** (10), 4116 (2006).
16. M. Brandbyge, P. Hedegard, T. F. Heinz, J. A. Misewich and D. M. Newns, *Physical Review B*, **52** (8), 6042 (1995).
17. F. J. Kao, D. G. Busch, D. Cohen, D. G. Dacosta and W. Ho, *Physical Review Letters*, **71** (13), 2094 (1993).
18. S. W. Gao, D. G. Busch and W. Ho, *Surface Science*, **344** (3), L1252 (1995).
19. F. Budde, T. F. Heinz, A. Kalamarides, M. M. T. Loy and J. A. Misewich, *Surface Science*, **283** (1-3), 143 (1993).
20. L. M. Struck, L. J. Richter, S. A. Buntin *et al.*, *Physical Review Letters*, **77** (22), 4576 (1996).
21. M. Bonn, S. Funk, C. Hess, D. N. Denzler, C. Stampfl, M. Scheffler, M. Wolf and G. Ertl, *Science*, **285** (5430), 1042 (1999).
22. T. Yamanaka, A. Hellman, S. W. Gao and W. Ho, *Surface Science*, **514** (1-3), 404 (2002).
23. F. Budde, T. F. Heinz, M. M. T. Loy, J. A. Misewich. F. Derougemont and H. Zacharias, *Physical Review Letters*, **66** (23), 3024 (1991).
24. J. A. Prybyla, T. F. Heinz, J. A. Misewich, M. M. T. Loy and J. H. Glownia, *Physical Review Letters*, **64** (13), 1537 (1990).
25. T. H. Her, R. J. Finlay, C. Wu and E. Mazur, *Journal of Chemical Physics*, **108** (20), 8595 (1998).
26. S. Deliwala, S. Frischkorn, M. Wolf, T. H. Her, W. D. Mieher and E. Mazur, *Chemical Physics Letters*, **242** (6), 617 (1995).

27. J. A. Misewich, A. Kalamrides, T. F. Heinz, U. Hofer and M. M. T. Loy, *Journal of Chemical Physics*, **100** (1), 736 (1994).
28. J. A. Misewich, S. Nakabayashi, P. Weigand, M. Wolf and T. F. Heinz, *Surface Science*, **363** (1-3), 204 (1996).
29. S. Funk, M. Bonn, D. M. Denzler, C. Hess, M. Wolf and G. Ertl, *Journal of Chemical Physics*, **112** (22), 9888 (2000).
30. J. A. Prybyla, H. W. K. Tom and G. D. Aumiller, *Physical Review Letters*, **68** (4), 503 (1992).
31. E. H. G. Backus, A. Eichler, A. W. Klein and M. Bonn, *Science*, **310** (5755), 1790 (2005).
32. P. Szymanski, A. L. Harris and N. Camillone, *Journal of Physical Chemistry A*, **111** (49), 12524 (2007).
33. R. Raval, M. A. Harrison and D. A. King., *Surface Science*, **211** (1-3), 61 (1989).
34. X. C. Guo and J. T. Yates, *Journal of Chemical Physics*, **90** (11), 6761 (1989).
35. P. A. Redhead, *Vacuum*, **12**, 203 (1962).
36. D. Loffreda, D. Simon and P. Sautet, *Chemical Physics Letters*, **291** (1-2), 15 (1998).
37. X. P. Xu, P. J. Chen and D. W. Goodman, *Journal of Physical Chemistry*, **98** (37), 9242 (1994).
38. D. R. Rainer, S. M. Vesecky, M. Koranne, W. S. Oh and D. W. Goodman, *Journal of Catalysis*, **167** (1), 234 (1997).
39. R. D. Ramsier, Q. Gao, H. N. Waltenburg and J. T. Yates, *Journal of Chemical Physics*, **100** (9), 6837 (1994).
40. J. W. Gadzuk, *Chemical Physics*, **251** (1-3), 87 (2000).
41. P. Salfrank, *Private Communications*.
42. W. Ho, *Surface Science*, **363** (1-3), 166 (1996).
43. M. Mehlhorn, H. Gawronski and K. Morgenstern, *Physical Review Letters*, **104** (7), 076101 (2010).
44. D. N. Denzler, C. Frischkorn, M. Wolf and G. Ertl, *Journal of Physical Chemistry B*, **108** (38), 14503 (2004).
45. R. D. Ramsier, Q. Gao, H. N. Waltenburg, K. W. Lee, O. W. Nooij, L. Lefferts and J. T. Yates, *Surface Science*, **320** (3), 209 (1994).

46. M. Gajdos, J. Hafner and A. Eichler, *Journal of Physics-Condensed Matter*, **18** (1), 13 (2006).
47. V. Krishna and C. J. Tully, *Journal of Chemical Physics*, **125** (7), 054706 (2006).
48. G. Ertl, *Pure and Applied Chemistry*, **61** (6), 1001 (1989).

CHAPTER 5

FEMTOSECOND LASER STUDIES OF CO/NO AND OF NO/CO ON Pd(111)

5.1 Introduction

This chapter describes femtosecond laser-induced desorption (fs-LID) and femtosecond laser-induced reaction (fs-LIR) of CO and NO, sequentially dosed on a Pd(111) surface. Four different co-adsorbed systems: (2, 4 L) ^{13}CO/2 L NO and (2, 4 L) NO/2 L ^{13}CO are investigated. The results obtained from these experiments are analysed together with measurements obtained from standard surface science techniques: temperature programmed desorption (TPD) and reflection absorption infrared spectroscopy (RAIRS).

The mechanism of fs-LID is different from the mechanism of thermally induced desorption. However, in some theoretical models it is possible to find a link between laser-induced reactions and thermal reactions. In this thesis, a simple qualitative model for studying fs-LID was used to calculate the ratio in the photodesorption yield for CO(NO) in co-adsorbed systems to the pure CO(NO) photodesorption yield, for the fluence, F = 18 mJ cm^{-2}. This model is based on equation that links the activation energy for desorption from TPD experiments with the photodesorption yield.

5.2 Overview

In this chapter, the reaction of interest is the CO and NO reaction on Pd(111). This reaction has been studied over a variety of transition and noble metal catalysts. [1–10] In the late 1970s, the three way catalytic converter was introduced into the emission control systems of car exhausts in the United States. The three way catalytic converter simultaneously catalyses three reactions: the reduction of NO_x species, the oxidation of CO and the oxidation of excess hydrocarbons. In order to choose the cheapest and best catalyst it is important to understand the fundamental reaction pathways and catalytic

characteristics. The first catalysts were made of platinum and rhodium (90% platinum and 10% rhodium). However, rhodium is expensive and a rare element. Palladium is one possible alternative to rhodium, not only because is more plentiful, but it has also been found to be more durable at higher reaction temperatures, so can be positioned nearer the engine.

The first step towards understanding reactions on real surfaces that are used in catalysis is to understand the reaction on a well-defined single-crystal surface that is prepared and investigated using ultrahigh vacuum (UHV) techniques and a range of classic surface science techniques. In Chapter 4, the adsorption of CO and NO on Pd(111) was studied by RAIRS, TPD and fs-LID. The intention in this chapter, is to compare the results obtained for these pure systems with the results for CO/NO mixtures on Pd(111).

Pure CO and NO on Pd(111) have been studied using a wide range of experimental and theoretical techniques [11–18], but there are relatively few RAIRS studies of co-adsorbed CO and NO on Pd(111) and just one TPD study of co-adsorbed CO and NO. The co-adsorption of a CO/NO gas mixture on Pd(111) has been studied using RAIRS over a wide range of temperatures and pressures [17, 19–21]. Xu *et al.* [19] used RAIRS to investigate a Pd(111) surface on exposure to an equimolar CO/NO mixture for temperatures in the range of 150-500 K at a total pressure of 10^{-6} Torr. The adsorption of CO and NO produces infrared bands at 1550, 1750, 1900, and 2070 cm^{-1}. The first two bands are associated with the adsorption of NO and the other two are associated with the adsorption of CO. The 1550 cm^{-1} band, observed at temperatures above 300 K, is attributed to nitric oxide adsorption on the 3-fold hollow sites of Pd(111). The 1750 cm^{-1} band, which is observed at temperatures below 300 K, is assigned to NO adsorption on the atop Pd(111) sites. These assignments are based on a study of NO on Pd(111) with RAIRS and low energy electron diffraction (LEED) [22]. The bands at 1900 and 2070 cm^{-1} for CO/NO co-adsorption are attributed to CO adsorbed at bridge and atop sites, respectively [11, 23]. Between 400 K and 500 K, the majority of surface species corresponds to NO adsorbed at the three-fold hollow sites. The coverage of CO is much less than that of NO and also much less than the CO equilibrium coverage when only gas phase CO is present.

Polarisation modulation (PM) RAIRS experiments have also been employed to investigate co-adsorbed CO/NO mixtures on Pd(111) at pressures of up to 240 mbar

[20–21]. The RAIR spectra are significantly different at higher pressures compared to those recorded under UHV conditions, with CO being observed in three-fold hollow sites and NO in atop or three-fold hollow sites, dependant on the gas pressure. For pressures greater than 0.1 mbar, and temperatures greater than 500 K, an additional band at 2242 cm^{-1} is observed, which is assigned to the NCO species. At 240 mbar, the formation of NCO is also observed at 2255 cm^{-1}.

Only one TPD study of co-adsorbed CO and ^{15}NO is recorded in the literature [24]. These TPD experiments were conducted as a part of a larger kinetics study of the CO+NO reaction on model catalysts. These TPD experiments of Rainer *et al.* [24] were carried out at higher pressures than discussed here and only TPD of $^{15}N_2$ from the CO+NO/Pd(111) surface was presented.

It is important to mention that in the literature there are no previous fs-LID studies of CO/NO on Pd(111). The CO and NO reaction has been studied on Ir(111) by time resolved sum frequency generation (SFG).[25] The frequency of the C-O stretch for a pure CO layer adiabatically follows the temperature of the iridium surface. In a mixed CO/NO layer, the C-O frequency exhibits non-adiabatic coupling to the hot iridium electrons with a friction coefficient that depends on the electron temperature and the CO:NO ratio. Two possible scenarios emerge: NO causes a static tilt of the CO with a tilt angle depending on the relative coverage. This increases the degree of bonding of the CO $2\pi^*$ orbital to the iridium surface, which in turn increases the degree of non-adiabatic coupling. Alternatively, the C-O frequency reflects transient changes in the bonding configuration of the neighboring NO. The latter interaction could be the primary step in the direct reduction of NO by CO to form CO_2 on the surface.

It can be observed that the RAIR and TPD studies described above are for the co-adsorption of equimolar quantities of CO and NO on Pd(111). In this chapter, studies are related either to CO following NO adsorption (2 L NO) or for NO following CO adsorption (2 L CO). RAIR and TPD experiments for these systems have not been presented in the literature.

In chapter 4, a new analysis method for analysing yield-*vs*-fluence curves was presented. The experimental data was first fitted to a power law, $Y_{FS} = aF^b$ and then to a power law with a fluence corrected for fluence threshold, F_0. This new fitting function was very useful when trying to explain trends in the prefactor, a for different coverages/exposures of CO or NO. Initially, it was decided to use this new function for

explaining the trends in prefactors *b* in the co-adsorbed systems. It was assumed that the exponent *b*, would be, approximately, the same for CO (NO) in co-adsorbed systems as for pure CO (NO) and that any changes in the photodesorption yield could be related to a change in the prefactor *b*. However, this was found to be true only for CO. The prefactor *b* decreased, and *a* increased for NO in co-adsorbed systems compared to pure NO systems. The errors in the parameters *a* and *b* for both CO and NO were higher using the new method of fitting than using a standard power fit, hence all changes in the photodesorption yield will be explained using a standard power fit.

5.3 Results and discussion

RAIRS experiments were performed with ^{12}CO and NO, as discussed in Section 4.4 in the previous chapter. TPD and fs-LID experiments were performed first with ^{13}CO and NO and then with CO and ^{15}NO. The first pair of isotopes was useful to distinguish between $^{13}CO_2$ and N_2O reaction products which would have the same mass in the quadrupole mass spectrometer (QMS). Unfortunately, residual CO made the mass 44 (N_2O + CO_2) assignment difficult. The second pair of isotopes was used to distinguish between N_2O and residual CO_2 because the reaction products were $^{15}N_2O$ (mass 46) and CO_2 (mass 44). For each of the co-adsorbed systems studied, TPD experiments were performed in combination with fs-LID for F = 24 mJ cm^{-2}. These experiments helped in assigning the multiple peaks observed in TPD experiments for mass 30 ($^{15}N_2$).

TPD spectra shown in this chapter were the same, whether or not fs-LID was performed before the TPD experiments, because the fs-LID experiments were performed on only a small area of the surface (less than 1%). However, RAIRS and TPD of the co-adsorbed systems were used to show the effects on the CO or NO when the other species is co-adsorbed.

5.3.1 RAIRS and TPD characterisation of NO/CO/Pd(111)

Before presenting the results of the fs-LID experiments for co-adsorbed CO and NO on Pd(111), the results of RAIRS and TPD experiments will be described in order to characterise this surface. CO and NO were sequentially dosed onto the Pd(111) surface. The results are presented in two parts: first for a system where CO was adsorbed first,

NO/CO/Pd(111), and then for a system where NO was adsorbed first, CO/NO/Pd(111). Figure 5.1 shows RAIR spectra for increasing exposure of NO on a Pd(111) surface onto which 2 L CO was previously adsorbed.

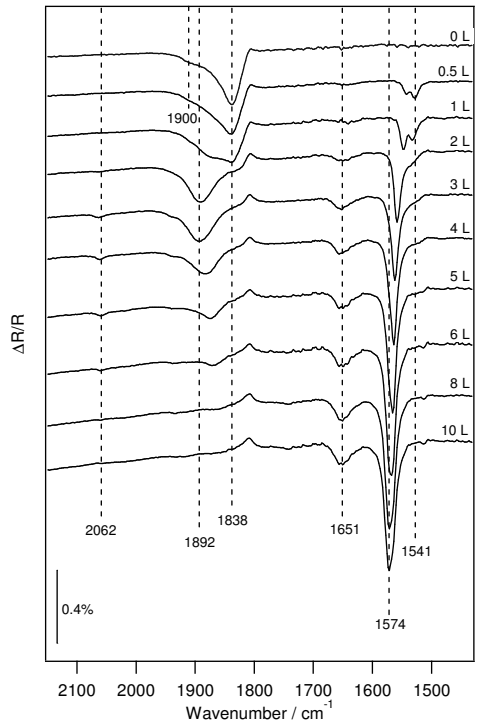

Figure 5.1 RAIR spectra for different exposures of NO on 2 L CO/Pd(111) at T = 320 K. The NO exposure is varied from 0 to 10 L.

At 2 L CO exposure, a band at 1838 cm^{-1} is observed which corresponds to CO adsorbed in three-fold hollow sites. As described in Chapter 4, this exposure corresponds to a $\left(\sqrt{3}\times\sqrt{3}\right)R30^\circ$ LEED structure, since this structure has been shown to generate a similar band at 1836 cm^{-1} in previous RAIRS studies [11]. A small shoulder at 1900 cm^{-1} can also be observed, which is assigned to CO adsorbed on defect sites. [19] With increasing NO exposure, the band assigned to CO adsorbed in three-fold hollow sites starts to broaden. The band remains at the same frequency until 2 L NO was dosed, and then it shifts to 1892 cm^{-1}, which is probably a displacement of CO to the less favourable bridge site [15]. With further NO dosing the band shifts to lower wavenumbers, and the integrated area under the peak decreases, until it disappears at 8 L NO exposure. The band assigned to CO adsorbed on an atop site, based on RAIRS and LEED [11],

appears for a 2 L NO exposure at 2062 cm^{-1} and slightly increases in intensity until it disappears after 8 L NO exposure. The area under the atop CO peak is very small, hence only a small amount of CO resides in atop sites. These RAIR spectra show clearly that CO is displaced by NO.

NO is able to force CO to initially occupy the less favoured bridge and atop sites, since the adsorption energy of NO is higher than that for CO in three-fold hollow sites (E_{ads}(CO) = −194 kJ mol^{-1}, E_{ads}(NO) = −221 kJ mol^{-1}). This statement is based on *ab initio* and Monte Carlo studies of CO and NO co-adsorption on Pd(111) [26]. The RAIR spectra in Figure 5.1 also show two NO vibrational bands with increasing NO exposure. The main vibrational band at 1541-1574 cm^{-1} is assigned to the NO stretching frequency for NO adsorbed in a three-fold hollow site, based on a room temperature RAIR study of NO/Pd(111) [27]. The band at 1651 cm^{-1} was assigned as NO adsorbed in defect sites (Chapter 4) [19]. This band remains at the same frequency for all NO exposures, but increases in intensity. RAIR spectra for 10 L NO on the surface initially dosed with 2 L CO are the same as RAIR spectra for 10 L of NO on clean Pd(111) with two bands observed at 1572 and 1652 cm^{-1} in both cases. This is further evidence that CO is displaced by the adsorption of NO. Figure 5.2 shows the integrated RAIR absorbance for CO (in the three-fold hollow site or bridge site) and NO (in the three-fold hollow site) for 2 L CO/Pd(111) as a function of increasing NO exposure.

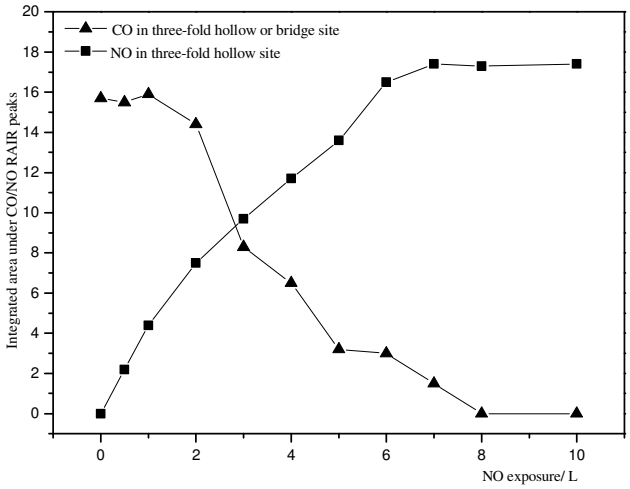

Figure 5.2 Integrated areas under RAIR peaks for CO in the three-fold hollow site and bridge site and for NO adsorbed in the three-fold hollow site as a function of NO exposure.

From Figure 5.2 it can be clearly observed that the integrated area under the peak for CO adsorbed in a three-fold hollow site gradually decreases, while the area under the peak for NO adsorbed in a three-fold hollow site gradually increases. The problem with integrated areas under RAIR peaks is that they are not always exactly proportional to the amount of species adsorbed on the surface because of ordering and dipole coupling effects, so TPD has to also be used to obtain exact information about the amount of CO and NO on the surface. Figure 5.2 shows that there is almost no change in the integrated area under the three-fold hollow CO peak until 2 L NO is dosed onto the 2 L CO/Pd(111) surface. It can also be observed that the area under the CO or NO peak is not a linear function of NO exposure.

Figure 5.3 shows a comparison of TPD spectra for two co-adsorbed systems, 4 L ^{15}NO/2 L CO/Pd(111) and 2 L ^{15}NO/2 L CO/Pd(111) with pure systems (^{13}CO or NO) of appropriate coverage. TPD spectra are shown for mass 28/mass 29 (CO/^{13}CO), mass 30 ($^{15}N_2$), mass 31/mass 30 (^{15}NO/NO), mass 44 (CO_2) and mass 46 ($^{15}N_2O$). Some of the spectra shown in Figure 5.3 are for the ^{15}NO/CO system and some are for the NO/^{13}CO system. Investigations show that TPD spectra of the isotopes (NO compared to ^{15}NO, and ^{13}CO compared to CO) in the co-adsorbed systems have the same shape and T_{max} and therefore the spectra can be compared directly. The only difference is in the integrated area under the TPD peaks that arises due to change in QMS sensitivity for the different isotopes. ^{13}CO spectra were corrected by comparison of the integrated TPD areas for 10 L ^{13}CO and 10 L CO. The integrated TPD area for 10 L ^{13}CO was 1.6 times lower than that for 10 L CO, hence all ^{13}CO TPD areas in Figure 5.3 were multiplied by 1.6. Unfortunately, TPD was not performed for pure ^{15}NO, hence the areas for ^{15}NO and NO were obtained from TPD of the co-adsorbed systems, ^{13}CO/NO or CO/^{15}NO which had the same amounts of CO and NO. All integrated areas under the NO TPD curves in Figure 5.3 were divided by 1.8. Most of the fs-LID experiments were performed with ^{13}CO/NO systems because ^{15}NO was not available at that time.

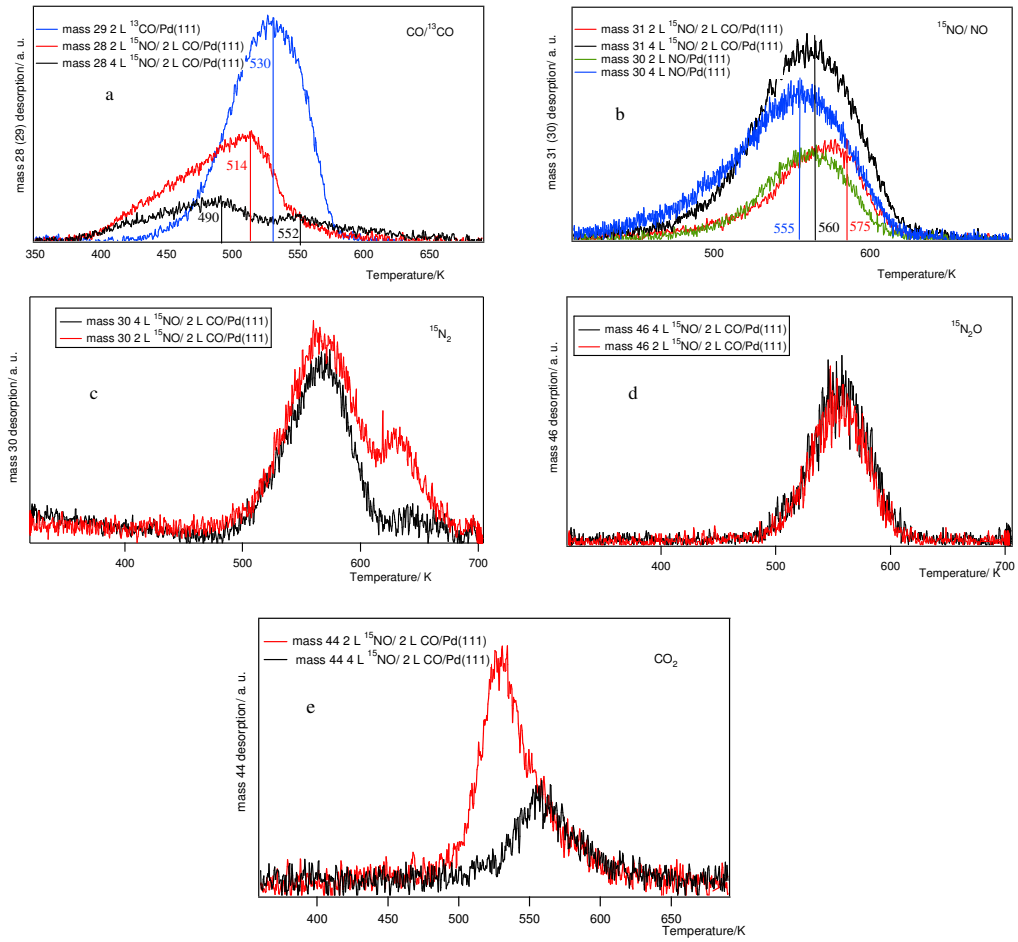

Figure 5.3 TPD spectra of a) mass 28/29 (CO/ ^{13}CO), b) mass 30/31 (NO/ ^{15}NO), c) mass 30 ($^{15}N_2$), d) mass 46 ($^{15}N_2O$) and e) mass 44 (CO_2) following ^{15}NO adsorption on 2 L CO/ Pd(111) at T = 320 K taken at 2 L and 4 L NO exposure. The 2 L ^{13}CO TPD curve is multiplied by 1.6, and the 2 L NO and 4 L NO curves are divided by 1.8 to compensate for different QMS sensitivities of the different isotopes.

Figure 5.3 needs to be analysed together with Table 5.1 to show exactly the integrated areas under the TPD peaks. Table 5.1 shows the integrated areas under the TPD peaks for mass 29 (^{13}CO), mass 30 (NO), mass 44 (CO_2+N_2O) and mass 45 ($^{13}CO_2$) (not shown in Figure 5.3). The areas shown in Table 5.1 are average areas obtained from all TPD experiments for co-adsorbed systems performed after fs-LID. Areas under TPD curves for co-adsorbed systems were reproducible within ± 5%. This percentage was calculated from standard deviation of the data.

Table 5.1 Integrated areas under the TPD curves for masses 28 (N_2 or CO), 29 (^{13}CO), 30 (NO), 44 (N_2O or CO_2) and 45 ($^{13}CO_2$) for 2 L NO/ 2 L ^{13}CO and 4 L NO/ 2 L ^{13}CO on Pd(111).

	TPD integrated areas				
Adsorbate system	Mass 29 (^{13}CO)	Mass 30 (NO)	Mass 28 (N_2)	Mass 44 (N_2O)	Mass 45 ($^{13}CO_2$)
2 L NO/2 L ^{13}CO	5.3×10^5	2.4×10^5	3.0×10^5	4.4×10^4	1.1×10^4
4 L NO/2 L ^{13}CO	1.3×10^5	4.4×10^5	1.8×10^5	6.5×10^4	5.6×10^3

From Figure 5.3 and Table 5.1 it can be observed clearly that NO displaces CO. The average area under the mass 31 (^{15}NO) TPD desorption peak is almost two times higher for 4 L ^{15}NO/ 2 L CO than for 2 L ^{15}NO/ 2 L CO on Pd(111), and in RAIR experiments the area under the three-fold hollow NO peak is 1.6 times higher, since some of the NO adsorbs in bridge sites on defects (probably (100) steps). These two sites do not have similar desorption energies, E_{ads} (NO on Pd(111), 3-fold hollow site) = −193 kJ mol^{-1}, [26] E_{ads}(NO on Pd(100), bridge site) = −145 kJ mol^{-1}, [28] but in the TPD spectrum for mass 30 only one peak is seen. The TPD peak is very broad, so the probable reasons for observing only average desorption profile are due to diffusion occurring before desorption or due to desorption from a heterogeneous surface (surface with defects).

The area under the TPD mass 29 (^{13}CO) peak is four times lower for 4 L NO/2 L ^{13}CO than for 2 L NO/2 L ^{13}CO, and it is 2.2 times lower in the RAIR experiments. If the area under the mass 29 TPD peak for 2 L NO/ 2 L ^{13}CO (Table 5.1) is compared with the area under the pure 2 L ^{13}CO TPD peak (Chapter 4, Section 4.4.1), it can be observed that they are the same within experimental error. The coverage for a 2 L ^{13}CO exposure corresponds to 60% of the saturation coverage, so 15% of the CO remains on the Pd(111) surface following a NO dose of 4 L. It is not only that the area under the CO desorption peak considerably decreases, but instead of one desorption peak, two desorption peaks can be observed (Figure 5.3). The desorption peak with the maximum at lower temperature can be assigned to CO adsorbed in the bridge sites, and the one at higher temperature can be assigned to CO adsorbed in the three-fold hollow sites. These assignments are based on RAIR spectra (Figure 5.1) that indicate that CO is first moved from the three-hollow site to the less-favoured bridge and atop sites with increasing NO exposure, and then it is desorbed. The position of the desorption peak for CO in the three-fold hollow site shifts to lower temperature for higher exposure of NO adsorbed

on 2 L CO/Pd(111). From the Redhead equation (Equation 4.3, Chapter 4) [29], desorption activation energies for CO and NO can be estimated assuming first order desorption. From Figure 5.3 it can be observed that T_{max} is at 530 K for 2 L ^{13}CO, giving an activation energy for first-order desorption of 147 kJ mol^{-1}, with a pre-exponential factor of 10^{13} s^{-1}. The first-order desorption activation energy for mass 28 (CO) in 2 L ^{15}NO/ 2 L CO/ Pd(111) is 136 kJ mol^{-1}, and for mass 28 (CO) in 4 L ^{15}NO/ 2 L CO/ Pd(111) it is 143 kJ mol^{-1} for desorption from the three-fold hollow site, and 154 kJ mol^{-1} for the desorption from the bridge site. The activation energy for first-order desorption of mass 30/31 (NO/ ^{15}NO) in 2 L NO, 4 L NO and 4 L ^{15}NO/ 2 L CO is 156 kJ mol^{-1}. In 2 L ^{15}NO/ 2 L CO the activation energy for first-order desorption of mass 31 (^{15}NO) is higher, about 160 kJ mol^{-1}, showing that CO does influence NO when CO is still on the surface. This is the only mass 29 (^{13}CO) system (Figure 5.3a) where two desorption peaks are observed, corresponding to CO adsorbed on two different sites or in two different environments (pure CO and CO next to NO). Clearly, there is an effect of NO on the amount of CO and an effect of CO on the position of the T_{max} in NO TPD curve.

It is also necessary to explain the most probable mechanism for formation of the observed reaction products: N_2O, CO_2 and N_2. There is a high probability of finding both molecular and dissociated NO species on a metal surface [14], because of the one extra electron in the $2\pi^*$ orbital compared to the CO molecule. This is because NO has a low internal bond energy (630 kJ mol^{-1}) [30] when compared to CO (1076 kJ mol^{-1}) [30]. It is therefore assumed that CO_2, N_2 and N_2O are formed after the dissociation of NO on the surface. There is currently no agreement about the mechanism for the CO–NO reaction on Pd; however, in a series of recent papers [31–33] it has been assumed that it is similar to that proposed a few years ago by Peden [34] and Permana [35] for Rh. This assumption is made on the basis of the closeness of Pd and Rh in the periodic table.

The mechanism is shown in Scheme 5.1, where S represents a vacant surface site and $CO_{(a)}$, $NO_{(a)}$, $N_{(a)}$, and $O_{(a)}$ are the species adsorbed on the surface.

$$CO + S \xrightarrow{k_1} CO_{(a)} \quad (1)$$

$$CO_{(a)} \xrightarrow{k_2} CO + S \quad (2)$$

$$NO + S \xrightarrow{k_3} NO_{(a)} \quad (3)$$

$$NO_{(a)} \xrightarrow{k_4} NO + S \quad (4)$$

$$NO_{(a)} + S \xrightarrow{k_5} N_{(a)} + O_{(a)} \quad (5)$$

$$2N_{(a)} \xrightarrow{k_6} N_2 + 2S \quad (6)$$

$$CO_{(a)} + O_{(a)} \xrightarrow{k_7} CO_2 + 2S \quad (7)$$

$$NO_{(a)} + N_{(a)} \xrightarrow{k_8} N_2O + 2S \quad (8)$$

Scheme 5.1. Mechanism of CO-NO reaction on Pd(111). Taken from ref. [18]

Scheme 5.1 shows that one of the important steps in the CO and NO reaction is the dissociation of NO. NO dissociation is not usually observed on Pd(111), but in Chapter 4 it was observed even for pure NO adsorbed on Pd(111) (Table 4.2, Section 4.4.2). It was concluded that the dissociation is due to the presence of defect sites, probably (100) steps. The dissociation of NO is clearly more pronounced when CO is co-adsorbed on the surface. Comparison of the pure 2 L NO system, and systems where 2 L NO is co-adsorbed with 2 L CO, shows that the ratio of the integrated area of mass 28 (N_2) to mass 30 (NO) is 0.52 for pure NO, and 1.25 for 2 L ^{13}CO/2 L NO.

From Figure 5.3 and Table 5.1, it can also be observed that the amount of mass 28/30 (N_2/ $^{15}N_2$) is higher for lower NO coverages. At first, this seems strange, but if this result is compared with the pure NO system (Chapter 4), then the same thing can be observed: the amount of mass 28 (N_2) is higher for 2 L NO than 4 and 10 L NO exposure. For NO/CO/Pd(111) and pure NO/Pd(111), at lower NO exposure N_2 formation is obviously more favourable compared to the process of N_2O formation. For N_2 formation, twice as much dissociation of NO is needed compared to the process of N_2O formation (Scheme 5.1).

If the mass 44 (CO_2) TPD curves are compared for 2 and 4 L NO exposure for NO/CO/Pd(111), then two things can be observed: the first is that the position of the mass 44 T_{max} for 4 L ^{15}NO/2 L CO/Pd(111) coincides with the position of the mass 28

(CO) T_{max} for CO adsorbed in a three-fold hollow site. The formation of CO_2 obviously happens only in three-fold hollow sites, and not in the bridge site. The second is that the area under the mass 44 TPD desorption peak is higher for lower NO exposure, because at higher NO coverage, there is less CO on the surface to react to form CO_2.

The mass 46 ($^{15}N_2O$) TPD curves look similar (Figure 5.3 d), and from Table 5.1 it can be seen that the amount of N_2O desorption is lower for 2 L NO/2 L ^{13}CO compared to 4 L NO/2 L ^{13}CO. However, the first co-adsorbed system shows more N_2 formation, so less N is available for reaction with NO, and less NO (lower NO coverage) is also available than for the second co-adsorbed system.

Overall, two co-adsorbed systems with initially pre-dosed CO show different selectivity for N_2O versus N_2 production. The branching ratio of N_2O/N_2 is higher for 4 L ^{15}NO/2 L CO than for 2 L ^{15}NO/2 L CO. This is consistent with high pressure RAIR study of CO + NO reaction [36], where higher N_2O/N_2 ratio correlated with higher $[NO_a]/[CO_a]$ ratio.

5.3.2 RAIRS and TPD characterisation of CO/NO/Pd(111)

The experiments described above were also repeated by first dosing NO and then exposing the surface to CO to see if this altered the way in which the two species interact with each other on the surface. Figure 5.4 shows RAIR spectra with an initial NO dose of 2 L following an increasing exposure of CO.

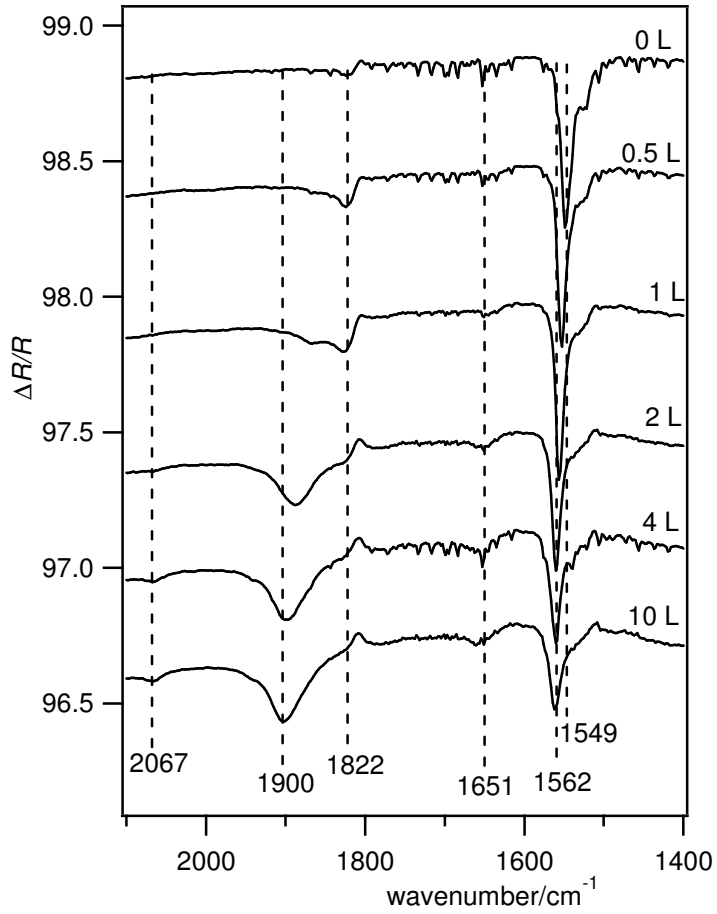

Figure 5.4 RAIR spectra for different exposures of CO on 2 L NO/Pd(111) at T = 320 K. The CO exposure is varied from 0 to 10 L.

For 2 L NO exposure, three vibrational bands can be observed. The band at 1549 cm^{-1} is assigned to NO in a three-fold hollow site, the band at 1651 cm^{-1} is assigned to NO adsorbed on defects, and a band at 1822 cm^{-1} is assigned to the small amount of residual CO adsorbed in the three-fold hollow site from the background in the chamber. With increasing exposure of CO, the intensity of the band associated with the NO in the three-fold hollow site, decreases and shifts to higher wavenumbers, while the intensity of the CO three-fold hollow site vibrational band increases and shifts from 1822 to 1900 cm^{-1}. The intensity of the band for NO adsorbed on bridge sites (1651 cm^{-1}) gradually increases with increasing CO exposure. From RAIR spectra alone, it could be concluded that the amount of NO adsorbed in three-fold hollow sites decreases, following CO adsorption. RAIR spectra can be more clearly analysed if the integrated areas under the RAIR peaks for CO and NO adsorbed in three-fold hollow sites are

calculated. Figure 5.5 shows the integrated RAIR absorbance for CO (in the three-fold hollow site or bridge site) and NO (in the three-fold hollow site) for 2 L NO/Pd(111) as a function of increasing CO exposure.

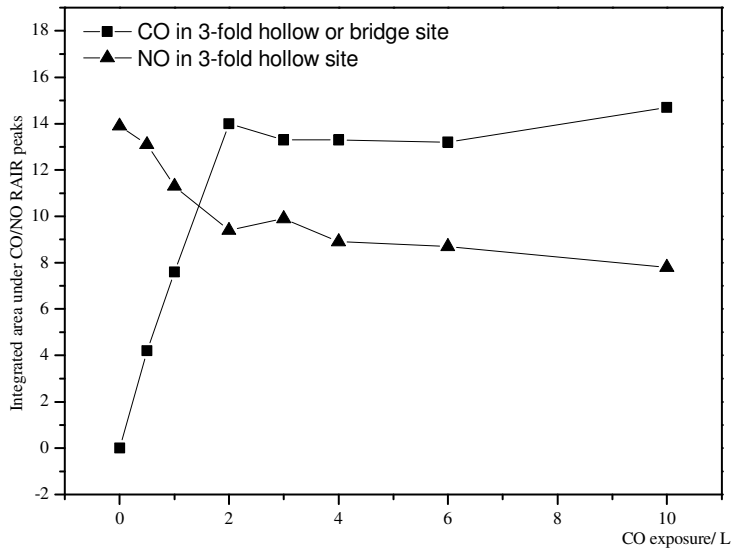

Figure 5.5 Integrated areas under RAIR peaks for CO in the three-fold hollow site and bridge site and for NO adsorbed in the three-fold hollow site as a function of NO exposure.

From Figure 5.5 and Figure 5.2 it can be clearly noted that the CO integrated area (A = 14.7) for the 10 L CO/2 L NO/Pd(111) system is lower than the CO area (A = 15.7) for the pure 2 L CO on Pd(111) system. It can also be noted that the integrated area under the three-fold hollow NO peak is almost halved when 2 L NO and 10 L CO/2 L NO systems on Pd(111) are compared. TPD spectra for 4 L CO/2 L ^{15}NO/Pd(111), 2 L CO/2 L ^{15}NO/Pd(111), 2 L NO, 2 L ^{13}CO and 4 L ^{13}CO (Figure 5.6) show that the amount of NO is lower for mixed systems when compared to pure 2 L NO on Pd(111), and this agrees with the observed decrease in integrated area under the three-fold hollow site NO peak from 13.9 for 2 L NO to 8.9 for 4 L CO/2 L NO/Pd(111). As was mentioned in Section 5.3, experiments with ^{15}NO were performed after all fs-LID experiments were finished, so they were only performed twice for each co-adsorbed system. Figure 5.6 needs to be analysed together with Table 5.2 to show exactly the integrated areas under the TPD peaks. Table 5.2 shows the integrated areas under the TPD peaks for mass 29 (^{13}CO), mass 28 (N_2 + CO), mass 30 (NO), mass 44 (CO_2 +

N_2O) and mass 45 ($^{13}CO_2$). The areas shown in Table 5.2 are average areas obtained from all TPD experiments for co-adsorbed systems performed after fs-LID. Areas under TPD curves were reproducible within ± 5%.

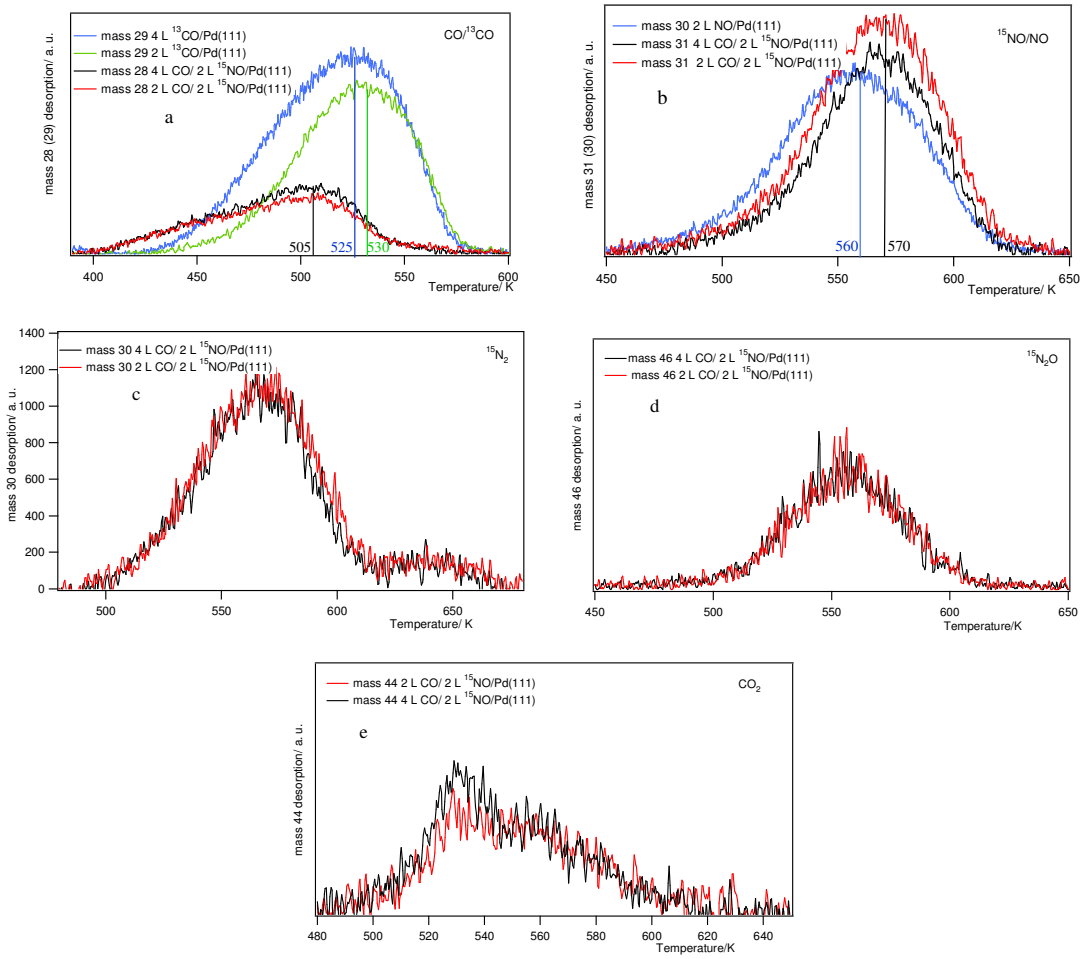

Figure 5.6 TPD spectra of a) mass 28 (CO), b) mass 31 (^{15}NO), c) mass 30 ($^{15}N_2$), d) mass 46 ($^{15}N_2O$) and e) mass 44 (CO_2) following CO adsorption on 2 L ^{15}NO/Pd(111) at T = 320 K taken at 2 L and 4 L CO exposure.

Table 5.2 Integrated areas under the TPD curves for masses 28 (N_2 or CO), 29 (^{13}CO), 30 (NO), 44 (N_2O or CO_2) and 45 ($^{13}CO_2$) for 2 L ^{13}CO/ 2 L NO and 4 L ^{13}CO/ 2 L NO on Pd(111).

	TPD integrated areas				
Adsorbate	Mass 29 (^{13}CO)	Mass 30 (NO)	Mass 28 (N_2)	Mass 44 (N_2O)	Mass 45 ($^{13}CO_2$)
2 L ^{13}CO/2 L NO	3.1×10^5	3.6×10^5	1.7×10^5	2.8×10^4	1.1×10^4
4 L ^{13}CO/2 L NO	2.3×10^5	2.7×10^5	1.0×10^5	2.3×10^4	6.5×10^3

From Figure 5.6 and Table 5.2 it can be observed clearly that CO is not able to displace pre-dosed ^{15}NO, as expected. The mass 28 TPD desorption curve (Figure 5.6 a) shows that the amount of CO adsorbed on the surface for 4 L CO/2 L ^{15}NO/Pd(111) is slightly lower than the amount of CO for 2 L CO/2 L ^{15}NO/Pd(111). This result is in agreement with RAIRS findings shown in Figure 5.5. The amount of adsorbed NO is also higher for the system with lower CO exposure. These findings can be due to the error in dosing, but may also be due to the influence of extra CO on the Pd(111) surface saturated with a CO/NO mixture. The relative ratios of the integrated TPD areas for mass 28 (N_2), mass 44 (N_2O), and mass 45 ($^{13}CO_2$) to mass 30 (NO) for both of the systems shown in Figure 5.6 is the same. Therefore, both systems have same N_2O/N_2 branching ratio, as expected based on similar $[NO_a]/[CO_a]$ ratios. In the experiments presented here, it has been shown that NO will displace pre-dosed CO, but CO will not cause significant desorption of pre-dosed NO. However, it can be observed that adding more CO than the saturation coverage, for the surface initially predosed with NO, causes desorption of CO and NO.

From a simple Redhead analysis, the activation energy for first order desorption can be estimated, using a value of the pre-exponential factor of 10^{13} s^{-1}. For mass 28/29 ($CO/^{13}CO$) in Figure 5.6 the activation energy is 148 kJ mol^{-1} for 4 L ^{13}CO and 2 L ^{13}CO, and 140 kJ mol^{-1} for 2 L CO/ 2 L ^{15}NO and 4 L CO/ 2 L ^{15}NO. For mass 31 (30) in Figure 5.6 the activation energies for desorption are 156 kJ mol^{-1} for 2 L NO and 159 kJ mol^{-1} for 4 L CO/ 2 L ^{15}NO and 2 L CO/ 2 L ^{15}NO. Hence, it can be observed that co-adsorption of CO and NO decreases the desorption activation energy of CO, and increases the desorption activation energy of NO, no matter what the sequence of dosing is.

It is known from the literature, that the desorption of both CO and NO on Pd(111) is first order (Chapter 4). [37] The order of the desorption is important because it is related to the shape of the TPD curves and the position of the peak maximum. First order desorption curves are usually asymmetric, with a steady slope up to the peak and then falling away rapidly at temperatures above the peak. If the desorption activation energy did not depend on coverage, then the peak temperature would not change as a function of coverage. [38] However, usually this is not the case, because the desorption activation energy depends on coverage. For a first order desorption process, where the activation energy for desorption decreases with coverage, the desorption maximum shifts down in temperature with increasing coverage. Here, in the co-adsorbed system on Pd(111), the

desorption maximum for CO in the co-adsorbed systems shifts down in temperature compared to pure CO. There is less CO in the co-adsorbed systems (Table 5.1 and Table 5.2), so the opposite shift in desorption maximum is expected if the trend in the desorption activation energy were the same as for pure CO system. The shape of the curve for CO in co-adsorbed systems changes with respect to the pure CO on Pd(111), becoming more assymmetric. Change in the desorption energy and in the shape of the TPD curve is probably related to the change in the pre-exponential factor ν_n, since there is a negligible probability that the reaction order will change due to the really small amount of CO_2 on the surface. The change in the pre-exponential factor is related to the change in the entropy of the metal-adsorbate system. Entropy change is related to the fact that NO forces CO to occupy less favourable sites on the surface, as is evident from RAIRS and TPD experiments. The desorption behaviour of NO is easier to explain. In co-adsorbed systems, there is slightly less NO than in pure systems. The desorption maximum should shift up in temperature for NO in co-adsorbed systems compared to pure NO, and this is exactly what happens.

5.3.3 Fs-LID of NO/CO/Pd(111) and CO/NO/Pd(111) – yield-vs-fluence curves for ^{13}CO and NO

The main goal of this section is to construct a phenomenological model that will enable comparison of TPD results with the fs-LID, and to compare the fs-LID experiments of mixed systems with pure ones, to see if any laser-induced reactions could be observed. First, a model that links TPD with fs-LID will be developed. Photoinduced processes in some one-dimensional models can be treated as activated processes [39–40]. In some of these models, the overall photodesorption process consists of two distinct steps: vibrational excitation and desorption.

Vibrational excitation can be modelled with electronic and lattice frictions within the electronic friction model [41]: the electronic and lattice degrees of freedom couple independently to the adsorbate, with strengths given by the frictional coupling coefficients, η_{el} and $\eta_{ph,}$ respectively. The empirical friction model was shown to be a good empirical model for describing subpicosecond photodesorption [39 41–44]. Desorption of the adsorbate was treated within a one dimensional activation-energy barrier

crossing, so for first order desorption, the Polanyi-Wigner rate equation could be written:

$$R_d = -\frac{d\theta}{dt} = \theta \nu_{PW} \exp\left[-E_a / k_B T_{ads}(t)\right] , \qquad (5.1)$$

where θ was the coverage, t was time, E_a was the desorption activation energy, and ν_{PW} was the prefactor and $T_{ads}(t)$ is the temporal evolution of the adsorbate temperature. There are several cases where E_a obtained from TPD data has been used successfully in simulating photodesorption with an empirical friction model [40, 42, 44], hence E_a from TPD spectra is also used here to model the photodesorption yield. The first shot yield at a particular laser fluence can be calculated as the time-integrated desorption rate. Calculating T_{ads} is a complicated procedure, explained in Chapter 1, Section 1.7. The main assumption in this qualitative description of fs-LID in co-adsorbed systems, is that T_{ads} for pure CO (NO) is the same as T_{ads} for CO (NO) in co-adsorbed systems. Hence, all the changes in the photodesorption yield are either due to a change in the activation energy, reaction order or pre-exponential factor. In order to analyse the data presented in this chapter, $T_{ads}(t)$ for one laser fluence (F = 18 mJ cm^{-2}) for pure CO/Pd(111) is assumed to be the same as $T_{ads}(t)$ calculated in reference [45]. A qualitative model, based on Equation 5.1, is then used only to explain the changes in the photodesorption yield of pure CO (NO) compared to CO and NO in co-adsorbed systems. Therefore, T_{ads} for NO is assumed to be the same as T_{ads} for CO, since any slight change in the T_{ads} profile would not influence the ratio of the photodesorption yield of pure NO compared to NO in co-adsorbed systems. In order to calculate $T_{ads}(t)$, temporal profiles of electron temperature, $T_e(t)$ and phonon temperature, $T_p(t)$ need to be known. The detailed procedure for obtaining T_e and T_p from the two temperature model is explained in Chapter 1.

Thus, overall, the activation energy calculated from TPD spectra is the same activation energy used in Equation 5.1 to describe fs-LID. The pre-exponential factor is assumed to be 10^{13} s^{-1}, the same as in TPD experiments. In this experimental set-up, in a laser-induced desorption experiment only one mass could be collected at one time. Therefore, the yield *vs* fluence curves (Section 4.5 Chapter 4) were recorded only for the reactants CO and NO, for the same systems as already described by TPD. The results were compared with pure CO or NO systems at appropriate coverages.

Figure 5.7 shows the mass 30 yield *vs* fluence curves for 2 L NO/2 L ^{13}CO, 4 L NO/2 L ^{13}CO, 4 L NO and 2 L NO.

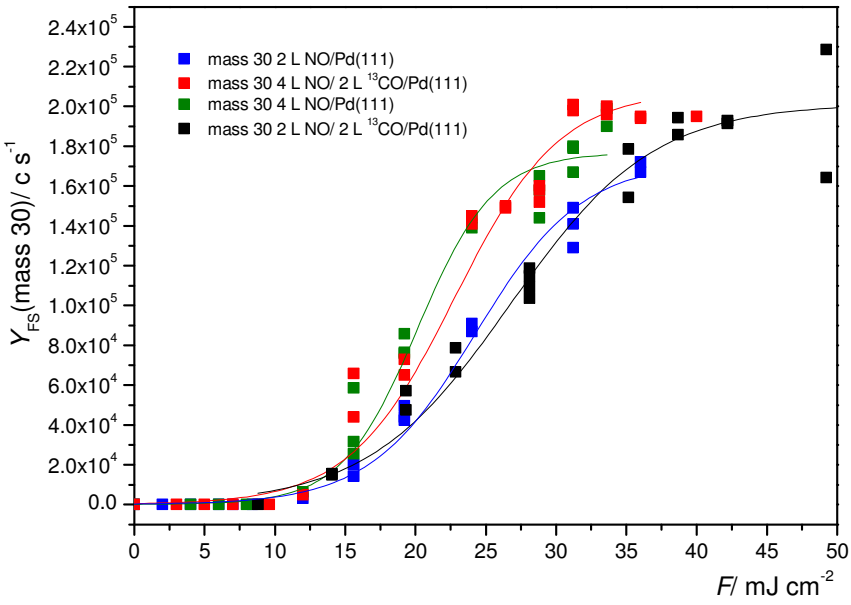

Figure 5.7 Mass 30 yield-*vs*-fluence dependence curves for ■ 4 L NO/ 2 L ^{13}CO, ■ 2 L NO/ 2 L ^{13}CO, ■ 4 L NO and ■ 2 L NO at T = 340 K. Solid lines are power fits to the data: – 4 L NO/ 2 L ^{13}CO, – 2 L NO/ 2 L ^{13}CO, – 4 L NO. – is a line to guide the eye for 2 L NO.

It is obvious from Figure 5.7, that the power fit cannot be fitted over the whole fluence range studied, because the photodesorption yield becomes saturated. The saturation fluence can be determined by fitting sigmoids to the data. An s-logistic curve was fitted to the data using the least squares method. The first derivative of the s-logistic curve, for all systems shown in Figure 5.7, was set to zero, and then the saturation fluence was determined. Saturation fluences together with R^2 values that provide the information about the goodness of fit are listed in Table 5.3. R^2 values are provided for all fits in this chapter as they were in Chapter 4. An s-logistic curve could not be fitted for 2 L NO, because there are not enough points near the saturation coverage.

Table 5.3 Saturation fluences calculated for the systems shown in Figure 5.7. R^2 values provide the information about goodness of fit.

Adsorbate system	F_{sat}/ mJ cm^{-2}	R^2
2 L NO/ 2 L ^{13}CO	80	0.999
4 L NO	50	0.994
4 L NO/ 2 L ^{13}CO	65	0.992

Table 5.3 shows that the saturation fluence is highest for the 2 L NO/2 L ^{13}CO system, which is the system with the highest T_{max} in the TPD curve. The activation energy for first order desorption is highest for this system, and therefore the desorption yield of NO molecules is expected to be the lowest. As a result of this, the saturation fluence will be shifted towards higher fluences with respect to other systems that have lower desorption activation energies. From the fitted curves in Figure 5.7, the inflection point can be easily found. As was explained in Chapter 4 (Section 4.6.2) only fluences before the inflection point are used for power fits. Yield-*vs*-fluence dependence curves for power fits are shown in Figure 5.8, and the parameters *a* and *b* obtained from these power fits are listed in Table 5.4.

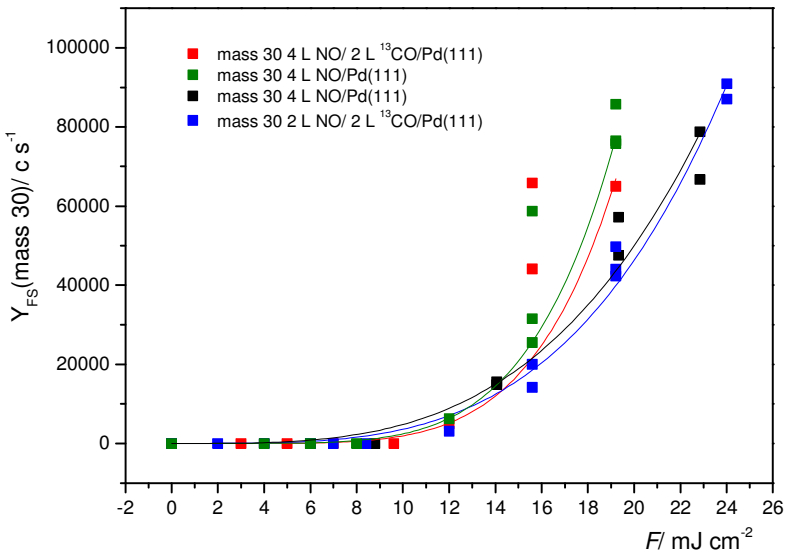

Figure 5.8 Mass 30 yield-*vs*-fluence dependence curves for ■ 4 L NO/ 2 L ^{13}CO, ■ 2 L NO/ 2 L ^{13}CO, ■ 4 L NO and ■ 2 L NO at T = 340 K. Solid lines are power fits to the data: – 4 L NO/ 2 L ^{13}CO, – 2 L NO/ 2 L ^{13}CO, – 4 L NO and – 2 L NO.

Table 5.4 Parameters a and b obtained by a power fit, $Y_{FS} = aF^b$ for the mass 30 yield-*vs*-fluence dependence curves for the photodesorption of NO/^{13}CO on Pd(111) shown in Figure 5.8. R^2 values provide the information about goodness of fit.

2 L NO	$Y_{\mathrm{FS}} = aF^b$	$a = 0.8 \pm 0.5$ $b = 3.7 \pm 0.2$	$R^2 = 0.991$
2 L NO/ 2 L ^{13}CO/Pd(111)	$Y_{\mathrm{FS}} = aF^b$	$a = 2.0 \pm 0.9$ $b = 3.4 \pm 0.2$	$R^2 = 0.972$
4 L NO	$Y_{\mathrm{FS}} = aF^b$	$a = 0.012 \pm 0.009$ $b = 5.3 \pm 0.2$	$R^2 = 0.995$
4 L NO/ 2 L ^{13}CO/Pd(111)	$Y_{\mathrm{FS}} = aF^b$	$a = 0.006 \pm 0.01$ $b = 5.5 \pm 0.7$	$R^2 = 0.914$

From Figure 5.8 it can be observed that there is slightly less NO desorption in co-adsorbed systems than in the pure NO system. The power law behaviour is almost the same within the experimental error of the fit, so there is no obvious difference in parameters a and b for the pure NO compared to the same exposure of NO in co-adsorbed systems. It is interesting to try and link this photodesorption behaviour with the results from the TPD. From the TPD curves, it can be observed that $T_{\max}$ is slightly shifted for mixed systems compared to the pure systems. The shift in $T_{\max}$ for 4 L ^{15}NO/2 L CO, with respect to 4 L NO is negligible (~5 K), but becomes significant for 2 L ^{15}NO/2 L CO with respect to 2 L NO (~15 K). Even though the a and b parameters obtained from the power law fit, for 2 L NO and 2 L ^{15}NO/2 L CO, are the same within the error of the fit, Y_{FS} is lower for the co-adsorbed system than for the pure NO system. This finding agrees with the shift of $T_{\max}$ in the TPD. Thus for this system, it is possible to predict the photodesorption behaviour, based on E_{a} from TPD. The most pronounced effect in the photodesorption yield is between the mass 30 photodesorption yield for 2 L NO and 2 L NO/2 L ^{13}CO. Equation 5.2 can be used to predict the ratio of the photodesorption yield for co-adsorbed systems to the pure system.

$$\frac{Y_{FS,2LNO}}{Y_{FS,2LNO/2L^{13}CO}} = \frac{\vartheta_{2LNO}}{\vartheta_{2LNO/2L^{13}CO}} \int_0^{6\,ps} \exp\left(-\frac{E_{a,2LNO} - E_{a,2LNO/2L^{13}CO}}{RT_{ads}(t)}\right) dt \approx 1.3 \times 1.1 \approx 1.4 \qquad (5.2)$$

All variables in Equation 5.2 are as already indicated for Equation 5.1. The ratio of the average TPD area is used to give the ratio of ϑ_{2LNO} and $\vartheta_{2LNO/2L^{13}CO}$, from Table 4.2 (Chapter 4, Section 4.4.2) and from Table 5.2, respectively. The photodesorption yield should be about 1.4 times higher for mass 30 2 L NO on Pd(111) than for mass 30 for the 2 L NO/2 L ^{13}CO system. The power fits predict that the photodesorption yield for the mass 30 2 L NO system will be 1.1 times higher than that for mass 30 2 L NO/2 L ^{13}CO at a fluence of 18 mJ cm^{-2}. For 4 L NO/2 L ^{13}CO, the calculated photodesorption ratio is 1.3, and the experimental photodesorption ratio is 1.2.

Clearly, for mass 30 desorption in the NO/CO/Pd(111) system, the desorption activation energy change between the pure and coadsorbed systems agrees well with the observed photodesorption ratio at F = 18 mJ cm^{-2}, showing that the model works well in this case.

Figure 5.9 and Table 5.5 show results for mass 29 (^{13}CO) desorption for the same systems as shown for NO.

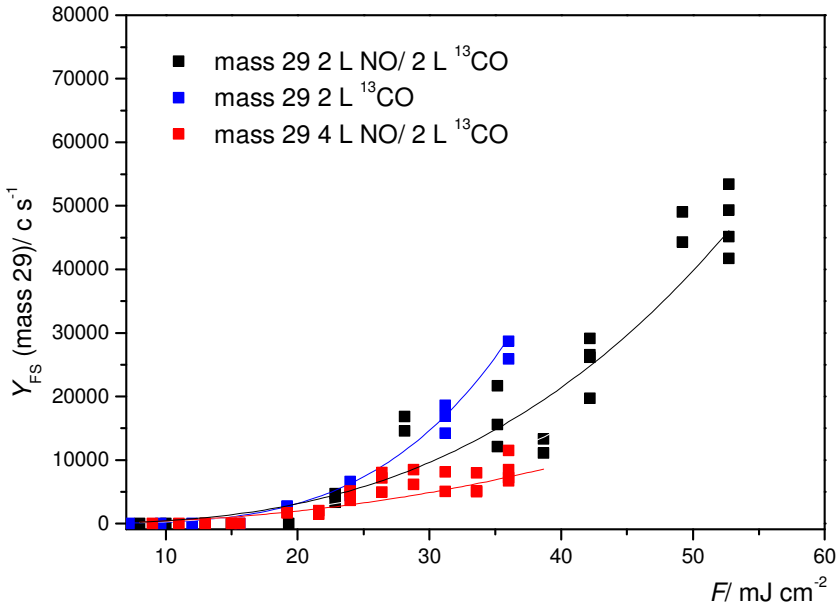

Figure 5.9 Mass 29 yield-*vs*-fluence dependence curves for ■ 4 L NO/ 2 L ^{13}CO, ■ 2 L NO/ 2 L ^{13}CO and ■ 2 L ^{13}CO at T = 340 K. Solid lines are power fits to the data: – 4 L NO/ 2 L ^{13}CO, – 2 L NO/ 2 L ^{13}CO, – 2 L ^{13}CO.

Table 5.5 Parameters a and b obtained by a power fit, $Y_{FS} = aF^b$ for the mass 29 yield-*vs*-fluence dependence curves for the photodesorption of NO/^{13}CO on Pd(111) shown in Figure 5.9. R^2 values provide the information about goodness of fit.

4 L NO/2 L ^{13}CO/Pd(111)	$Y_{FS} = aF^b$	$a = 2.5 \pm 2$ $b = 2.2 \pm 0.2$	$R^2 = 0.949$
2 L NO/2 L ^{13}CO/Pd(111)	$Y_{FS} = aF^b$	$a = 0.8 \pm 0.8$ $b = 2.8 \pm 0.3$	$R^2 = 0.887$
2 L ^{13}CO	$Y_{FS} = aF^b$	$a = 0.04 \pm 0.01$ $b = 3.8 \pm 0.1$	$R^2 = 0.966$

The mass 29 (^{13}CO) photodesorption behaviour is more difficult to link with the results obtained from TPD experiments. Equation 5.2 is used to predict the photodesorption ratio of the pure CO to CO in the co-adsorbed systems. It can be estimated that the desorption yield of mass 29 in the 2 L ^{13}CO system should be 0.7 times the desorption yield of mass 29 in the 2 L ^{13}CO/2 L NO system and 3.4 times higher than the desorption yield of mass 29 in 4 L ^{13}CO/2 L NO, for fluence, F = 18 mJ cm^{-2}.

From power fits, it is determined that the ^{13}CO photodesorption yield at 18 mJ cm^{-2} is 1.4 times higher for 2 L ^{13}CO than for 4 L NO/2 L ^{13}CO system, and this is 2.4 times lower than was calculated using Equation 5.2. The ^{13}CO photodesorption yield for the 2 L ^{13}CO system is 0.9 times the photodesorption yield for 2 L NO/2 L ^{13}CO. This result is in 20% agreement with the calculated photodesorption ratio. It is reasonable to assume, (based on the TPD analysis in the previous section) that the pre-exponential factor for photodesorption of CO co-adsorbed with NO would be different to the pre-exponential factor of pure CO. Hence, the Redhead equation [29] using a pre-exponential factor of 10^{13} s^{-1} would not be valid. It seems that the pre-exponential factor does not change significantly for ^{13}CO photodesorption in the 2 L NO/2 L ^{13}CO system, but it changes by a large amount for ^{13}CO photodesorption in the 4 L NO/2 L ^{13}CO system. There are only a small number of preferred three-fold hollow sites available for ^{13}CO adsorption in the 4 L NO/2 L ^{13}CO system, because NO forces CO to occupy less favourable bridge and atop sites. Therefore, the entropy change upon desorption is probably higher (resulting in a higher pre-exponential factor) for the 4 L NO/2 L ^{13}CO system than for the ^{13}CO system.

From Figure 5.9 it can be observed that until about 27 mJ cm^{-2}, the photodesorption yields for all three systems are similar, and then the photodesorption yields start to differ. So, it seems that CO photodesorption behaviour is complex, and needs to be explained for the low fluence region as well as for the high fluence region.

However, a general trend can be observed. The photodesorption for co-adsorbed systems is lower than the photodesorption for pure 2 L ^{13}CO systems. It is known from DFT calculations that the repulsion energies between CO and NO on Pd(111) are slightly lower than the NO-NO and CO-CO repulsion energies [15], and lower repulsion energy corresponds to less photodesorption. 4 L NO/2 L ^{13}CO is the only mass 29 system which shows sigmoidal behaviour, hence saturation is reached for mass 29. This is probably because, for this system, only a very small amount of CO is left on the surface.

Here, a trend in the values of the prefactor *a*, can be seen. For mass 29 in the 4 L NO/2 L ^{13}CO system, the value of the prefactor ($a = 2.5$) is the highest, even though the CO coverage is very low, about 15% of the saturation coverage. It decreases to 0.5 for 2 L NO/2 L ^{13}CO and then it drops for pure 2 L ^{13}CO to 0.04. The value of the prefactor *a* is not only linked to the coverage of CO, but also the coverage of NO and probably also to interaction between the adsorbates. In Chapter 4, Section 4.6.2, it was observed that for the lowest NO exposure (2 L), the value of the prefactor *a* was the highest. For that exposure, about 10% of CO was adsorbed on the surface (confirmed by TPD and RAIRS). Unfortunately, at this stage it is not possible to link the coverages of different adsorbates and their interactions with the value of the prefactor *a*.

Given the differences observed in TPD spectra which depend on the order of dosing, it is interesting to see what will happen in the fs-LID experiments in the case when 2 L NO is dosed first on the Pd(111) surface. Figure 5.10 shows the mass 30 yield-*vs*-fluence dependence curves for 4 L ^{13}CO/2 L NO/ Pd(111), 2 L ^{13}CO/2 L NO/ Pd(111) and 2 L NO/Pd(111).

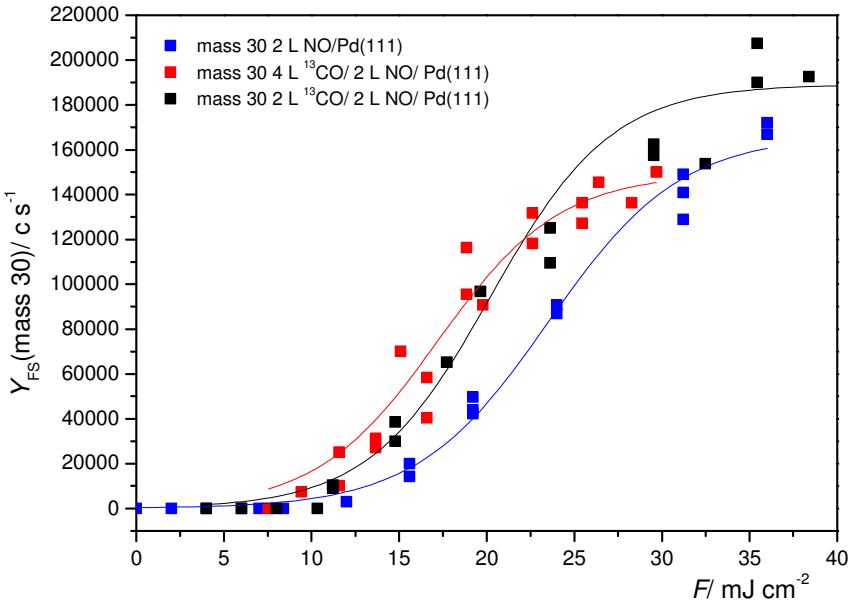

Figure 5.10 Mass 30 yield-*vs*-fluence dependence curves for ■ 4 L ^{13}CO/ 2 L NO, ■ 2 L ^{13}CO/ 2 L NO and ■ 2 L NO at T = 340 K. Solid lines are power fits to the data: – 4 L ^{13}CO/ 2 L NO, – 2 L ^{13}CO/ 2 L NO and – 2 L NO.

Again, from Figure 5.10, it is clear that a power law is not valid for the whole fluence range. Yield-*vs*-fluence curves again show sigmoidal behaviour, and so s-logistic curves were fitted for the coadsorbed systems. From the s-logistic curves, the saturation fluence can be calculated, and the results are shown in Table 5.6. Again, an s-logistic curve could not be fitted for 2 L NO because there were insufficient data points near the saturation coverage.

Table 5.6 Saturation fluences calculated for systems shown in Figure 5.10. R^2 values provide the information about goodness of fit.

adsorbate system	F_{sat}/ mJ cm^{-2}	R^2
2 L ^{13}CO/ 2 L NO	57	0.973
4 L ^{13}CO/ 2 L NO	54	0.969
2 L NO	–	–

The co-adsorbed systems in this case have similar amounts of ^{13}CO and NO (Table 5.3), so it is expected that the co-adsorbed systems would have similar desorption characteristics. Clearly, the saturation fluences for both systems are the same within the error bars. From the fitting curves in Figure 5.10, the inflection point can be determined easily. As was explained in Chapter 4 (Section 4.6.2) and earlier in this chapter (Section 5.3.3) only fluences before the inflection point are used for power fits. Power fit curves, and the resulting parameters, *a* and *b* are plotted in Figure 5.11 and listed in Table 5.7.

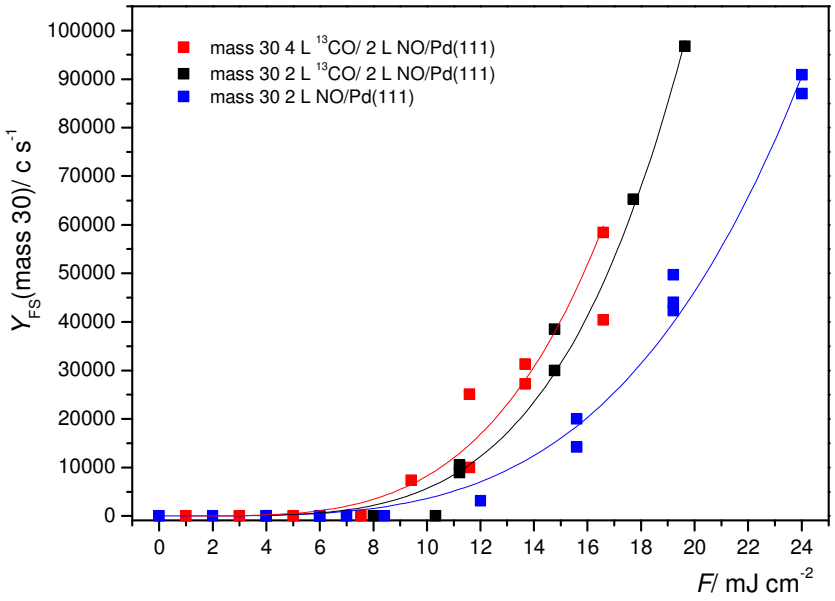

Figure 5.11 Mass 30 yield-*vs*-fluence dependence curves for ■ 4 L ^{13}CO/ 2 L NO, ■ 2 L ^{13}CO/ 2 L NO and ■ 2 L NO at T = 340 K. Solid lines are power fits to the data: – 4 L ^{13}CO/ 2 L NO, – 2 L ^{13}CO/ 2 L NO and – 2 L NO.

Table 5.7 Parameters *a* and *b* obtained by a power fit, $Y_{FS} = aF^b$ for the mass 30 yield-*vs*-fluence dependence curves for the photodesorption of ^{13}CO/NO on Pd(111) shown in Figure 5.11. R^2 values provide the information about goodness of fit.

4 L ^{13}CO/ 2 L NO/Pd(111)	$Y_{FS} = aF^b$	$a = 1 \pm 1$
		$b = 3.9 \pm 0.4$
2 L NO	$Y_{FS} = aF^b$	$a = 0.8 \pm 0.5$
		$b = 3.7 \pm 0.2$
2 L ^{13}CO/ 2 L NO/Pd(111)	$Y_{FS} = aF^b$	$a = 0.3 \pm 0.2$
		$b = 4.2 \pm 0.2$

Equation 5.2 is again used to obtain information about the changes for mass 30 in co-adsorbed systems with respect to pure NO. The ratio of the coverages is obtained from the average TPD areas from Table 4.2 (Section 4.4.2, Chapter 4) and Table 5.2. TPD spectra provide desorption activation energies for mass 30 in all systems shown in Figure 5.11. It can be estimated that the photodesorption yield of mass 30 for 2 L NO should be 0.9 times the desorption yield of mass 30 in 2 L ^{13}CO/2 L NO and 1.1 times higher than the desorption yield for 4 L ^{13}CO/ 2 L NO, for fluence, F = 16.6 mJ cm^{-2}. The fluence of 16.6 mJ cm^{-2} is the maximum fluence that can be used for a power fit for the 4 L ^{13}CO/ 2 L NO system, because the inflection point is at 17 mJ cm^{-2}. Unfortunately, the photodesorption yields determined from the power fits do not agree with the calculations. The photodesorption yield of mass 30 in the 2 L NO system is 0.6 times the desorption yield of mass 30 in the 2 L ^{13}CO/ 2 L NO and 0.4 times the desorption yield of mass 30 in the 4 L ^{13}CO/ 2 L NO system. Thus, adding CO to systems with predosed NO, makes NO desorb more than for a system containing just pure NO.

The photodesorption behaviour of NO in the co-adsorbed systems depends on the sequence of dosing. NO photodesorption is more difficult for co-adsorbed systems than for pure NO systems, if CO is dosed first onto the surface. These findings agree with Equation 5.1 that links TPD with photodesorption experiments. NO photodesorption is easier for co-adsorbed systems than for pure NO for systems with NO dosed onto the surface first, and in this case the model that links TPD findings with the predictions of photodesorption yield is not so useful.

By close inspection of the average TPD areas for NO/CO/Pd(111) (Table 5.1) and TPD areas for CO/NO/Pd(111) (Table 5.2), it can be observed that the amounts of N_2O and N_2 desorbed also depend on the sequence of dosing. Therefore, the influence of N_2O on NO desorption kinetics is different for NO/CO/Pd(111) compared to CO/NO/Pd(111). Due to the reaction of NO and N, the desorption order can change. The shape of the mass 30 TPD curves in co-adsorbed systems depends on the sequence of dosing, being more asymmetric for the systems where CO is dosed first. Using the same value of the pre-exponential factor, $\nu = 10^{13}$ s^{-1} for both co-adsorbed systems is probably no longer a good approximation. It is difficult to quantify these factors based on the provided data, therefore more information about the reaction kinetics is needed.

In light of the information obtained from the TPD spectra it can be concluded that the microscopic surroundings of the NO molecule will be different depending on the sequence of dosing, and that the Redhead equation is no longer valid for the system where NO is dosed first.

One possible explanation for the different surroundings of an NO molecule is that for co-adsorbed systems where CO is dosed first, NO molecules occupy sites so that NO-NO and NO-CO repulsions are minimised, because NO will occupy three-fold hollow sites and CO molecules will be forced to move to less favourable bridge and atop sites, but with lower CO-NO repulsions. For 2 L ^{13}CO/2 L NO there is less CO and NO on the surface than for 2 L NO/2 L ^{13}CO (based on the average TPD areas in Table 5.1 and Table 5.2), so probably this accounts for the higher CO-NO repulsion energy since both molecules prefer to occupy three-fold hollow sites. Results of DFT calculations performed by Honkala *et al.* [46] suggest that NO-CO repulsions are higher for systems where NO and CO both occupy three-fold hollow sites.

Yield-*vs*-fluence dependence curves for mass 29 in pure systems and co-adsorbed systems are shown in Figure 5.12, and the obtained parameters *a* and *b* are shown in Table 5.8.

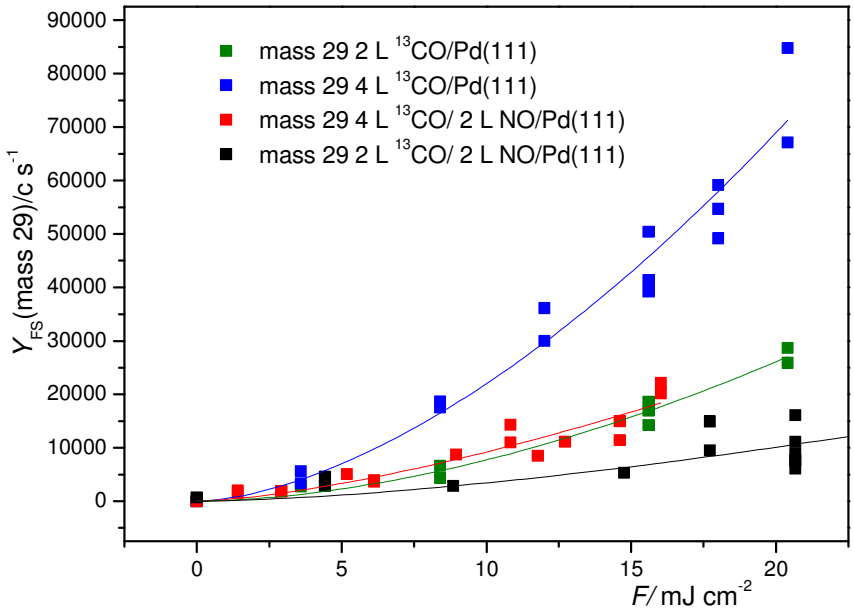

Figure 5.12 Mass 29 yield-*vs*-fluence dependence curves for ■ 4 L ^{13}CO/ 2 L NO, ■ 2 L ^{13}CO/ 2 L NO, ■ 2 L ^{13}CO and ■ 4 L ^{13}CO at T = 340 K. Solid lines are power fits to the data: – 4 L ^{13}CO/ 2 L NO, – 2 L ^{13}CO/ 2 L NO, – 4 L ^{13}CO, – 2 L ^{13}CO.

Table 5.8 Parameters a and b obtained by a power fit, $Y_{FS} = aF^b$ for the mass 29 yield-*vs*-fluence dependence curves for the photodesorption of ^{13}CO/NO on Pd(111) shown in Figure 5.12. R^2 values provide the information about goodness of fit.

2 L ^{13}CO/ 2 L NO/Pd(111)	$Y_{FS} = aF^b$	$a = 1 \pm 1$ $b = 2.7 \pm 0.3$	$R^2 = 0.935$
2 L ^{13}CO	$Y_{FS} = aF^b$	$a = 0.04 \pm 0.01$ $b = 3.8 \pm 0.1$	$R^2 = 0.966$
4 L ^{13}CO/ 2 L NO/Pd(111)	$Y_{FS} = aF^b$	$a = 0.02 \pm 0.01$ $b = 4.1 \pm 0.2$	$R^2 = 0.949$
4 L ^{13}CO	$Y_{FS} = aF^b$	$a = 0.3 \pm 0.1$ $b = 3.5 \pm 0.1$	$R^2 = 0.994$

First, Equation 5.2 is used to obtain information about the changes for mass 29 (^{13}CO) in co-adsorbed systems with respect to pure 2 L ^{13}CO. From this equation, it can be estimated that the desorption yield for mass 29 for 2 L ^{13}CO should be 1.3 times of the desorption yield for mass 29 in 2 L ^{13}CO/2 L NO and 1.7 times higher than the desorption yield for 4 L ^{13}CO/ 2 L NO, for fluence, F = 18 mJ cm^{-2}.

From the power fits, it is determined that at 18 mJ cm^{-2}, the desorption yield of mass 29 in 2 L ^{13}CO is 0.9 times the photodesorption yield of mass 29 in the 2 L ^{13}CO/ 2 L NO and 0.9 times the photodesorption yield of mass 29 in the 4 L ^{13}CO/2 L NO system. The experimental photodesorption yield (from the power fit) for these two systems again does not agree with the calculations based on Equation 5.1. The photodesorption yield of mass 29 for both of these systems should be higher than the photodesorption yield of mass 29 for pure 2 L ^{13}CO, but this is not the case. Even though, from the Redhead analysis, it is expected that the mass 29 photodesorption in co-adsorbed systems is higher than the mass 29 photodesorption for 2 L ^{13}CO on Pd(111) (except for 4 L NO/2 L ^{13}CO systems where CO coverage is very small). The mass 29 photodesorption is, for all co-adsorbed systems studied, lower than the mass 29 photodesorption for 2 L ^{13}CO/Pd(111). Therefore, for CO photodesorption, a model based on Equation 5.1 cannot predict photodesorption trends.

However, reflecting upon the strong influence of NO on the desorption of CO, the model describing CO photodesorption becomes clearer. The discrepancy between the

calculated and experimental photodesorption yield ratio can be explained if the pre-exponential factor in Equation 5.1 is, for both of the co-adsorbed systems, approximately twice the value of the pure ^{13}CO system. As was suggested for the 4 L NO/ 2 L ^{13}CO system, a higher entropy change for co-adsorbed systems can be based on the fact that NO does not allow CO to occupy three-fold hollow sites and this contributes to the lower entropy of the co-adsorbed systems with respect to the pure system where CO can occupy any site. Therefore, the entropy change (resulting in a higher pre-exponential factor) upon desorption should be higher for the co-adsorbed systems than for the pure system.

It is interesting to observe a trend in the parameters *a* and *b* for these three systems. Parameters *a* and *b* for 4 L ^{13}CO/2 L NO and 2 L ^{13}CO are the same within experimental error. For 2 L ^{13}CO/2 L NO the prefactor *a* is significantly higher (~25 times) than the prefactor for the 2 L ^{13}CO system. The exponent *b* is significantly lower ($b = 2.7$) than the 2 L ^{13}CO exponent, $b = 3.8$.

5.3.4 Reaction products in fs-LID of NO/CO/Pd(111) and CO/NO/Pd(111)

The reaction products for the co-adsorbed systems were recorded for just one fluence, $F = 24$ mJ cm^{-2}. The isotopes used were CO and ^{15}NO in order to distinguish between residual CO_2 and N_2O. In TPD experiments (carried out with ^{13}CO and NO) a small amount of mass 28 (N_2 + CO) and mass 44 (N_2O + CO_2) was observed for pure NO on Pd(111). TPD spectra of NO adsorbed on Pd(111) typically show that there is no NO dissociation [27], or that the dissociation is negligible [24]. Dissociation of NO on Pd(111) in TPD and RAIR experiments described in Chapter 4 was assigned to the presence of a small number of defect sites, probably (100) steps. [19]

In the fs-LID experiments of NO/Pd(111) performed in reference [47], NO dissociation was not detected. Therefore, before presenting the results for reaction products in the CO and NO reaction, it is necessary to observe whether there is any influence of defect sites on NO dissociation in the fs-LID experiments for pure NO adsorbed on Pd(111). Formation of N_2 was monitored by the QMS. In order to distinguish between N_2 and any residual CO from the background gas in the UHV chamber, the products resulting from the cracking pattern of CO and N_2 were monitored. The difference in the cracking patterns of CO and N_2 helped to distinguish between the two of them. The experiment

was performed at a fluence F ~20 mJ cm^{-2}, for mass 14 and mass 12, for an NO exposure of 2 L. Mass 14 was monitored because it is one of the products from the cracking pattern of N_2. Mass 12 is one of the products from the cracking pattern of CO. A QMS signal was not detected for mass 12, but it was detected for mass 14, therefore it can be concluded that NO also dissociates in fs-LID experiments. Figure 5.13 shows the depletion curve of mass 14 for 2 L NO on Pd(111), F = 20 mJ cm^{-2}.

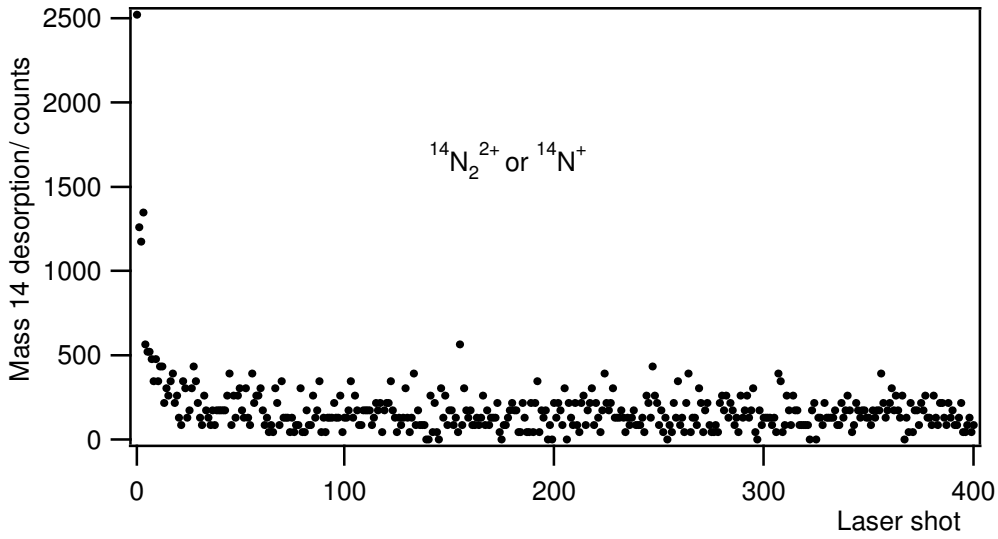

Figure 5.13 The depletion curve of mass 14 after fs-LID of 2 L NO/Pd(111), F = 20 mJ cm^{-2}, T = 340 K.

In light of the information provided for fs-LID of pure 2 L NO on Pd(111), it is not certain whether the reaction products, observed in the femtosecond laser-induced reaction of CO and NO co-adsorbed on Pd(111), are the result of laser irradiation, or due to the fact that the Pd(111) surface contains a small concentration of (100) defect sites. Depletion curves for N_2 formation observed in all co-adsorbed systems are shown in Figure 5.14, and the Y_{FS} for formation of mass 46 ($^{15}N_2O$), mass 44 (CO_2) and mass 30 ($^{15}N_2$) are shown in Table 5.9.

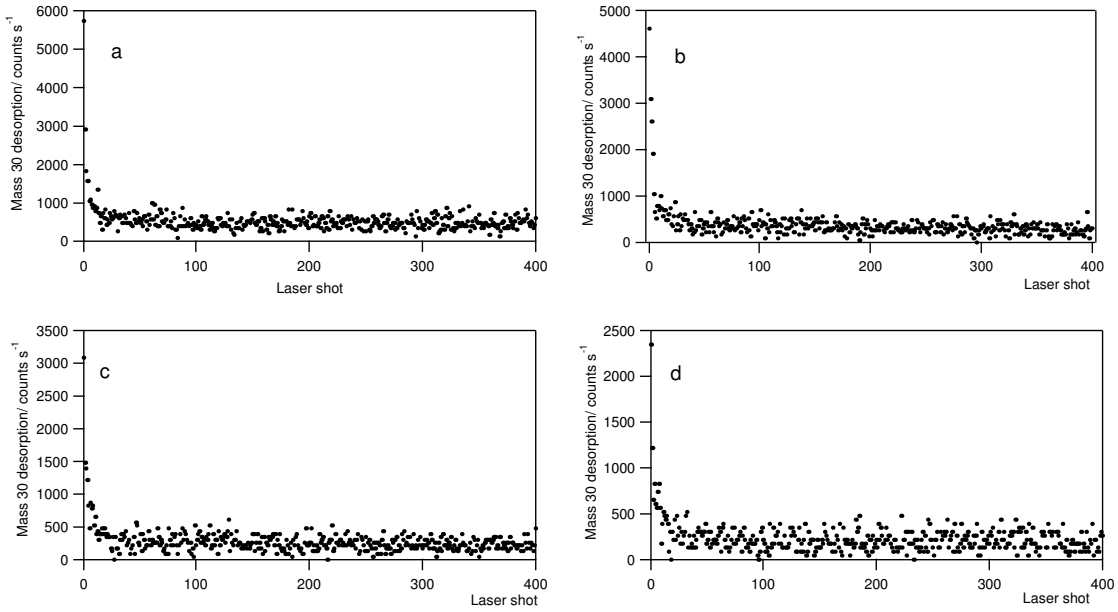

Figure 5.14 Depletion curves for mass 30 ($^{15}N_2$) for different coadsorbed systems: a 2 L ^{15}NO/2 L CO/Pd(111), b 4 L ^{15}NO/2 L CO/ Pd(111), c 2 L CO/2 L ^{15}NO/ Pd(111) and d 4 L CO/2 L ^{15}NO/ Pd(111). F = 20 mJ cm^{-2}, T = 340 K.

Table 5.9 First shot yields for mass 44 (CO_2), mass 46 (N_2O) and mass 30 ($^{15}N_2$) for 2 L ^{15}NO/ 2 L CO, 4 L ^{15}NO/2 L CO, 2 L CO /2 L ^{15}NO and 4 L CO/2 L ^{15}NO.

	Y_{FS}/ counts s^{-1}			
	2 L ^{15}NO/2 L CO	4 L ^{15}NO/2 L CO	2 L CO /2 L ^{15}NO	4 L CO/2 L ^{15}NO
CO_2	0	8000	2900	12000
N_2O	0	300	0	0
N_2	5800	4600	3100	2300

From Figure 5.14 and Table 5.9 it can be observed that for 2 L ^{15}NO/2 L CO there is a higher amount of N_2 formation than for 4 L ^{15}NO/2 L CO. This follows the observed trend in TPD experiments, which was explained by a higher fraction of dissociation at a lower NO exposure. N_2O formation was only observed for the 4 L ^{15}NO/2 L CO system in very small amounts and for all the other co-adsorbed systems N_2O was not observed. This result is again consistent with TPD experiments, where the highest amount of desorbed N_2O was observed for the 4 L ^{15}NO/2 L CO system. CO_2 formation shows

interesting trends, opposite from the trend expected on the basis of TPD spectra. Hence, for 4 L ^{15}NO/2 L CO mass 44 (CO_2) formation is higher than for 2 L ^{15}NO/2 L CO where CO_2 formation was not detected. In the TPD experiments, CO_2 formation was higher for the system with a lower NO coverage, simply because there is more CO on the surface that can react with O from NO dissociation to form CO_2. For systems with pre-dosed NO, the CO_2 photodesorption yield was about 4 times higher for 4 L CO/2 L ^{15}NO than for 2 L CO/2 L ^{15}NO. This result again contrasts the TPD results, where formation of CO_2 was higher for the 2 L CO/2 L ^{15}NO system simply because there was slightly more CO on Pd(111) surface.

First shot yields of the reaction products are considerably lower than the first shot yields of the reactants, therefore in order to quantitatively discuss the yields, more experiments will need to be performed. At this point it is difficult to say whether there is any effect of the femtosecond laser on the formation of reaction products different to the one observed in TPD.

5.4 Summary

The main focus of this chapter was on the femtosecond laser-induced desorption and reaction of CO and NO sequentially dosed on the Pd(111) surface for four different systems: 2 L NO/ 2 L CO/ Pd(111), 4 L NO/ 2 L CO/ Pd(111), 2 L CO/ 2 L NO/Pd(111) and 4 L CO/ 2 L NO/ Pd(111). Femtosecond laser studies are accompanied by the results of RAIRS and TPD experiments. RAIRS and TPD experiments show that CO is displaced by NO, and that CO does not cause significant desorption of pre-dosed NO. Changes in the desorption maximum and shape of the desorption curves for CO and NO in co-adsorbed systems are compared with the pure CO(NO) systems of appropriate coverage. The desorption maximum for CO in the CO/NO and NO/CO systems shifts down in temperature with respect to the pure systems, but the shapes of the curves and number of desorption peaks is different depending on the dosing order. The desorption maximum for NO in NO/CO and CO/NO shifts up in temperature, and the shape of the NO TPD peaks in the co-adsorbed systems are similar to the TPD shapes of pure NO. The activation energy for desorption is calculated for CO and NO in all the systems studied, assuming first order desorption and the Redhead analysis.

TPD spectra for the reaction products, N_2, N_2O and CO_2, also depend on the dosing order. The relative ratio of mass 44 to mass 28 is the highest for 4 L NO/2 L CO, which is the system with the highest amount of adsorbed NO. This experimental finding agrees with the literature [36].

Results from the fs-LID of CO and NO are interpreted qualitatively using equation that links the desorption activation energy obtained from TPD spectra with the first shot yield. For the systems where CO is dosed onto Pd(111) first, the ratio of the calculated photodesorption yield of pure NO, and NO in the co-adsorbed systems, agrees well with the ratio obtained experimentally; hence, the model that links the change in the desorption activation energy with the change in photodesorption yield works well. Unfortunately, for the systems where the sequence of the dosing is opposite, ((2, 4 L) ^{13}CO/2 L NO) the model does not work so well. The model predicts that the photodesorption yields for co-adsorbed systems should be approximately the same as the photodesorption yield of pure NO on Pd(111). The experimentally obtained mass 30 photodesorption yield is higher for the co-adsorbed systems than for the pure 2 L NO system. Therefore, probably the Redhead approximation for calculation of the activation desorption energy is not valid for these two systems, since either the pre-exponential factor changes or the order of the desorption changes.

Interpretation of the photodesorption of CO is more complex. The only system for which the model works well is mass 29 photodesorption in 2 L NO/2 L ^{13}CO/ Pd(111). For all other systems, the ratio of the photodesorption yield for pure CO and CO in co-adsorbed systems is twice the experimentally obtained ratio. The discrepancy between the calculated and experimental photodesorption yield might be explained by the change in the pre-expontial factor. The pre-exponential factor is linked with the entropy changes, and one of the contributions to the entropy change is the configurational entropy connected with the availability of sites on the surface. All sites on Pd(111) for the CO molecule are available only for 2 L NO/2 L ^{13}CO/Pd(111). Due to the influence of NO, CO adsorption in all other systems is limited to a smaller number of sites, thus the contribution to the entropy change upon desorption is higher. Therefore, the model would work, if a higher value of the pre-exponential factor is used.

The reaction products for the co-adsorbed systems were recorded for just one fluence, F = 24 mJ cm^{-2}. The isotopes used were CO and ^{15}NO in order to distinguish between residual CO_2 and N_2O. The trends in photodesorption yield were compared with the trends in TPD experiments. For the formation of N_2 and N_2O, the trends are

similar, but regarding the formation of CO_2 there is a possibility for a different branching ratio (desorption/reaction) for femtosecond laser-induced process than in the thermally induced process.

5.5 References

1. J. D. Butler and D. R. Davis, *Journal of the Chemical Society-Dalton Transactions*, (21), 2249 (1976).
2. B. K. Cho, *Journal of Catalysis*, **148** (2), 697 (1994).
3. L. M. Carballo, T. Hahn and H. G. Lintz, *Applied Surface Science*, **40** (1-2), 53 (1989).
4. F. Gao Y. L. Wang and D. W. Goodman, *Journal of Catalysis*, **268** (1), 115 (2009).
5. T. Hahn and H. G. Lintz, *Applied Surface Science*, **40** (1-2), 59 (1989).
6. C. Howitt, V. Pitchon and G. Maire, *Journal of Catalysis*, **154** (1), 47 (1995).
7. K. Y. S. Ng, D. N. Belton, S. J. Schmieg and G. B. Fisher, *Journal of Catalysis*, **146** (2), 394 (1994).
8. S. H. Oh and C. C. Eickel, *Journal of Catalysis*, **128** (2), 526 (1991).
9. S. H. Oh, G. B. Fisher, J. E. Carpenter and D. W. Goodman, *Journal of Catalysis*, **100** (2), 360 (1986).
10. M. Valden, J. Aaltonen, E. Kuusisto, M. Pessa and C. J. Barnes, *Surface Science*, **307**, 193 (1994).
11. A. M. Bradshaw and F. M. Howmann, *Surface Science*, **72** (3), 513 (1978).
12. S. G. Sugai, H. Watanabe,T. Kioka and H. Miki, *Surface Science*, **259** (1-2), 109 (1991).
13. I. Stara and V. Matolin, *Surface Science*, **313** (1-2), 99 (1994).
14. W. A. Brown and D. A. King, *Journal of Physical Chemistry B*, **104** (47), 11440 (2000).
15. K. Honkala, P. Pirila and K. Laasonen, *Surface Science*, **489** (1-3), 72 (2001).
16. D. Loffreda, D. Simon and P. Sautet, J*ournal of Catalysis*, **213** (2), 211 (2003).
17. E. Ozensoy, C. Hess and D. W. Goodman, *Topics In Catalysis*, **28** (1-4), 13 (2004).
18. J. Cortés and E. Valencia, *Chemical Physics Letters*, **463** (1-3), 251 (2008).
19. X. P. Xu, P. J. Chen and D. W. Goodman, *Journal of Physical Chemistry*, **98** (37), 9242 (1994).

20. E. Ozensoy, C. Hess and D. W. Goodman, *Journal of the American Chemical Society*, **124** (29), 8524 (2002).
21. C. Hess, E. Ozensoy and D. W. Goodman, *Journal of Physical Chemistry B*, **107** (12), 2759 (2003).
22. P. J. Chen, and D. W. Goodman, *Surface Science*, **297** (3), L93 (1993).
23. W. K. Kuhn, J. Szanyi and D. W. Goodman, *Surface Science*, **274** (3), L611 (1992).
24. D. R. Rainer, S. M. Vesecky, M. Koranne, W. S. Oh and D. W. Goodman, *Journal of Catalysis*, **167** (1), 234 (1997).
25. H. Arnolds, D. A. King and I. M. Lane, *Chemical Physics*, **350** (1-3), 94 (2008).
26. K. Honkala, P. Pirila and K. Laasonen, *Physical Review Letters*, **86** (26), 5942 (2001).
27. I. Nakamura, T. Fujitani and H. Hamada, *Surface Science*, **514** (1-3), 409 (2002).
28. D. Loffreda, D. Simon and P. Sautet, *Chemical Physics Letters*, **108** (15), 6447 (1998).
29. P. A. Redhead, **12**, *Vacuum*, 203 (1962).
30. *Handbook of Chemistry and Physics*. (CRC Press, 1973).
31. G. Prévot, and C. R. Henry, *Journal of Physical Chemistry B*, **106** (47), 12191 (2002).
32. K. Nakao, S. Ito, K. Tomishige and K. Kunimori, *Journal of Physical Chemistry B*, **109** (37), 17579 (2005).
33. K. Thirunavukkarasu, *K.* Thirumoorthy, J. Libuda and C. S. Gopinath, *Catalysis Letters*, **109** (27), 13272 (2005).
34. C. H. F. Peden, D. N. Belton and S. J. Schmieg, *Journal of Catalysis*, **155** (2), 204 (1995).
35. H. Permana, K. J. Simon Ng, C. H. F. Peden, S. J. Scmieg, D. K. Lambert and D. N. Belton, *Journal of Catalysis*, **164** (1), 194 (1996).
36. S. M. Vesecky, P. J. Chen, X. P. Xu and D. W. Goodman, *Journal of Vacuum Science and Technology A*, **13** (3), 1539 (1995).
37. R. D. Ramsier, Q. Gao, H. N. Waltenburg and J. T. Yates, *Journal of Chemical Physics*, **100** (9), 6837 (1994).
38. E. M. McCash, *Surface Chemistry*. (Oxford University Press, 2001)
39. M. Brandbyge, P. Hedegard, T. F. Heinz, J. A. Misewich and D. M. Newns, *Physical Review B*, **52** (8), 6042 (1995).

40. P. Saalfrank, *Chemical Reviews*, **106**, 4116 (2006)
41. F. Budde, T. F. Heinz, A. Kalamarides, M. M. T. Loy and J. A. Misewich, *Surface Science*, **283** (1-3), 143 (1993).
42. S. Funk, M. Bonn, D. N. Denzler, C. Hess, M. Wolf and G. Ertl, *Journal of Chemical Physics*, **112** (22), 9888 (2000).
43. J. A. Misewich, A. Kalamarides, T. F. Heinz, U. Hofer and M. M. T. Loy, *Journal of Chemical Physics*, **100** (1), 736 (1994)
44. L. M. Struck, L. J. Richter, S. A. Buntin, R. R. Cavanagh and J. C. Stephenson, *Physical Review Letters*, **77** (22), 4576 (1996).
45. P. Szymanski, A. L. Harris and N. Camillone, *Journal of Physical Chemistry A*, **111** (49), 12524 (2007).
46. K. Honkala, P. Pirila and K. Laasonen, *Surface Science*, **489** (1-3), 72 (2001).
47. J. A. Prybyla, T. F. Heinz, J. A. Misewich, M. M. T. Loy and J. H. Glownia, *Physical Review Letters*, **64** (13), 1537 (1990).

CHAPTER 6

SUMMARY AND OUTLOOK

This thesis has described the commissioning of a new ultra high vacuum (UHV) apparatus for femtosecond surface science experiments and its application to femtosecond laser-induced desorption (fs-LID) studies of pure NO and CO on Pd(111) and fs-LID and femtosecond laser-induced reaction (fs-LIR) studies of co-adsorbed NO and CO on Pd(111). It has also described the design and operation of a new femtosecond extreme ultraviolet (XUV) source.

The main purpose of the work described in this thesis is the fs-LID study of the CO + NO on Pd(111). Before investigating this two component system, fs-LID of pure CO and pure NO on Pd(111) were investigated. This served not only as a test of the new apparatus through comparison with previous investigations [1,2], but because our fs-LID studies covered a broader range of fluences than the earlier studies, new information was also obtained. From yield-*vs*-fluence dependence investigations, the existence of fluence thresholds was discovered for both CO/Pd(111) and NO/Pd(111). The fluence threshold for NO was 9 mJ cm^{-2}, and for CO/Pd(111) it was 15 mJ cm^{-2}. Yield-*vs*-fluence dependence curves for NO showed a sigmoidal shape, indicating saturation of desorption, whilst for CO the power law seems to be valid across the whole fluence range studied. The different photoreactivity of NO compared to CO was explained using both the electronic friction model and the desorption induced by multiple electronic transitions (DIMET) model, based on a shorter vibrational and electronic lifetime and a smaller energy difference between the ground and excited potential energy surface for NO on Pd(111).

Temperature programmed desorption (TPD) spectra for NO/Pd(111) and fs-LID experiments showed a small amount of NO dissociation, and this has been associated with the presence of defects, probably (100) steps, on the surface. It would be interesting to know the exact concentration of the defect sites, and this information could be obtained using scanning tunnelling microscopy (STM).

Fs-LID experiments were performed for three different exposures/coverages. The relative coverage calibration was obtained from TPD experiments, assuming that the saturation coverage for NO/Pd(111) is 0.5 ML [3] and for CO/Pd(111) that it is ~0.6 ML [4]. The interpretation of the fs-LID experiments is based on different overlayer structures (occupation of different types of sites) for these exposures. A proper coverage calibration, based on a combination of TPD and LEED or on the use of a quartz crystal microbalance, would support our interpretation of the fs-LID data.

In almost all TPD and fs-LID experiments for pure CO systems, the ^{13}CO isotope was used. TPD spectra of ^{13}CO/Pd(111) have the same shape and T_{max} as TPD spectra of CO, only the area under TPD curve is different, due to the quadrupole mass spectrometer (QMS) having different sensitivity to the two isotopes. However, TPD curves for CO and ^{13}CO can be compared quantitatively if they are multiplied by the appropriate factor obtained from comparison of integrated areas under TPD peaks. In a small number of TPD experiments of the co-adsorbed systems performed for this thesis, ^{15}NO was used instead of NO. The TPD spectra of NO in NO/^{13}CO co-adsorbed systems were compared with ^{15}NO spectra in corresponding ^{15}NO/CO co-adsorbed systems, and in this way ^{15}NO and NO TPD spectra could also be compared quantitatively. Future work could focus on investigating the TPD spectra of pure ^{15}NO on Pd(111). These TPD spectra could then be compared with the TPD spectra of pure NO/Pd(111) in order to obtain a more accurate factor for the quantitative comparison of TPD spectra of NO and ^{15}NO in co-adsorbed systems.

It is hoped that the results of our experiments will be useful as benchmark data for the development of new theoretical models, based on either the the DIMET or friction models, to improve our understanding of the different photoreactivity of NO compared to CO on Pd(111).

As already stated, the primary motivation for the work described in this thesis was the fs-LID of CO + NO on Pd(111). This thesis has described the first investigations of the fs-LID of CO+NO/Pd(111) for four different co-adsorbed systems. The co-adsorbed systems studied are: 2 L NO/2 L CO, 4 L NO/2 L CO, 2 L CO/2 L NO and 4 L CO/2 L NO on Pd(111). Femtosecond laser studies are accompanied by reflection absorption infrared spectroscopy (RAIRS) and TPD experiments. They show that CO is displaced by NO. The shapes and positions of the desorption maxima in the TPD spectra of CO in the co-adsorbed systems depend strongly on the order of dosing. The TPD spectra of NO in the co-adsorbed systems do not differ significantly from the TPD spectrum of

pure NO. The TPD spectra of the reaction products (N_2, N_2O and CO_2) also depend on the dosing order. Results from the fs-LID of CO+NO are interpreted qualitatively based on an equation that links the desorption activation energy obtained from TPD spectra with the first shot photodesorption yield. The model works well only for NO in the co-adsorbed systems where CO is dosed first. For the other systems, agreement between the theoretically predicted and experimental yields is obtained only if a change in the entropy factors or a change in the reaction order is assumed. The trend in the photodesorption yield for the reaction products at one laser fluence was compared with the trend in the TPD experiments. There is a possibility for a different branching ratio between CO desorption and CO_2 formation in the femtosecond laser-induced reaction compared to the TPD experiments.

The experiments performed with CO and ^{15}NO helped to distinguish the reaction product N_2 from CO TPD peaks. More experiments using isotopes would make it possible to obtain quantitative agreement between the experiments performed with ^{13}CO and NO and with CO and ^{15}NO.

The activation energy for desorption was calculated from the Redhead equation[5] for all adsorbate systems. This is the simplest approximation for extracting the desorption energy from a TPD spectrum, when the absolute coverage is not known. A proper coverage calibration, as already mentioned for experiments with pure CO or NO on Pd(111), would enable the use of some other methods based on TPD (for example leading edge analysis) to obtain more accurate values of the activation energy, E_a or pre-exponential factor, ν.

In order to test the model that compares photodesorption yields of CO or NO in pure and co-adsorbed systems, it would be useful to calculate the desorption yields for each of the laser fluences studied in our experiments using a two temperature model in combination with an empirical friction model.

The formation of reaction products is particularly interesting since the CO and NO reaction is one of the reactions in the car exhaust system, and there is still much to learn about the mechanism.

Finally, it is not clear whether femtosecond laser irradiation causes any difference in the amount of reaction products compared to the thermal reaction observed by TPD. The phonon or electron mediated formation of the reaction products could be distinguished using the two-pulse correlation technique (2 PC). In this technique, the

reaction yield is plotted as a function of temporal separation between two equal intensity pulses. The full-width at half-maximum (FWHM) of this correlation function for an electron driven reaction is several picoseconds, while for a phonon driven reaction it is tens of picoseconds.

In order to see the influence of the surface morphology on the CO and NO reaction, femtosecond studies could also be performed for other Pd surfaces, for example Pd(100).

From a technical point of view, the work described in this thesis required the coupling of the femtosecond laser system to a new UHV apparatus. Femtosecond laser light was successfully aligned onto the Pd(111) sample, and the femtosecond laser pulses were characterized spatially and temporally, as described in detail in Chapter 2. In addition, a setup for synchronization of the laser pulses with the QMS was developed. The new experimental set-up works well; however, there are a number of modifications that could be made to make the performance of the experiments easier.

With the current set-up, the absorbed laser fluence cannot be measured, since the reflected laser light does not exit through the UHV chamber. Placing the QMS on another port would require rotating the whole UHV chamber (Figure 2.2, Chapter 2), but it would enable the direct measurement of the absorbed laser light.

Another useful modification is one related to the sample heating design. It was emphasized that the tantalum foil that was spot welded onto the sample and the heating wires did not last for more than a couple of months. This is because resistive heating was used, not only for TPD experiments, but also for the cleaning procedure. The sample cleaning procedure for Pd requires heating to very high temperatures of around 1200 ˚C, therefore it is not surprising that the heating wires or spot welded tantalum foil detach after repetitive cycles of heating and cooling. Electron beam heating is a technique often used in surface science to reach high temperatures during sample cleaning. This technique would enable the use of resistive heating for only the TPD experiments. Hence, for future experiments it would be desirable to implement electron beam heating.

Making the sample mount more rigid would also enable an easier alignment procedure. At the moment, the sample is mounted on the heating wires (Figure 2.4, Chapter 2), and the mount would be more robust if the sample could be placed between solid tantalum rods together with the heating wires.

In addition to setting up the femtosecond surface science experiments, another technical achievement has been the design and testing of a femtosecond extreme ultraviolet (XUV) source. The main result is observation of the 11th harmonic of 800 nm radiation. The 11th harmonic was recorded for three Xe pressures. However, a more detailed investigation of the influence of the gas pressure on the harmonic intensity is necessary in order to compare theoretical simulations with the experimental results. The 11th harmonic has energy 17 eV, which is perfect for gas-phase photoionisation, but a significant challenge for the future will be to generate harmonics around 30 nm for ionising valence electrons, and some core electrons, of the metal-adsorbate system to achieve real time-resolved surface photochemistry.

References

1. P. Szymanski, A. L. Harris. N. Camillone III, *Journal of Physical Chemistry A*, **111** (49), 12524 (2007).
2. J. A. Prybyla, T. F. Heinz and J. A. Misewich, *Physical Review Letters*, **64** (13), 1537 (1990).
3. K. H. Hansen, Z. Sljivancanin and B. Hammer, *Surface Science*, **496** (1-2), 1 (2002).
4. A. M. Bradshaw and H. M. Hoffman, *Surface Science*, **72** (3), 513 (1978).
5. P. A. Redhead, *Vacuum*, **12**, 203 (1962).

APPENDIX A

Theory of generation of femtosecond laser pulses

Femtosecond laser technology is a research field in itself and there are many excellent reviews available, see for example [1]. First, the basic principles of laser action will be explained. Laser is an acronym for 'Light Amplification by Stimulated Emission of Radiation'. This means that photons emitted by spontaneous emission stimulate the emission of further photons, leading to feedback and amplification. The laser light is generated in such a way that first an inversion of the population needs to be achieved. Figure 1 shows a schematic energy level diagram of two-, three- and four-level laser systems. In a two-level system, an equalisation of the populations can be achieved, but never an inversion, and it is not an efficient method for designing a laser. A three-level system is the minimum requirement for lasing to occur. More than half of the population needs to be transferred from the ground state into the upper lasing level, which is very hard to fulfil. A more effective implementation of a laser is based on a four-level system.

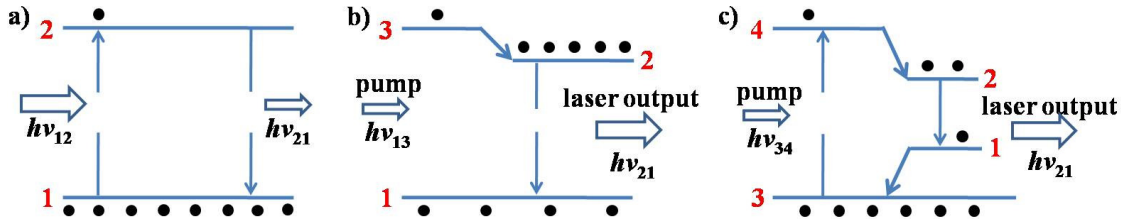

Figure 1 Schematic representation of energy levels for systems used to achieve a population inversion necessary for lasing action: a) a two-level system (excimer laser), b) a three-level system, c) a four-level system.

The simplest layout of a laser cavity consists of a gain medium, and one mirror at each end of the cavity. The medium needs to be pumped in order to achieve a population

inversion, and the cavity then provides a feedback. The cavity supports light frequencies, v, for which the length of the cavity is an integer number of half-wavelengths; these frequencies span the cavity length by starting and ending with a node. These are called the longitudinal modes of the cavity, $v = nc/2L$, where L is the cavity length, c is the speed of light, and n is an integer. The number of longitudinal modes that are amplified in the laser cavity is determined by the spectral bandwidth of the laser transition. For generation of femtosecond pulses, a large number of longitudinal cavity modes must be locked in phase (modelocking). According to the energy-time uncertainty principle, the larger the bandwidth (larger number of modes locked in phase) the shorter the pulse. In most cases, the pulse has a Gaussian distribution of modes and a Gaussian temporal intensity distribution, so that $\Delta\nu\Delta t \geq 0.44$ (Δt is the duration of the pulse, and $\Delta\nu$ is the range of optical frequencies within a pulse, bandwidth). When the value of 0.44 is reached the pulse is said to be Fourier-transform limited.

There are two different types of modelocking: active modelocking and passive modelocking. In most cases, active modelocking relies on inserting into the laser cavity an externally driven acousto-optic modulator. If the frequency of the acousto-optic modulator is equal to the frequency separation between the modes, cavity modes will be locked in phase. For passive modelocking, an intracavity element such as a saturable absorber leads to the modelocking. Ti:sapphire lasers use Kerr lens modelocking. Kerr lens modelocking is a special case of passive modelocking that exploits the optical Kerr effect within the gain medium. The optical Kerr effect is a third-order nonlinear optical effect that causes a change in the refractive index of the medium when an intense electric field is applied. The refractive index, n corresponds to the ratio of the speed of light in a vacuum to the speed of light in a medium under consideration. In the case of an intense electric field, for example from an ultrashort laser, the expression for the refractive index becomes

$$n = n_0 + n_2 I, \tag{1}$$

where n_0 is the linear refractive index, n_2 is the nonlinear refractive index and I is the laser intensity. There are two effects associated with the nonlinear refractive index, one in time domain and the other in the frequency domain. The time-dependence of the

intensity ($I(t)$) induces a time-dependence of the refractive index, $n = n_0 + n_2 I(t)$, which causes a time- dependent phase delay (Equation 2):

$$\Delta\Phi(t) = \frac{n_2 I(t)\,\omega L}{c}, \tag{2}$$

where ω is the angular frequency and L is the length of the medium. The time-dependent phase- delay causes an instantaneous frequency shift, $\Delta\omega$:

$$\Delta\omega = -n_2 \frac{dI(t)}{dt}\omega L / c, \tag{3}$$

that gives rise to new frequency components in the spectrum, broadening the spectrum and shortening the duration of the pulse. This effect is called self-phase modulation. The Kerr effect also causes a positive lens effect because of the spatial intensity profile, as is shown in Figure 2.

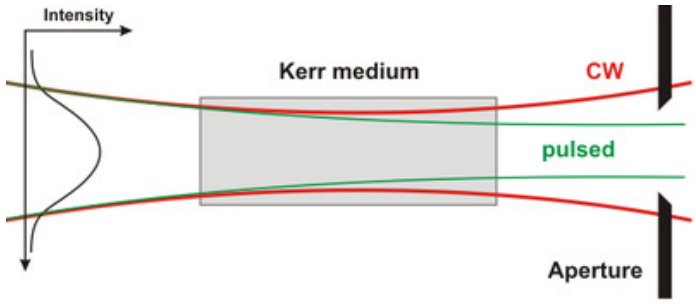

Figure 2 Schematic diagram showing Kerr lens modelocking [2].

Putting a slit in the cavity helps to remove the continuous wave (CW) component and to extract just the middle, modelocked, part of the Gaussian intensity profile.

References

1. P. M. W. French, *Reports on Progress in Physics*, **58** (2), 169 (1995).
2. Wikipedia. April 2005. Kerr lens modelocking. [online]. Available from: http://en.wikipedia.org/wiki/File:Kerr-lens_Modelocking.png.

APPENDIX B

Calculation of the kinetic energy of the recombining electron in the semi-classical model of high harmonic generation

The first step involves finding the solution of the second order differential equation for motion of the electron in the laser field:

$$\frac{\mathrm{d}^2 x}{\mathrm{d}t^2} = -\frac{\mathrm{e}}{m_\mathrm{e}} E_0 \cos \omega t \,, \tag{1}$$

where x denotes the displacement of the electron in a particular time interval, t, e is the charge of the electron, E_0 is the electric field amplitude, m_e is the mass of the electron, and ω is the laser frequency.

The velocity of the electron is defined as $v = \frac{\mathrm{d}x}{\mathrm{d}t}$, so the left side of Equation 1 can be expressed as a first derivative of v with respect to t,

$$\frac{\mathrm{d}v}{\mathrm{d}t} = -\frac{\mathrm{e}}{m_\mathrm{e}} E_0 \cos \omega t \,. \tag{2}$$

Performing the integration of Equation 2 leads to the following relation for the velocity of the electron:

$$v = -\frac{\mathrm{e}E_0}{m\omega} \sin \omega t + v_0 \,. \tag{3}$$

In this model it is assumed that the velocity of the electron just after the ionization (when $t = t_\mathrm{i}$) is zero, therefore v_0 is defined as:

$$v_0 = \frac{\mathrm{e}E_0}{m\omega} \sin \omega t_\mathrm{i} \,, \tag{4}$$

and finally v is,

$$v = -\frac{\mathrm{e}E_0}{m\omega} \sin \omega t + \frac{\mathrm{e}E_0}{m\omega} \sin \omega t_\mathrm{i} \,. \tag{5}$$

After finding the solution for v, the solution for x can be found in the same way, performing the integration under the condition, $t = t_i \leftrightarrow x = 0$,

$$x = \frac{eE_0}{m\omega^2}\cos\omega t + \frac{eE_0 t}{m\omega}\sin\omega t_i - \frac{eE_0}{m\omega^2}\cos\omega t_i - \frac{eE_0 t_i}{m\omega}\sin\omega t_i . \quad (6)$$

From Equation 6 the moment of ionization, t_i can be calculated assuming that $x = 0$ at the moment of recombination, t_r,

$$\cos\omega t_r + \omega t_r \sin\omega t_i - \cos\omega t_i - \omega t_i \sin\omega t_i = 0 . \quad (7)$$

Rearranging Equation 7 using the relation $\tau = t_r - t_i$, and the cosine addition formula, the expression for t_i is:

$$t_i = \frac{1}{\omega}\arctan\frac{\cos\omega\tau - 1}{\sin\omega\tau - \omega\tau} . \quad (8)$$

The next step is to calculate the kinetic energy of the recombining electron,

$$E_k(t_r) = \frac{1}{2}mv^2(t_r) . \quad (9)$$

Using the expression for the ponderomotive potential (Equation 3.5, Chapter 3), the expression relating the intensity of the laser pulse and the electric field amplitude, $I = \frac{E_0^2 \varepsilon_0 c}{2}$, and expression (5) for the velocity of the electron, the kinetic energy of the recombining electron is then equal to:

$$E_k(t_r) = 2U_p(\sin\omega t_i - \sin\omega t_r)^2 . \quad (10)$$

If the above equation is rearranged using the expression $\tau = t_r - t_i$ and the sine addition formula, the following relation is obtained:

$$E_k(t_r) = 2U_p(\sin\omega t_i - \sin\omega t_i\cos\omega\tau - \cos\omega t_i\sin\omega\tau)^2 . \quad (11)$$

Using basic trigonometric relations then lead to Equation 12:

$$E_k(t_r) = 2U_p\cos^2\omega t_i(\tan\omega t_i(1-\cos\omega\tau) - \sin\omega\tau)^2 . \quad (12)$$

In the final expression for the kinetic energy of the recombining electron, the ωt_i term should be replaced with $\omega\tau$. It is then easily seen that one can get rid of $\tan(\omega t_i)$ using Equation 8 to lead to Equation 13:

$$E_{\mathrm{k}}(t_{\mathrm{r}}) = 2U_p \cos^2 \omega t_{\mathrm{i}} \left(\frac{2 - 2\cos\omega\tau - \omega\tau \sin\omega\tau}{\omega\tau - \sin\omega\tau} \right)^2 . \tag{13}$$

The problem of removing the $\cos^2 \omega t_{\mathrm{i}}$ term is overcome by using trigonometric formulas that relate $\tan^2 \omega t_{\mathrm{i}}$ to $\cos^2 \omega t_{\mathrm{i}}$ in the following equations:

$$\cos^2 \omega t_{\mathrm{i}} = \frac{1 + \cos 2\omega t_{\mathrm{i}}}{2}, \tag{14}$$

$$\tan^2 \omega t_{\mathrm{i}} = \frac{1 - \cos 2\omega t_{\mathrm{i}}}{1 + \cos 2\omega t_{\mathrm{i}}} . \tag{15}$$

So, first $\cos 2\omega t_{\mathrm{i}}$ is calculated,

$$\cos 2\omega t_i = \frac{(\sin\omega\tau - \omega\tau)^2 - (\cos\omega\tau - 1)^2}{(\cos\omega\tau - 1)^2 + (\sin\omega\tau - \omega\tau)^2}, \tag{16}$$

and finally $\cos^2 \omega t_{\mathrm{i}}$,

$$\cos^2 \omega t_{\mathrm{i}} = \frac{(\sin\omega\tau - \omega\tau)^2}{(\cos\omega\tau - 1)^2 + (\sin\omega\tau - \omega\tau)^2} . \tag{17}$$

The final expression for the kinetic energy of the recombining electron as a function of $\omega\tau$ is given by the equation:

$$E_{\mathrm{k}}(t_{\mathrm{r}}) = 2U_p \left(\frac{2 - 2\cos\omega\tau - \omega\tau \sin\omega\tau}{1 - \cos\omega\tau - \omega\tau \sin\omega\tau + \frac{1}{2}\omega^2\tau^2} \right)^2 . \tag{18}$$